

Title:

Craspase is a CRISPR RNA-guided, RNA-activated protease

Authors: Chunyi Hu^{1, †}, Sam P. B. van Beljouw^{2,3, †}, Ki Hyun Nam⁴, Gabriel Schuler¹, Fran Ding¹, Yanru Cui¹, Alicia Rodríguez-Molina^{2,3}, Anna C Haagsma^{2,3}, Menno Valk^{2,3}, Martin Pabst⁵, Stan J.J. Brouns^{2,3,*}, Ailong Ke^{1,*}

Affiliations:

¹ Department of Molecular Biology and Genetics, Cornell University, 253 Biotechnology Building, Ithaca, NY 14853, USA.

² Department of Bionanoscience, Delft University of Technology, Van der Maasweg 9, 2629 HZ Delft, Netherlands.

³ Kavli Institute of Nanoscience, Delft, Netherlands.

⁴ Department of Life Science, Pohang University of Science and Technology, Pohang, Gyeongbuk, Republic of Korea

⁵ Department of Environmental Biotechnology, Delft University of Technology, Van der Maasweg 9, 2629 HZ Delft, Netherlands.

† These authors contributed equally.

* Correspondence to ailong.ke@cornell.edu, stanbrouns@gmail.com

Abstract

The Type III-E RNA-targeting effector complex (gRAMP/Cas7-11) is associated with a caspase-like protein (TPR-CHAT/Csx29) to form Craspase (CRISPR-guided caspase). Here we use cryo-electron microscopy snapshots of Craspase to explain its target RNA cleavage and protease activation mechanisms. Target-guide pairing extending into the 5' region of the guide RNA displaces a gating loop in gRAMP, which triggers an extensive conformational relay that allosterically aligns the protease catalytic dyad and opens an amino acid sidechain-binding pocket. We further define Csx30 as the endogenous protein substrate that is site-specifically proteolyzed by RNA-activated Craspase. This protease activity is switched off by target RNA cleavage by gRAMP, and is not activated by RNA targets containing a matching protospacer flanking sequence. We thus conclude that Craspase is a target RNA-activated protease with self-regulatory capacity.

One Sentence Summary:

This work generates the high-resolution mechanisms for RNA-guided RNA and protein cleavage by CRISPR-guided Caspase (Craspase).

Main Text

It has become clear that RNA-guided DNA/RNA degradation is not the sole mechanism for CRISPR-Cas to confer immunity against foreign genetic elements in prokaryotes (1-5). Type III CRISPR-Cas systems in particular present a plethora of alternative mechanisms, including RNA-guided secondary messenger production and signaling (6, 7) to activate a range of immune responses (e.g. collateral RNA damage) (6-8). Type III CRISPR-Cas effectors are typically assembled from multiple protein subunits to enable crRNA binding, target RNA cleavage, DNA cleavage and secondary messenger synthesis (9, 10). Type III-E is a recently identified atypical Type III system: it encodes a large polypeptide (called gRAMP) as a fusion of four Cas7-like domains, one Cas11-like domain, and a big insertion domain (BID) of unfamiliar structural fold, but conspicuously lacks the signatures of a canonical Type III signaling system (e.g. Cas10 and CARF-domain containing proteins) (5). Subsequent studies showed that gRAMP ribonucleoprotein (RNP) complex is capable of RNA-guided RNA cleavage at two specific sites (11, 12), six nucleotides (nts) apart (11). Unlike the Type VI CRISPR-Cas effector Cas13, gRAMP does not cause collateral RNA cleavage, and has no cytotoxicity in eukaryotic cells (12).

In Type III-E loci, gRAMP frequently associates with TPR-CHAT, a caspase-like protein with N-terminal TPR repeats (5). Caspases are a family of cysteine proteases controlling programmed cell death (PCD) pathways in eukaryotes (13). Cleavage of gasdermin by caspases, for example, triggers membrane pore formation to cause cell death (14, 15). An equivalent PCD pathway was recently discovered in prokaryotes, where TPR-CHAT was shown to cleave bacterial gasdermin to induce cellular suicide (2). In Type III-E systems, TPR-CHAT and gRAMP form an effector complex named Craspase, for CRISPR-guided caspase (11). This observation raised the possibility that Craspase functions as a caspase guide by the CRISPR-Cas effector to prevent the spread of phage infection through an RNA-guided suicide mechanism. However, it remains unknown how Craspase is structurally

organized, if TPR-CHAT in Craspase is a protease and whether its activity is RNA-regulated (16, 17).

gRAMP structures in resting, RNA-bound, and post-cleavage states

To gain insights into the RNA-guided target RNA cleavage mechanisms inside gRAMP, we reconstituted *Candidatus "Scalindua brodae"* gRAMP (*Sb*-gRAMP) (11) and determined its cryo-electron microscopy (cryo-EM) structures in different functional states (**Figs. 1A, S1**). Consistent with previous results (11), *Sb*-gRAMP bound to the complementary RNA target with better than 25 nM affinity and cleaved it at two distinct locations, after the 3rd (Site 1) and 9th (Site 2) nucleotides (**Fig. S1A-C**). Single-particle three-dimensional reconstruction produced *Sb*-gRAMP RNP in four different functional states: a 3.81 Å structure of the resting/*apo* state, 3.65 Å structure of the non-matching protospacer flanking sequence (PFS) target bound state, 3.76 Å structure of the matching PFS target bound state, and 3.62 Å structure of the post-cleavage state (**Fig. 1B-E, S2-S4; Table S1**).

The overall architecture of *Sb*-gRAMP is similar to that of *D. ishimotonii* Cas7-11 (*Di*-Cas7-11), recently reported in the target-bound form (18). The two structures in the same functional state superimpose with an r.m.s.d. of 1.1 Å for C α atoms, excluding the BID domain, which is less conserved and poorly resolved in the EM density (**Fig. S5**). *Sb*-gRAMP also shares some degree of similarity with the canonical Type III-A effector Csm (10, 19-21) in overall architecture, guide RNA display, and target RNA binding mode (**Fig. S6**). The *Sb*-gRAMP backbone consists of four non-identical Cas7 domains fused together, instead of three identical Cas7 subunits in Csm (**Figs. S6**). A Zn-knuckle is present in each of the four Cas7s, which appears to be a shared hallmark among Type III effectors (**Fig. S7A**). Csm further contains one copy of Csm4 for 5'-handle recognition, two copies of Csm2 as part of the backbone, and one copy of Csm5 for continued guide-target pairing. In contrast, *Sb*-gRAMP is streamlined: its Cas7.1 has been repurposed for 5'-handle recognition, the single-copy Cas11 domain has been repurposed for target cleavage, and a

structurally distinct BID replaces Csm5 (**Fig. S6A-H**). On the guide RNA side, the ordered 18-nt 5'-handle of the CRISPR RNA (crRNA) in *Sb*-gRAMP is twice as long as in other Class I CRISPR-Cas systems (**Fig. 2A-B**). The majority of the handle residues are bound by Cas7.1 and shielded on the top by the linker from Cas11 to Cas7.2 and the Zn-knuckle in Cas7.2 (**Fig. S6, S7B-C**). Mutagenesis of the Zn-knuckle structure or sequence-specific contacts to the 5'-handle abolished the *in vivo* RNA silencing activity of *Sb*-gRAMP, presumably through disruption of RNP assembly (**Fig. S8**). Surprisingly, *Sb*-gRAMP differs from *Di*-Cas7-11 in crRNA biogenesis. An endoribonuclease center is present in Cas7.1 of *Di*-Cas7-11 for crRNA processing (18). The equivalent residues in *Sb*-gRAMP have been mutated to non-catalytic ones (**Fig. 2C-D**) (18), which rationalized the observation that the crRNA 5'-handle in *Sb*-gRAMP is 3-nt longer (11). We speculate that *Sb*-gRAMP may rely on certain host nucleases for crRNA biogenesis.

Notably, the last two handle nucleotides (5'-A₂C-1-3') are base-pairing competent because they are displayed like a guide (**Fig. 2A, S6H-G**). Type I, III, and IV effectors display the crRNA spacer (guide region) in 6-nt segments, with the 6th nucleotide pinned down by the thumb loop of Cas7; the target is hence recognized in 5-nt segments with the 6th nucleotide unspecified. *Sb*-gRAMP contains major exceptions. The first displayed 5-nt segment contains the last two nucleotides of the 5'-handle and the first three nucleotides of the spacer, a scenario only observed in Type III-E (18) (**Fig. 2A, 2E, S6H-G**). The third segment deviates from the normal again, as an unconventional knotted protein loop from Cas7.4 divides the displayed bases to a 3-nt segment and a 6-nt segment. However, base-pairing in the 3rd segment is not interrupted; a local base buckling accommodates the peptide crossover. The following crRNA nucleotides are displayed by the dynamic BID domain (aa 1031-1385) which is only resolved to low-resolution and therefore docked with an AlphaFold predicted model (22) (**Fig. 1B**).

Off-targeting prevention and RNA cleavage mechanisms in *Sb*-gRAMP

By capturing three additional functional states, we have the temporal resolution to interpret the target recognition and cleavage mechanisms by *Sb*-gRAMP. We found that the long linker from Cas11 to Cas7.2 (G375-E412, here named the gating loop) has acquired important functions for RNase regulation (**Fig. 3A-B, S9**). Its N-terminal portion (G375-G397) senses RNA substrate binding and controls RNase activities. In resting state, the gating loop blocks the first segment of the guide RNA and the nearby Site 1 cleavage center. This conformation is incompatible with target-guide pairing at the first segment and the gating loop has to be displaced to enable cleavage at Site 1 (**Fig. 3A**). We therefore envision that the target-guide pairing initiates from the third and second segments and propagates into the first segment (**Fig. S9**), as observed for other Type III systems (23). In follow-up experiments, we found *Sb*-gRAMP's RNase activity was optimal against a target with 18-nt complementarity from the 5'-end of the spacer portion; 12-nt or shorter complementarity abolished cleavage and 24-nt or longer complementarity attenuated cleavage (**Fig. S10**). This suggests that at least some base-pairing along all three segments of the guide RNA, displayed by Cas7.2-Cas7.4, is required for efficient RNA cleavage. In contrast, additional base-pairing with crRNA at the BID is not required or may even be counterproductive (**Fig. S10**). This is consistent with the previous observation that the 3'-end of the crRNA in the endogenous *Sb*-gRAMP is often as short as 20 nt (11), and that the BID is dispensable for Cas7-11 activity in human cells (18).

Sb-gRAMP was further incubated with two kinds of RNA targets whose PFS was either matching (complementary) or non-matching with the 5'-handle in the crRNA, as complementarity in this region may be indicative of a self-target (i.e. anti-sense transcript from the CRISPR locus) and thus perhaps leads to alternative structural configurations in *Sb*-gRAMP. However, our structures reveal that regardless of the PFS status, RNA binding induces the same set of conformational changes in *Sb*-gRAMP. Where the guide nucleotides are pinned down by the Cas7 thumbs, the corresponding target nucleotides (4th and 10th) flip outwards. Rotation of the backbone orients their 2'-OH towards the previous phosphate,

forming the so-called “in-line” conformation, which is necessary for RNA cleavage. For target RNA with a matching PFS, the first segment consists of five base-pairs, starting from the last two nucleotides of the 5'-handle and ending with the 3rd nucleotide in the spacer portion (**Fig. 2E**). The rest of the PFS is not traceable in the EM map. For target RNA with a non-matching PFS, only three base-pairs are found between the target RNA and the spacer portion of the guide. The first two nucleotides of the PFS do not form hydrogen bonds with the two 5'-handle residues on the opposite side, but they remain stacked to complete the first target-guide segment (**Fig. 2E**). In both PFS matched and non-matched conditions, the impinging gating loop in *Sb*-gRAMP is pushed away from the first segment and becomes entirely disordered (**Fig. 3A**). Concurrently, the cleavage center at Site 1 is exposed and further enhanced by a hinge motion in Cas11 (**Fig. 3C, S11A**), which aligns catalytic residues among Cas11 and Cas7.2. It should be noted that stacking from the additional 2-nt PFS is not a prerequisite to activate *Sb*-gRAMP, as RNA substrates lacking nucleotides in the PFS region were found to be cleaved efficiently (11, 18). To validate these structural findings, we replaced the tip of the gating loop with a flexible linker to evaluate its importance in target RNA recognition (**Fig. S9D-E**). Wild-type *Sb*-gRAMP did not bind or cleave RNA that only base-pairs with the first 9-nt of the crRNA guide. In contrast, the gating loop mutant bound this target RNA efficiently to subsequently cleaved it (**Fig. 3D**). These experiments suggest the gating loop is playing a pivotal role in preventing off-targeting. Overall, our RNA-bound *Sb*-gRAMP structures support a mechanistic model in which the resting *Sb*-gRAMP exists in an autoinhibited state to avoid sequence-unspecific RNA binding and cleavage. Target RNA is validated via crRNA-pairing in a directional fashion from the 3' to 5' region of the guide. Upon completion of target binding, movement of the gating loop initiates a chain of allosteric events to switch on the RNase centers in gRAMP (**Fig. 3E; Movie S1**).

We further attempted to interpret the cleavage mechanism by comparing the pre- and post-cleavage states (**Fig. 1, 3F-G**). EM densities suggest the RNA substrate was cleaved after the 3rd and 9th nucleotides (Site 1 and Site 2, respectively) (**Fig. 2E**), which is consistent with

previous reports (11, 18). Since cleavage is metal-dependent, we identified multiple candidate residues around the cleavage sites that may contribute to metal coordination (generally acidic residues), proton shuttling (generally polar residues), and transition state stabilization (generally positively charged residues) (**Fig. 3F-G**). In subsequent mutagenesis testing (**Fig. S11B-D**), RNA cleavage at Site 1 was abolished by alanine substitutions to D547 in Cas7.2 and R294, D298, Y367, and K371 in Cas11 (**Fig. 3H**). Since Site 1 is assembled from residues in both Cas11 and Cas7.2, it may only become active after target binding-induced hinge motion in Cas11. Cleavage at Site 2 was abolished by Cas7.3 mutations D698A (11) and D806A, but not by Cas11 mutations R323A and H328A (**Fig. 3H**). An allosteric effect was noticed: Site 1 disruptive mutations D547A and D298A impaired Site 2 cleavage as well, and Site 2 mutation H328A impaired Site 1 cleavage instead. These mutants appeared to weaken or alter the RNA-binding mode of *Sb*-gRAMP, as revealed by electrophoretic mobility shift assay (EMSA) (**Fig. 3H, S11C**). *Sb*-gRAMP containing the double mutations R294A/D698A or D547/D806A was efficient in RNA binding but completely inactive in RNA cleavage (**Fig. S11C**). Such dead-gRAMP variants could be useful in RNA editing, tagging, or tracing applications.

Craspase architecture and component interfaces

To gain mechanistic insights into how the putative RNA-guided protease system may work, we reconstituted Craspase in its apo (resting) state, the matching PFS-containing RNA target bound state, and the non-matching PFS-containing target bound state and generated their corresponding cryo-EM structures at 3.7 Å, 2.6 Å, and 2.7 Å resolutions, respectively (**Fig. S12-S14**). The TPR-CHAT binding surface is on top of the buried crRNA 5'-handle in *Sb*-gRAMP, architecturally similar to where the cOA synthetase (Csm1/Cas10) binds in canonical Type III-A effector complexes (**Fig. 4A-B, S15A, Movie S2**). TPR-CHAT consists of an N-terminal TPR domain (aa 1-323), a dynamic mid-region (aa 324-399), and a C-terminal cysteine protease from the caspase family (aa 400-717). The domain arrangement of TPR-CHAT resembles that of separase (24, 25), an essential eukaryotic protein that

cleaves the cohesin ring to allow chromosome segregation (**Fig. S15B-D**). Like separate, the CHAT domain contains a N-terminal pseudo-caspase domain, a long dimeric coiled coil mid-insertion, and a C-terminal active-protease domain (24, 25). Although structurally distinct, the two caspase domains pack in a similar fashion as the eukaryotic caspase dimers do (26). In TPR-CHAT, the β -sheet structure in the pseudo-caspase domain interacts with the TPR domain and the mid-region serves as the sole anchoring point of CHAT onto *Sb*-gRAMP. The TPR repeats belong to the so-called solenoid domains, which are assembled from repeating structural units and often mediate protein-protein or protein-ligand interactions (27). The seven TPR repeats in TPR-CHAT pack side-by-side to form a C-shaped architecture, with the 7th TPR repeat packing against the β -sheet of the globular CHAT domain. Together, TPR-CHAT adopts the rough shape of a padlock, with TPR being the shackle and CHAT the body (**Fig. S15B**). In the Craspase structure without target RNA (apo-Craspase), the shackle of the padlock captures a long “switch helix” (aa338-362) in the middle. The switch helix is captured by the molecular contacts from the inward facing loops in the TPR repeats. When wedged in the shackle, the switch helix pins down a loop-helix-loop structure underneath (aa 324-337). Together, they mediate an extensive set of molecular contacts to multiple regions inside the padlock (**Fig. S15B**), including contacts to the tips of two long β -hairpins (sensor hairpins) that further extend all the way to the protease center in CHAT (**Fig. S15E**).

An area of $\sim 75 \times 35 \text{ \AA}^2$ of the Cas7.1 surface in *Sb*-gRAMP is buried by TPR-CHAT (**Fig. 4C-D**). However, the actual physical contacts between TPR-CHAT and *Sb*-gRAMP are limited to two surface patches 50 \AA apart. On the TPR side, a hydrophobic patch in the first and second TPR repeats makes hydrophobic and mainchain hydrogen bond contacts to a portion of the gating loop (F381, I383, and L384), and a nearby Cas7.2 loop (L450, V451) (**Fig. 4C**). A more extensive and mostly hydrophobic interface is found between one of the coiled coil helix in the CHAT domain (aa 434-450) and two regions of *Sb*-gRAMP, namely the C-terminal portion of the gating loop (aa 396-403) and the Zn-knuckle of Cas7.2 (**Fig.**

4D). In particular, Y450 and L499 of CHAT insert into a hydrophobic pocket on the *Sb*-gRAMP surface, promoting shape complementarity at the interface. The interaction between gRAMP and TPR-CHAT was completely disrupted by Y75A and F103A mutations in the TPR interface, and severely impaired by A445R and L449A/Y450A mutations in the CHAT interface (**Fig. 4E**). An important observation is that the gating loop of *Sb*-gRAMP, which plays a pivotal role in regulating the RNase activity of *Sb*-gRAMP through conformational changes, is sandwiched between *Sb*-gRAMP and TPR-CHAT (**Fig. S16A**). Whereas the entire gating loop becomes unstructured in the RNA-bound *Sb*-gRAMP structure, only the tip of it is rearranged in the RNA-bound Craspase (**Fig. 3A, S17**). Given this conformational restriction, we speculated that the energetic barrier for RNase activation may be higher in Craspase compared to *Sb*-gRAMP. Indeed, RNA binding was consistently weaker at different temperatures and the cleavage was slower in Craspase compared to *Sb*-gRAMP (**Fig. 4F, S16B-C**).

RNA-guided protease activation mechanism in Craspase

When Craspase is in the resting state, the catalytic dyad in the TPR-CHAT protease center, Cys627 and His585, are 6.6 Å apart (**Fig. S18**). As this exceeds hydrogen bonding distance by a large margin, C627 could not be deprotonated by H585, hence could not initiate the nucleophilic attack on the peptide substrate. Our structure therefore suggests TPR-CHAT is an inactive protease in the apo Craspase. When Craspase is bound to a target RNA with a matching PFS (**Fig. 5A**), a perfectly base-paired first segment is formed between guide and target. Constrained by the base-pairing from the first two PFS residues to the guide, the remaining PFS nucleotides point towards the bottom of TPR. Although their densities are difficult to model, possible phosphate densities suggest that the PFS travels underneath TPR (**Fig. 5C, Movies S3-S5**). This path may have perturbed the conformation dynamics of the sensing β -hairpin in CHAT, as its tip that may contact PFS becomes disordered. This coincides with a backbone twitch at the protease center, on the opposite end of the sensing hairpin (aa 626-631) (**Fig. 5D**). Notably, C627 and H585 reside on the two strands of the

sensing hairpin. The allosteric change shortens their distance from 6.6 to 5.2 Å (**Fig. S18B**). This distance, however, is still too far to allow H585-mediated C627 deprotonation. Moreover, the nearby sidechain-binding pocket found in the apo structure is closed after the structural rearrangement (**Fig. 5D**). Therefore, the matching PFS RNA bound Craspase is not expected to be proteolytically active, either.

A greater set of conformational changes take place when RNA target containing a non-matching PFS is bound by Craspase (**Fig. 5B**). Lacking sequence complementarity to the first 2-nt of PFS, the base-pairing in the first guide-target segment is incomplete and the gating loop is only partially dislodged (**Fig. S17**). While the first nucleotide of PFS forms a partially frayed A•C pair, the rest of PFS pivots toward the surface of TPR (**Fig. 5C**). The switch helix is dislodged from the shackle of the padlock, possibly due to clashes with the non-matching PFS. This helix and the preceding loop-helix-loop connection rotates 90 degree and packs against CHAT as a coiled coil structure (**Fig. 5D, S19**). The sensor hairpin undergoes a larger set of long-range allosteric alteration. Consequently, C627 and H585 become oriented within hydrogen bonding distance (3.3 Å) (**Fig. 5D**), and a hydrophobic pocket opens nearby (**Fig. S18C**). The entire CHAT domain further undergoes a rigid-body movement. The cleft between *Sb*-gRAMP and TPR-CHAT widens, which may enable the peptide substrate to access binding surfaces (**Fig. 5D**).

Based on the observed structural features in the protease center, we designed candidate peptides to probe for potential RNA-guided peptidase activity in Craspase. We noticed that one designed peptide showed Craspase-dependent cleavage in thin-layer chromatography assays (**Fig. S20A-B, 5E**). Consistent with our mechanistic predictions, the activity was stronger in the presence of a non-matching PFS RNA substrate, but not a matching PFS substrate (**Fig. 5E**). This peptide could also be cleaved by Craspase in the context of an inter-domain protein linker, and the cleavage was stimulated by non-PFS target RNA (**Fig. S20C-F**). Mass spectrometry (MS) revealed that the cleavage took place after a leucine

residue (**Fig. S21**). Judging by the fact that only one of the two leucine residues in the peptide was selectively cleaved (**Fig. 5F**), and that the cleavage activity was low and only partially RNA-dependent, Craspase clearly specifies additional sequences nearby.

The above mechanistic analysis defines how RNA-guided RNA recognition regulates the protease activity of Craspase (**Fig. 5G**). Sequence complementarity in the target RNA is a prerequisite, which is indirectly read out from the gating loop movement. A NOT logic gate is also in place to avoid activation by a self-RNA. Craspase is only activated when both conditions are true. The structural feature performing the logic calculation is the switch helix: its movement triggers a stepwise conformational relay that allosterically unlocks the TPR-CHAT padlock and switches on the protease activity (**Fig. 5H**).

Craspase proteolytically cleaves Csx30 in an RNA-dependent manner

Type III-E *loci* encode three other well-conserved proteins: the putative sigma-factor RpoE and two proteins of unknown function, denoted Csx30 and Csx31 (5, 11, 12). As a protease and its target are often co-localized in the genome (2, 8), we tested Craspase protease activity against these proteins in co-expression experiments (**Fig. 6A**). Full-length Csx30 was strongly reduced in the presence of target bound Craspase, whereas full-length RpoE and Csx31 levels were unaffected (**Fig. 6B**). This effect was alleviated when Craspase carried inactivated cysteine-histidine residues (H585A and C627A) (**Fig. 6B**), suggesting that Craspase possesses proteolytic activity against Csx30. This observation was confirmed *in vitro*, where purified Craspase processes Csx30 in two distinct fragments (**Fig. 6C; Table S2**), demonstrating that Csx30 is a natural protein target of Craspase. Mutational analysis of the amino acids encompassing the cleavage site showed that L407 in Csx30 is important for Craspase activity (**Table S3; Table S4; Fig. S22A-B**). Cleavage by Craspase after a leucine residue is consistent with MS (**Fig. S22A**) and the peptide cleavage experiments (**Fig 5E-F**). Corroborating the structural insights, proteolytic digestion could only be observed in the presence of target RNA with non-matching PFS, whereas no cleavage fragments

accumulated with non-target RNA or target RNA with matching PFS (**Fig. 6C**; **Fig. 6D**). As Craspase cleaves bound RNA only under bivalent cation conditions (11), we reasoned that the peptidase in target bound Craspase would be stay active in the absence of magnesium ions. We indeed observe a marked increase in Csx30 processing under magnesium poor conditions compared to magnesium rich conditions (**Fig. 6E**), suggesting that target RNA cleavage switches off the peptidase. This is further supported by the finding that the peptidase activity of a nuclease-dead variant of Craspase is not impaired in the presence of magnesium ions (**Fig. 6E**), rendering Craspase R294A D698A a 'stay-on' variant. Binding of a complementary ssDNA, which is not cleaved by Craspase (11, 12), does not activate the peptidase (**Fig. 6E**). These findings combined support a model (**Fig. 6F**) in which the peptidase activity of Craspase is switched-on upon target RNA binding to cleave Csx30 after L407, separating a large N-terminal fragment of ~47 kDa from a small C-terminal fragment of ~19 kDa small fragment. Due to the low sequence and structural similarity to known proteins, a prediction of the function of the two protein fragments cannot be made with confidence (**Fig. S22C**). However, based on analogous defense systems, processed Csx30 fragments likely enable an immune response, possibly by eliciting toxicity to the native host cell. Craspase then self-regulates through target RNA cleavage to switch the peptidase off, thereby timing the duration of the immune response and possibly recycling the Craspase complex to bind new target RNAs.

Discussion

A new frontier in CRISPR-Cas biology has emerged, in which the RNA-guided effectors control physiological responses using mechanisms other than nucleic acid degradation. Here we define how the Craspase protease is allosterically activated by target RNA recognition and inactivated by target RNA cleavage to cleave the native substrate Csx30 in a binary fashion. We tuned its dynamic response range using mechanism-inspired mutants, which will pave the way for biotechnological and therapeutic applications.

Our observations point to the possibility that the cleavage sequence in the native protein substrate is read out in the context of the 3D structure, which is also the case for the molecular recognition of gasdermins by eukaryotic caspases (26, 28). We wait for follow-up studies to reveal the missing recognition codes in substrate recognition and cleavage.

Despite the large structural distinctions, our studies revealed that Type III-E share fundamental mechanistic similarities with canonical CRISPR-Cas Type III systems. Analogous to Cas10 activation in other Type III effectors, Craspase only turns on the protease activity in response to non-self RNA targets, whereas it does not differentiate self and non-self RNA targets at the RNA cleavage level. This, combined with the observation that Craspase switches off protease activity upon target RNA cleavage, suggests that the protease activity may only be desired temporarily in the cell, which points to a possible ominous consequence of turning on the Craspase pathway. Does Csx30 proteolysis lead to cell dormancy or possibly programmed cell death? Due to the lack of homology to known proteins, it is difficult to infer the physiological function of Csx30 with confidence. Based on the AlphaFold (22) predicted structure, we speculate that proteolysis may relieve a physical sequestration or trigger a conformational change in Csx30, converting it to the active form (**Fig. S22C-D**). An analogous scenario was described for bacterial gasdermin, which only induced its anti-viral effect after site-specific cleavage by TPR-CHAT (2). Potential involvement of other Craspase-associated proteins, RpoE and Csx31, needs to be assessed in future experiments. However, unraveling the biological details is complicated by the difficulty of working with the native host *Candidatus* "Scalindua brodae" (29). Alternative model organisms may be needed for future functional dissections. On the application side, the fact that the Craspase peptidase is only active in the presence of a specific RNA species renders it useful for both in vivo (e.g. gene expression profiling) and in vitro (e.g. RNA diagnostics) biotechnological applications. This will represent a major expansion of the range of biomolecular engineering possibilities of CRISPR-Cas effectors.

References and Notes

1. S. Doron et al., Systematic discovery of antiphage defense systems in the microbial pangenome. *Science* 359, (2018).
2. A. G. Johnson et al., Bacterial gasdermins reveal an ancient mechanism of cell death. *Science* 375, 221-225 (2022).
3. S. A. Shah et al., Comprehensive search for accessory proteins encoded with archaeal and bacterial type III CRISPR-cas gene cassettes reveals 39 new cas gene families. *RNA Biol* 16, 530-542 (2019).
4. K. S. Makarova et al., Evolutionary and functional classification of the CARF domain superfamily, key sensors in prokaryotic antiviral defense. *Nucleic Acids Res* 48, 8828-8847 (2020).
5. K. S. Makarova et al., Evolutionary classification of CRISPR-Cas systems: a burst of class 2 and derived variants. *Nature reviews. Microbiology* 18, 67-83 (2020).
6. M. Kazlauskienė, G. Kostiuik, C. Venclovas, G. Tamulaitis, V. Siksnys, A cyclic oligonucleotide signaling pathway in type III CRISPR-Cas systems. *Science* 357, 605-609 (2017).
7. O. Niewoehner et al., Type III CRISPR-Cas systems produce cyclic oligoadenylate second messengers. *Nature* 548, 543-548 (2017).
8. C. Rouillon et al., SAVED by a toxin: Structure and function of the CRISPR Lon protease. *bioRxiv*, 2021.2012.2006.471393 (2021).
9. R. Molina, N. Sofos, G. Montoya, Structural basis of CRISPR-Cas Type III prokaryotic defence systems. *Curr Opin Struct Biol* 65, 119-129 (2020).
10. L. You et al., Structure Studies of the CRISPR-Csm Complex Reveal Mechanism of Co-transcriptional Interference. *Cell* 176, 239-253 e216 (2019).
11. S. P. B. van Beljouw et al., The gRAMP CRISPR-Cas effector is an RNA endonuclease complexed with a caspase-like peptidase. *Science* 373, 1349-1353 (2021).

12. A. Ozcan et al., Programmable RNA targeting with the single-protein CRISPR effector Cas7-11. *Nature* 597, 720-725 (2021).
13. Y. Shi, Caspase activation: revisiting the induced proximity model. *Cell* 117, 855-858 (2004).
14. J. Ding et al., Pore-forming activity and structural autoinhibition of the gasdermin family. *Nature* 535, 111-116 (2016).
15. J. Shi et al., Cleavage of GSDMD by inflammatory caspases determines pyroptotic cell death. *Nature* 526, 660-665 (2015).
16. M. L. Hochstrasser, J. K. Nunez, CRISPR meets caspase. *Nat Microbiol* 6, 1481-1482 (2021).
17. R. J. Catchpole, M. P. Terns, New Type III CRISPR variant and programmable RNA targeting tool: Oh, thank heaven for Cas7-11. *Mol Cell* 81, 4354-4356 (2021).
18. K. Kato et al., Structure and engineering of the type III-E CRISPR-Cas7-11 effector complex. *Cell*, (2022).
19. N. Jia et al., Type III-A CRISPR-Cas Csm Complexes: Assembly, Periodic RNA Cleavage, DNase Activity Regulation, and Autoimmunity. *Mol Cell* 73, 264-277 e265 (2019).
20. M. Guo et al., Coupling of ssRNA cleavage with DNase activity in type III-A CRISPR-Csm revealed by cryo-EM and biochemistry. *Cell Res* 29, 305-312 (2019).
21. S. Sridhara et al., Structural and biochemical characterization of in vivo assembled *Lactococcus lactis* CRISPR-Csm complex. *Commun Biol* 5, 279 (2022).
22. J. Jumper et al., Highly accurate protein structure prediction with AlphaFold. *Nature* 596, 583-589 (2021).
23. J. A. Steens et al., SCOPE enables type III CRISPR-Cas diagnostics using flexible targeting and stringent CARF ribonuclease activation. *Nat Commun* 12, 5033 (2021).

24. Z. Lin, X. Luo, H. Yu, Structural basis of cohesin cleavage by separase. *Nature* 532, 131-134 (2016).
25. A. Boland et al., Cryo-EM structure of a metazoan separase-securin complex at near-atomic resolution. *Nat Struct Mol Biol* 24, 414-418 (2017).
26. Z. Liu et al., Caspase-1 Engages Full-Length Gasdermin D through Two Distinct Interfaces That Mediate Caspase Recruitment and Substrate Cleavage. *Immunity* 53, 106-114 e105 (2020).
27. G. L. Blatch, M. Lasse, The tetratricopeptide repeat: a structural motif mediating protein-protein interactions. *Bioessays* 21, 932-939 (1999).
28. K. Wang et al., Structural Mechanism for GSDMD Targeting by Autoprocessed Caspases in Pyroptosis. *Cell* 180, 941-955 e920 (2020).
29. T. Awata et al., Physiological characterization of an anaerobic ammonium-oxidizing bacterium belonging to the "Candidatus scalindua" group. *Appl Environ Microbiol* 79, 4145-4148 (2013).
30. A. Punjani, J. L. Rubinstein, D. J. Fleet, M. A. Brubaker, cryoSPARC: algorithms for rapid unsupervised cryo-EM structure determination. *Nat Methods* 14, 290-296 (2017).
31. S. H. Scheres, RELION: implementation of a Bayesian approach to cryo-EM structure determination. *J Struct Biol* 180, 519-530 (2012).
32. E. F. Pettersen et al., UCSF Chimera--a visualization system for exploratory research and analysis. *J Comput Chem* 25, 1605-1612 (2004).
33. P. Emsley, B. Lohkamp, W. G. Scott, K. Cowtan, Features and development of Coot. *Acta Crystallogr D Biol Crystallogr* 66, 486-501 (2010).
34. D. Liebschner et al., Macromolecular structure determination using X-rays, neutrons and electrons: recent developments in Phenix. *Acta Crystallogr D Struct Biol* 75, 861-877 (2019).

35. C. J. Williams et al., MolProbity: More and better reference data for improved all-atom structure validation. *Protein Sci* 27, 293-315 (2018).
36. S. F. Altschul, W. Gish, W. Miller, E. W. Myers, D. J. Lipman, Basic local alignment search tool. *J Mol Biol* 215, 403-410 (1990).

Acknowledgements

Funding

National Institutes of Health grant GM118174 (AK)

Department of Defense through the National Defense Science & Engineering Graduate Fellowship Program (GS)

NSF MRSEC program grant DMR-1719875 (Cornell Center for Materials Research Shared Facilities)

DOE Office of Biological and Environmental Research grant KP1607011 (Laboratory for BioMolecular Structure (LBMS))

Netherlands Organisation for Scientific Research (NWO VICI; VI.C.182.027 to S.J.J.B.)

European Research Council (ERC) CoG under the European Union's Horizon 2020 research and innovation program (grant agreement no. 101003229 to S.J.J.B.)

Author Contributions

Conceptualization: AK, CH, SB, SvB

Methodology: CH, GS, KHN, FD, YC, AK, SB, SvB, AH, ARM, MP

Investigation: CH, GS, KHN, FD, YC, AK, SB, SvB, AH, ARM, MP, MV

Visualization: CH, AK

Funding acquisition: AK, SB

Project administration: AK, SB

Supervision: AK, SB

Writing – original draft: AK, CH, GS, SB, SvB

Writing – review & editing: AK, CH, GS, SB, SvB

Competing Interests

The authors declare competing financial interests on Craspase-inspired genome editing applications. S.P.B.v.B. and S.J.J.B. are inventors on patent application N2028346 and PCT/NL2022/050296 submitted by Delft University of Technology that covers uses of gRAMP and Craspase. A provisional patent application related to this research has been filed by Cornell University.

Data and materials availability: The resting-gRAMP coordinates and cryo-EM density map have been deposited in the Protein Data Bank (PDB:8D97) and the Electron Microscopy Data Bank (EMD-27257); gRAMP/non matching PFS RNA bound (PDB:8D8N, EMD-27252); gRAMP/matching PFS RNA bound (PDB:8D9E, EMD-27259); gRAMP/non matching PFS RNA post cleavage state (PDB:8D8I, EMD-27263); Craspase complex (PDB:8D8F, EMD-27260); Craspase/matching PFS RNA complex (PDB:8D8H, EMD-27262); Craspase/non-matching PFS RNA complex (PDB:8D8G, EMD-27261) Plasmids used in this study are available upon request.

Supplementary Materials

Materials and Methods

Table S1-S5

Fig S1 – S22

References (30-36)

Movie S1-S7

Figure legends

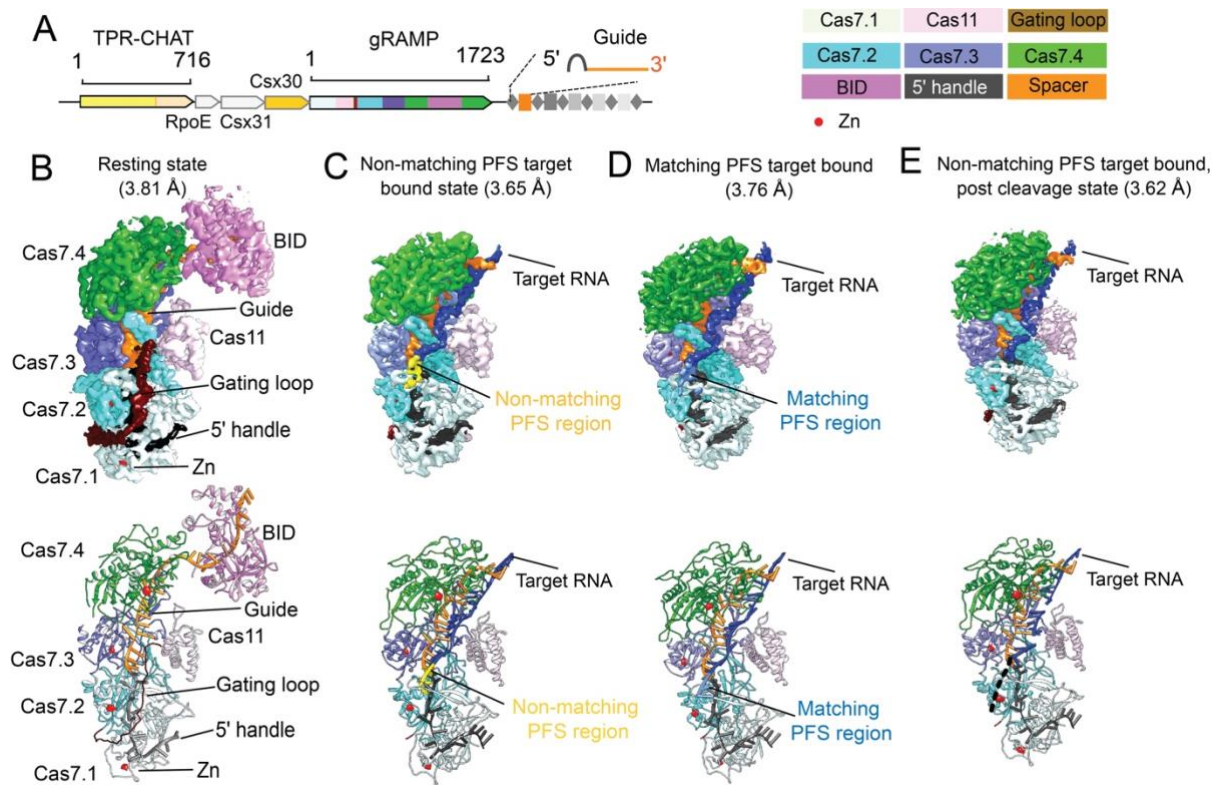


Fig. 1. Structural snapshots of *Sb*-gRAMP RNP in different functional states. (A) Type III-E operon in *Candidatus* 'Scalindua brodae'. Snapshot of **(B)** *Sb*-gRAMP at resting state, **(C)** non-matching PFS RNA bound state, **(D)** matching PFS RNA bound state, and **(E)** non-matching PFS RNA post-cleavage state with MgCl₂. Top images are cryo-EM densities and bottom images are structural models.

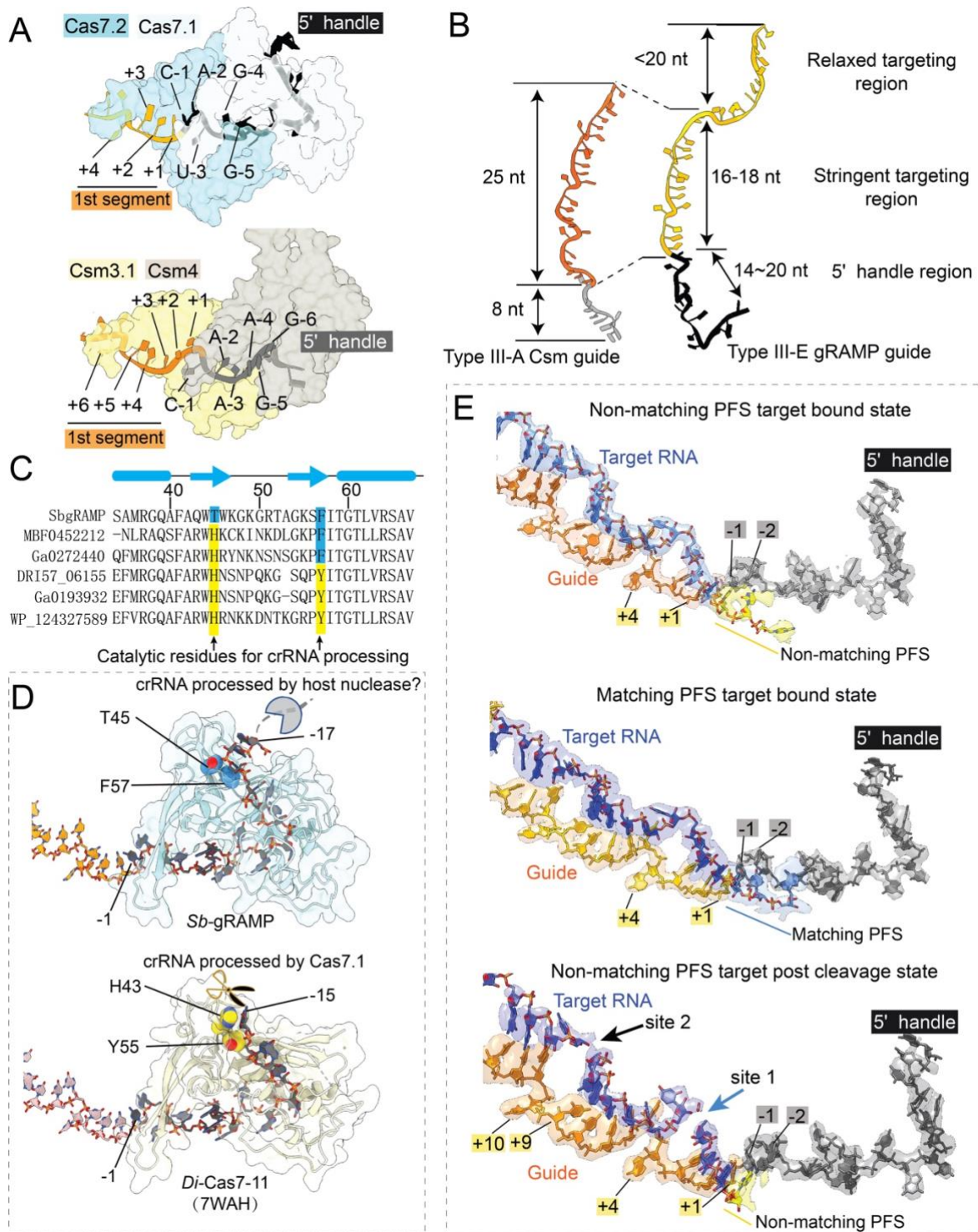


Fig. 2. crRNA accommodation and target RNA recognition mechanisms by *Sb*-gRAMP. (A) Accommodation of crRNA 5'-handle and (B) spacer region in Type III-E *Sb*-gRAMP and Type III-A Csm. (C) Primary sequence and (D) 3D structural alignment at the pre-crRNA cleavage center. Catalytic residues in *Di*-Cas7-11 are colored in yellow; equivalent residues in *Sb*-gRAMP are in blue. (E) Extracted Cryo-EM density from non-matching PFS RNA (left), matching PFS RNA (middle) and non-matching PFS RNA post-cleavage state (right).

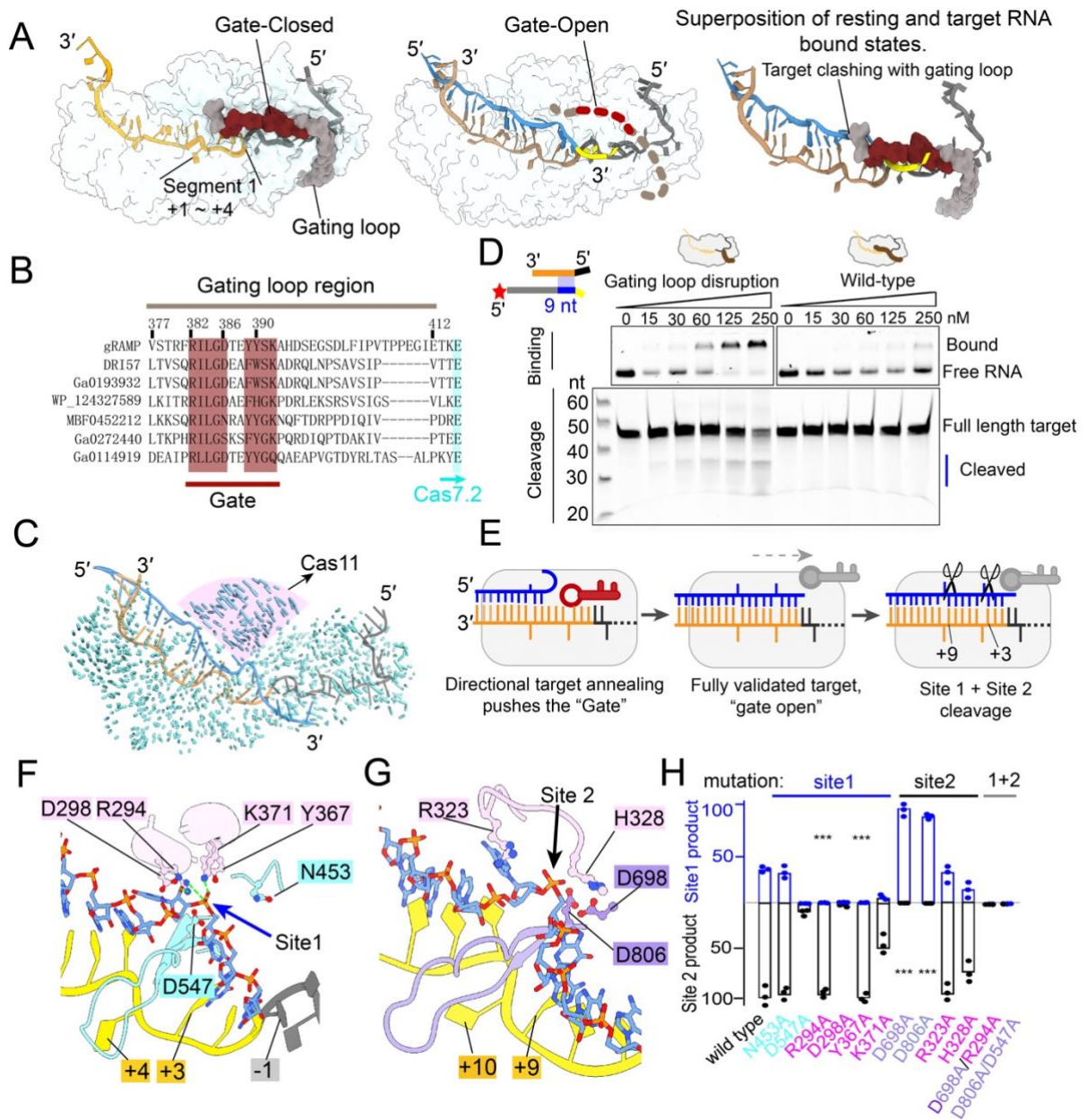


Fig. 3. Target validation and cleavage mechanisms by *Sb*-gRAMP RNP. (A) Models depicting the gate closed structure in resting state (left) and gate open structure in target RNA bound state (middle). Superposition is shown as the right panel. **(B)** Sequence alignment at the gating loop region. Conserved residues are highlighted in burgundy red. **(C)** Structural comparison of the resting and non-matching PFS RNA bound states. Vector length is proportional to residue movement distance. Hinge motion in Cas11 is pronounced. **(D)** EMSA (top) and urea-PAGE (bottom) to evaluate the impact of gating loop disruption on the binding and cleavage of partially matching RNA targets. **(E)** Mechanistic model depicting the essential role of the gating loop in target validation. **(F)** Structural basis for Site 1 cleavage. **(G)** Structural basis for Site 2 cleavage. **(H)** Impact of Site 1 (in blue) and Site 2 (in black) mutations on target RNA cleavage efficiency.

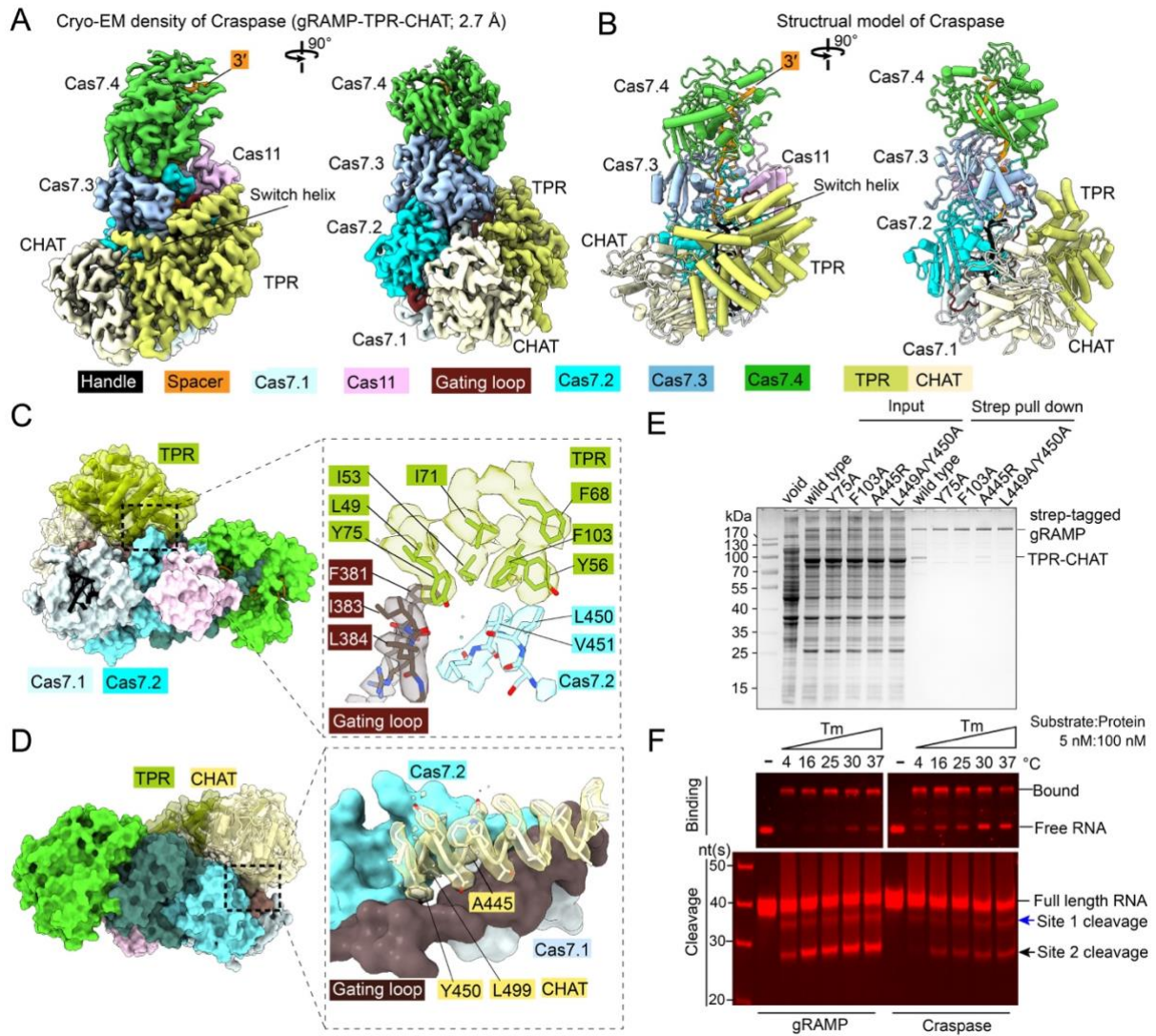


Fig. 4. Structural basis for Craspase assembly. (A) 2.7 Å cryo-EM density and **(B)** structural model of Craspase (gRAMP-TPR-CHAT). **(C)** Location and zoom-in view of the molecular contacts between gRAMP and TPR. Interface residues and corresponding cryo-EM densities are shown. **(D)** Location and zoom-in view of the molecular contacts between gRAMP and CHAT. **(E)** Strep-tag affinity purifications quantifying the impact of interface mutations on Craspase complex formation. **(F)** EMSA (top) and urea-PAGE (bottom) to quantify activity differences in RNA binding and cleavage by gRAMP and Craspase.

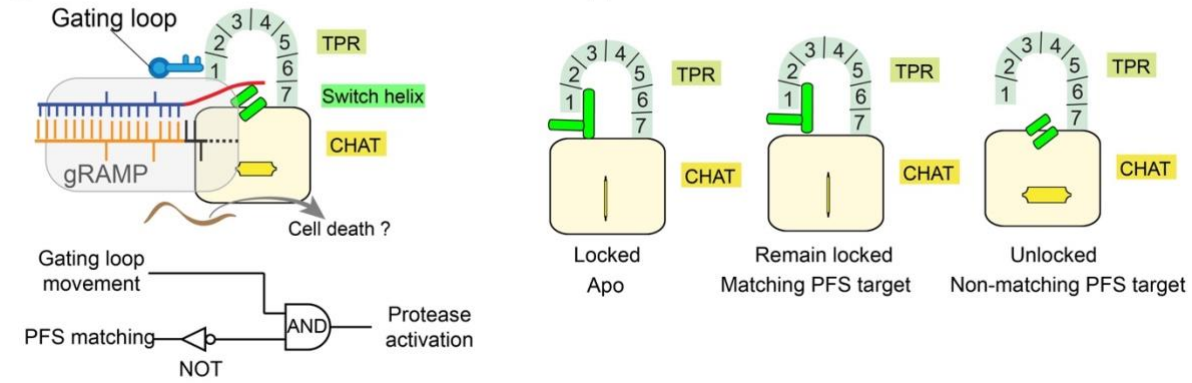
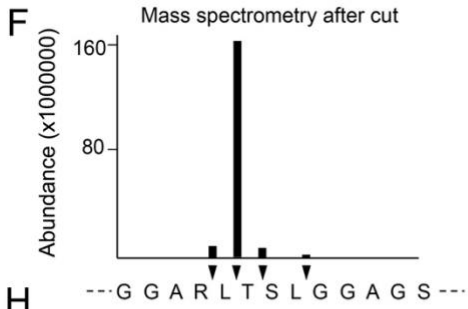
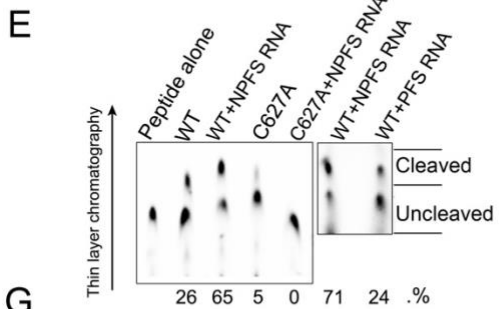
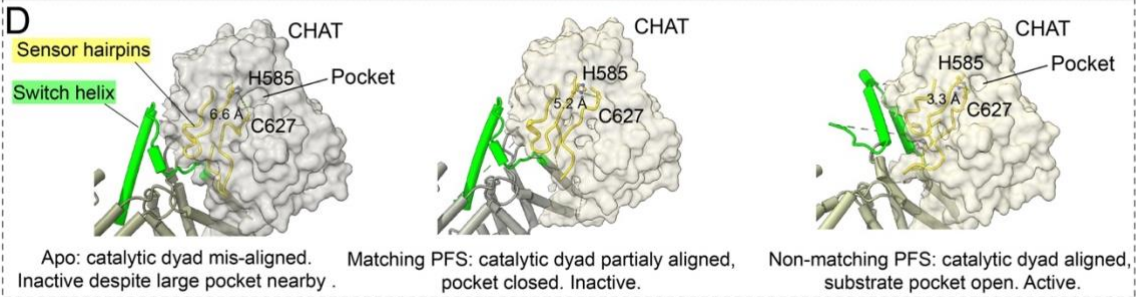
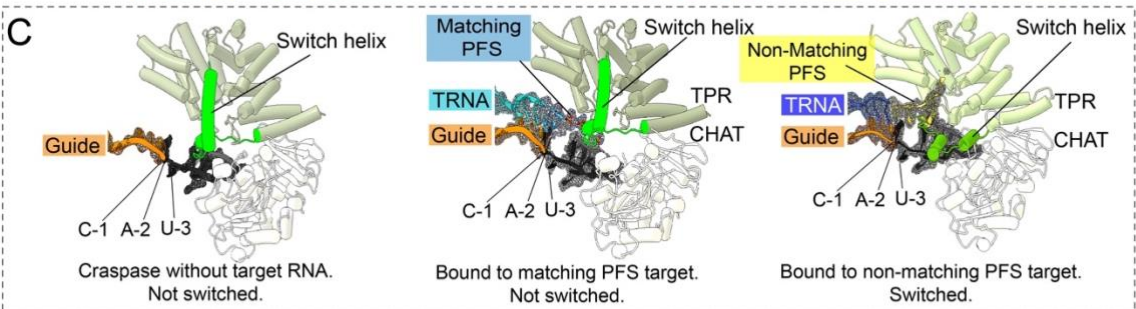
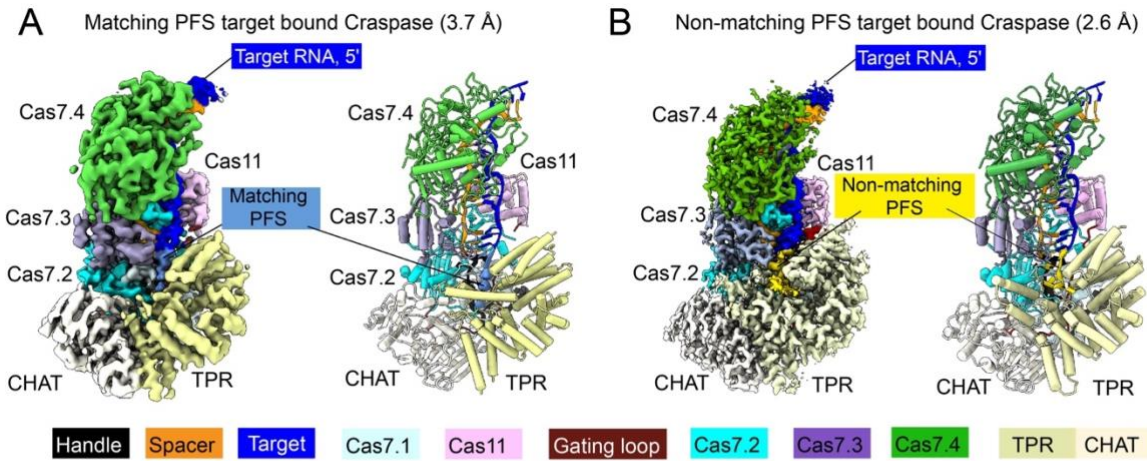


Fig. 5. Structural basis for Craspase protease activation. (A) 3.7 Å cryo-EM density (left) and structural model (right) of matching PFS RNA bound Craspase. **(B)** 2.6 Å cryo-EM density (left) and structural model (right) of non-matching PFS RNA bound Craspase. **(C)** Close-up views of switch helix in resting state (left), matching PFS RNA bound state (middle), and non-matching PFS RNA bound state (right). Switch helix highlighted in green and the density of crRNA and target RNA (TRNA) are shown in mesh. **(D)** Conformation of the switch helix and sensor hairpin in three states. Changing status in the catalytic dyad and the nearby side-chain binding pocket in CHAT (grey surface) highlighted. **(E)** TLC-based peptide cleavage assay by Craspase. **(F)** Cleavage site mapping by mass-spectrometry. **(G)** Top: model depicting non-matching PFS RNA induced Craspase activation. Bottom: Logic gate diagram illustrating the protease activation mechanism. **(H)** Model depicting TPR-CHAT status in the apo/resting, matching PFS RNA bound state, and non-matching PFS RNA bound states.

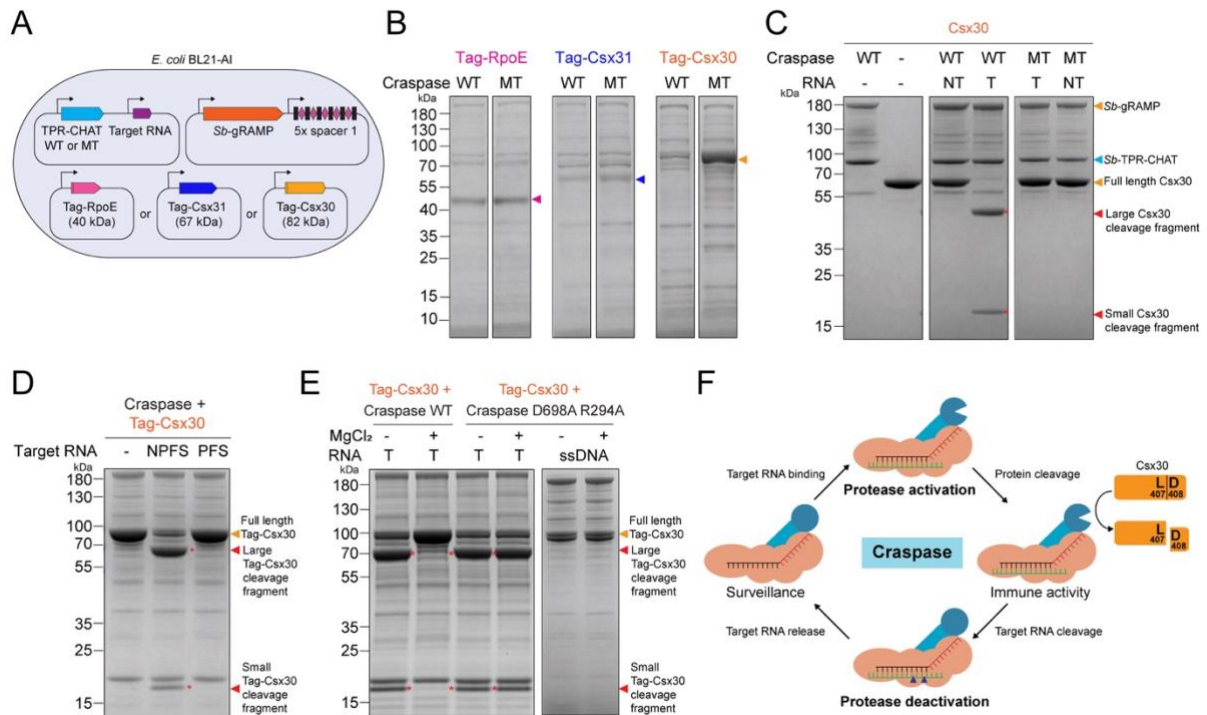


Fig. 6. Craspase proteolytically cleaves Csx30 in an RNA-dependent manner. (A) Genetic context for RpoE, Csx31 and Csx30 co-expression with Craspase wild-type (WT) or mutant (MT; H585A C627A) and a target RNA in *E. coli* BL21-AI. **(B)** Protein gel showing the eluted protein content from Streptavidin purifications of Tag-RpoE, Tag-Csx31 and Tag-Csx30 after co-expression with either Craspase WT or Craspase MT (H585A C627A). Colored arrows indicate the expected size for full length protein. **(C)** Protein gels after Craspase WT or Craspase MT (H585A C627A) incubation with Csx30 in the presence of target RNA or non-target RNA. Protein cleavage products are indicated with a red asterisk. **(D)** Protein gel after Craspase WT incubation with target RNA containing either a non-matching PFS (NPFS) or matching PFS (PFS). **(E)** Left: protein gel after incubation of Tag-Csx30 with target RNA and Craspase WT or Craspase D698A R294A, with or without prior incubation with MgCl₂. Right: protein gel after incubation of Tag-Csx30 with target ssDNA and Craspase D698A R294A. **(F)** Model for Craspase functionality. Once unbound Craspase has bound a target RNA, the peptidase activity is activated. This results in proteolytic cleavage of Csx30 between L407 and D408. Upon target RNA cleavage by Craspase, the peptidase activity is shut off.

Supplementary Materials for

Craspase is a CRISPR RNA-guided, RNA-activated protease

Authors: Chunyi Hu^{1, †}, Sam P. B. van Beljouw^{2,3, †}, Ki Hyun Nam⁴, Gabriel Schuler¹, Fran Ding¹, Yanru Cui¹, Alicia Rodríguez-Molina^{2,3}, Anna C. Haagsma^{2,3}, Menno Valk^{2,3}, Martin Pabst^{2,3}, Stan J.J. Brouns^{2,3,*}, Ailong Ke^{1,*}

† These authors contributed equally.

* Correspondence to ailong.ke@cornell.edu, stanbrouns@gmail.com

This PDF file includes:

Materials and Methods

Figs. S1 to S22

Tables S1-S5

Captions for Movies S1-S7

Other Supplementary Materials for this manuscript include the following:

Movies S1-S7

Materials and Methods

Cloning, Expression, and Purification

Plasmids used in this study are listed in **Table S5**. Primers described in **Table S5** were used for PCR amplification using the Q5 high-fidelity Polymerase (New England Biolabs). Ordered DNA sequences are listed in **Table S5**. All plasmids were verified by Sanger-sequencing (Macrogen Europe, Amsterdam, The Netherlands). Cloning was performed using NEBuilder HiFi DNA Assembly (New England Biolabs) unless stated otherwise. Bacterial transformations for cloning were performed using NEB® 5-alpha Competent *E. coli* (New England Biolabs) and carried out by electroporation using ECM630 Electrocell Manipulator (2.5 kV, 200 Ω , 25 μ F).

For Craspase expression, pSB-GRAMP, pCRISPR1, pSB-GRAMP_CRISPR1, pSB-GRAMP_CRISPR1_target1 and TPR-CHAT were used (11). For *Sb*-gRAMP-crRNA expression, the pSB-GRAMP_CRISPR1 was transformed into BL21(DE3) cells. A single colony was picked and grown for overexpression in 4 liters of LB media supplemented with streptomycin (add concentration here). Over expression was induced by adding isopropyl- β -D-thiogalactopyranoside (IPTG) to a final concentration of 0.5 mM and incubation at 16°C overnight. Cells were collected by centrifugation at 5000 rpm on J6 centrifuge and lysed by sonication in buffer A (200 mM NaCl, 50 mM HEPES pH 7.5, 2 mM TCEP, 10% glycerol) with 1 mM phenylmethylsulfonyl fluoride (PMSF). The lysate was centrifuged at 12,000 rpm for 60 minutes at 4°C, and the supernatant was filtered through a 0.45 μ m syringe filter and loaded onto 5 ml of pre-equilibrated Strep-Tactin @XT Affinity Resin (IBA Lifesciences GmbH). The loaded resin was washed with 25 ml of buffer A and the protein eluted by 20 ml buffer A with 2.5 mM dethio-biotin. The elution was concentrated and further purified by size-exclusion chromatography (Superdex 200 Increase 10/300 GL; Cytiva) equilibrated with buffer B (175 mM NaCl, 25 mM HEPES pH 7.5). The second size-exclusion chromatography peak was collected, concentrated, and flash frozen with liquid nitrogen.

For Craspase expression, the pSB-GRAMP-CRISPR plasmid was co-transformed into BL21(DE3) with pTPR-CHAT plasmid (8). A single colony was picked and grown for expression in 4 liters of LB media. Expression was induced by adding IPTG to a final concentration of 0.5 mM and incubation at 16°C overnight. Cells were collected by centrifugation and lysed by sonication in buffer A (200 mM NaCl, 50 mM HEPES pH 7.5, 2 mM TCEP, 10% glycerol) with 1 mM phenylmethylsulfonyl fluoride (PMSF). The lysate was centrifuged at 12,000 rpm. for 60 minutes at 4°C, and the supernatant was filtered through a 0.45 μ m syringe filter and loaded onto 5 ml of pre-equilibrated Strep-Tactin @XT Affinity Resin (IBA Lifesciences GmbH). The loaded resin was washed with 20 ml buffer A and eluted by 25 ml buffer A with 2.5 mM dethio-biotin. The elution was then loaded onto 3 ml of pre-equilibrated Ni-NTA resin (Qiagen). After washing with 15 ml of buffer A, the sample was eluted by 15 ml buffer A with 300 mM imidazole. This eluted sample was concentrated and further purified by size-exclusion chromatography (Superdex 200 Increase 10/300 GL;

Cytiva) equilibrated with buffer B (175 mM NaCl, 25 mM HEPES pH 7.5). The peak was collected, concentrated, and flash frozen with liquid nitrogen.

To construct pTag-Csx30, pTag-Csx31 and pTag-RpoE, a coding sequence corresponding to an *E. coli* codon-optimized Csx30, Csx31 and RpoE proteins were designed, ordered (Life Technologies Europe BV) and cloned into the plasmid pGFPuv using NEBuilder HiFi DNA Assembly (New England Biolabs), combined with a cloned fragment encoding the LacI repressed T7 promoter followed by a N-terminal Twin-Strep-Tag II and a SUMO-tag. For the construction of pTag-Csx30 mutants, primers including the desired mutation were used with pTag-Csx30 as backbone for PCR and subsequent HiFi assembly.

To construct pTPR-CHAT-target1, pTPR-CHAT was enriched with a sequence encoding for target RNA complementary to crRNA1 under control of the IPTG inducible T7 promoter, using NEBuilder HiFi DNA Assembly (New England Biolabs).

Purification of Csx30, Csx31 and RpoE overexpressed together with Craspase.

Plasmid pSB-GRAMP_CRISPR1, pTPR-CHAT and one of the following three (pTag-RpoE, pTag-Csx31 or pTag-Csx30) were transformed in electrocompetent *E. coli* BL21(AI) cells and grown overnight on selection media (100 µg/mL spectinomycin, 25 µg/mL chloramphenicol, 100 µg/mL ampicillin). Colonies were streaked from the plate and grown in 200 mL LB medium containing antibiotics (100 µg/mL spectinomycin, 25 µg/mL chloramphenicol, 100 µg/mL ampicillin) in baffled flasks at 37°C and 150 rpm until they reached exponential phase (OD₆₀₀ 0.3-0.5). The grown cultures were incubated on ice for 1 hour and protein overexpression was induced with a final concentration of 0.2% L-arabinose and 0.5 mM IPTG followed by overnight incubation at 20 °C and 150 rpm. Cells were collected by centrifugation at 16000 rpm at 4°C. The supernatant was discarded and the pellets were resuspended in PBS (50 mL PBS/initial 1 L culture) and harvested by centrifugation (30 minutes, 3900 rpm 4 °C). The supernatant was discarded, and the pellets stored at -80°C until further use.. Bacterial cell pellets of each 200 mL culture were resuspended in 10 mL of ice-cold lysis buffer (100 mM Tris-HCl, 150 mM NaCl, 1 mM DTT, 5% glycerol, pH 7.5). The cells were lysed by sonication (2 minutes, 30 sec on 30 sec off, amplitude 30%). The lysate was centrifuged at 16,000 rpm for 30 minutes at 4°C, and the supernatant was filtered through a 0.45 µm syringe filter and loaded onto 0.25 ml (column bed volume) of pre-equilibrated Strep-Tactin®XT Affinity Resin (IBA Lifesciences GmbH). The loaded resin was washed with 10 column volumes of ice-cold wash buffer (100 mM Tris-HCl, 150 mM NaCl, 1 mM DTT, 5% glycerol, pH 7.5) and eluted in 750 µL of elution buffer (100 mM Tris-HCl, 150 mM NaCl, 1 mM DTT, 5% glycerol, 50 mM Biotin, pH 7.5).

Purification of Csx30 wild-type and Csx30 mutants for cleavage experiments

The plasmid pTag-Csx30 was transformed in electrocompetent *E. coli* BL21(AI) cells and grown overnight on selection media (100 µg/mL ampicillin). Colonies were streaked from the plate and grown in 4L or 8L of LB medium containing antibiotics (100 µg/mL ampicillin) in baffled flasks at 37°C and 150 rpm until they reached exponential phase (OD₆₀₀ 0.3-0.5). The grown cultures were incubated on ice for 1 hour and protein overexpression was induced with a final concentration of 0.2% L-arabinose and 0.5 mM IPTG followed by overnight incubation at 20 °C and 150 rpm. Cells were collected by centrifugation at 16000 rpm at 4°C. The supernatant was discarded and the pellets were resuspended in PBS (50 mL PBS/initial 1 L culture) and harvested by centrifugation (30 minutes, 3900 rpm 4 °C). The supernatant was discarded, and the pellets stored at -80°C until further use. Bacterial cell pellets were resuspended in ice-cold lysis buffer (100 mM Tris-HCl, 150 mM NaCl, 1 mM DTT, 5% glycerol, pH 7.5), 50 ml of buffer/1L initial culture. 1 tablet of cOmplete™ EDTA-free Protease Inhibitor Cocktail was added per 50 mL resuspended pellet. The cells were lysed with 3 runs at 1000 bar in a cooled French press. The lysate was centrifuged at 16,000 rpm for 30 minutes at 4°C, and the supernatant was filtered through a 0.45 µm syringe filter and loaded onto pre-equilibrated Strep-Tactin®XT Affinity Resin (IBA Lifesciences GmbH), 1.5 mL column bed volume/4L initial volume. The loaded resin was washed with 10 column volumes of ice-cold wash buffer (100 mM Tris-HCl, 150 mM NaCl, 1 mM DTT, 5% glycerol, pH 7.5) and eluted in 750 µL of elution buffer (100 mM Tris-HCl, 150 mM NaCl, 1 mM DTT, 5% glycerol, 50 mM Biotin, pH 7.5).

For removal of the Csx30 purification Strep-SUMO tag, Tobacco Etch Virus (TEV) protease (Sigma Aldrich; T4455) was added for overnight incubation at 4°C, followed by affinity chromatography containing HIS-Select Nickel Affinity Gel (Sigma-aldrich) to remove the TEV protease. The collected flow-through was subjected to size exclusion chromatography using Superdex 200 Increase 10/300 GL (Cytiva) column equilibrated with running buffer (100 mM Tris-HCl, 150 mM NaCl, 1 mM DTT, 5% glycerol, pH 7.5) with 0.3 mL/min flow rate using running buffer as mobile phase. Pooled fractions were concentrated, flash frozen in liquid nitrogen and stored at -80 °C until further use.

In vitro target RNA and non-target RNA generation

gBlocks (Table S5) containing the T7 promoter and target RNA (complementary to CRISPR1) or non-target RNA (not complementary to CRISPR1) were synthesized (IDT) and PCR amplified with 5'-TCGATCAGAGCGCTCTTACG and 5'-GGTCCAGTTCAAACACTCCC. ~500 ng of purified PCR fragment was *in vitro* transcribed overnight using the HiScribe™ T7 High Yield RNA Synthesis Kit (NEB) and subsequently treated with DNase I according to the manufacturer's protocol. For RNA extraction, acidic phenol (pH 4.5, phenol:chloroform = 5:1, Invitrogen) was added to the sample in a 1:1 ratio, vortexed for 1 minute and centrifuged for 10 minutes at 13,200 rpm at room temperature. The aqueous phase was collected and subjected to RNA precipitation (20 µL 3M NaAcetate and 500 µL 100% ethanol per 200 µL of sample) for 1 hour at -20 °C. Samples were

centrifuged at 13,200 rpm at 4 °C for 2 hours, washed twice with ice-cold 70% ethanol and centrifuged at 13,200 rpm at 4 °C for 10 minutes. The pellet was dried in a SpeedVac concentrator (Thermo Fisher Scientific) for 30 minutes at 60 °C and resuspended in RNA grade water. The four variants of target RNA were mixed in an equimolar ratio before usage in Csx30 protein cleavage reactions.

RNA cleavage Assays

20 µL reactions were prepared where 20 nM Cy5 labeled target RNA (**Table S5**) was incubated with *Sb*-gRAMP RNP in cleavage buffer (100 mM KCl, 50 mM HEPES pH 7.5, 2 mM βME, 5 mM MgCl₂) and incubated at room temperature for 30 min (unless otherwise specified). The 20 µL reactions were quenched with the addition of EDTA to 150 mM (final concentration) and 1:1 volume of 100% formamide. Samples were heated to 95 °C for 10 minutes and run on 12% urea-PAGE gel. Fluorescent signals were imaged using ChemiDoc (BioRad) and quantified using Image Lab.

For the RNA cleavage experiments using varying lengths of complementarity in the target RNA, 10 µL reactions containing 200 nM *Sb*-gRAMP RNP with 100 nM target RNA was used in an alternative cleavage buffer (25 mM Tris-HCl, 150 mM NaCl, 10 mM DTT and 2 mM MgCl₂). Reactions were incubated at 20 °C for 2 hours, after which 0.5 µL of 800 units/mL proteinase K (New England Biolabs) was added for 1 hour at 37 °C. Reactions were heat inactivated at 95 °C for 5 minutes, followed by mixing with 2x RNA loading dye (95% formamide, 0.025% SDS and 0.5 mM EDTA) and loaded on an 8M urea 10% PAGE gel (pre-run at 350 V for 1 hour, sample run at 333V for 2 hours)

RNA knock down assay in *E.coli*

p*SB*-GRAMP wild type or mutants (Spec^R), pCRISPR_GFP guide wild type or repeat region mutants (Kana^R) and pGFP (Amp^R) were co-transformed into *E.coli* BL21(DE3) cells and plated on LB-agar plates with appropriate antibiotics. Transformation plates were incubated for 20 hours at 37°C and then scanned via GFP channel using a ChemiDoc (BioRad) (Figure S1D-E). For the dot assay, single colonies were picked after transformation and cultured in 3 ml LB media with appropriate antibiotics for 18 hours in 37 °C. Then adjusted all cultures to the same OD at 0.1. 10 µL from each culture was pipetted on a plastic membrane. Fluorescent signals were imaged using a ChemiDoc (BioRad) via 515 nm to monitor GFP signal and 600 nm to monitor cell density.

Electrophoretic mobility shift assay

5 nM final concentration of fluorescently labeled target RNA was incubated with specified concentration of *Sb*-gRAMP or Craspase complex in a 20 µL reaction containing binding buffer (50 mM Tris pH 8.0, 150 mM NaCl, 10% glycerol). After a 20-minute incubation on ice (unless otherwise specified), 10 µL of each sample was loaded onto 1% agarose gel equilibrated in 0.5 x TBE buffer. Electrophoresis was performed at 60 V for 30 min at 4°C. Fluorescent signals were recorded using a ChemiDoc (Bio-Rad).

Peptide cleavage assay

500 ng FAM labeled synthesized peptides (GenScript) were dissolved in 500 μ L buffer A (150 mM NaCl, 25 mM HEPES pH 7.5, 5% glycerol) to a final concentration of 1 mM. Peptides were further diluted to 100 μ M before performing the assay. 2 μ L of the peptide was mixed with 3 μ L of Craspase RNP (1 μ M final concentration) with pre-incubated target RNA (4 μ M final RNA concentration when added) and incubated at 37 °C for 1 hour. 2 μ L of reaction was applied to a thin layer chromatography plate (K6 silica gel, catalogue No: 4860-820). Thin layer chromatography (TLC) plate was put in a sealing glass tank with 3 cm of acetone for 30 min. After chromatography, FAM signals on the plate were imaged using a ChemicDoc (Bio-Rad).

For GST-AK2-P3C fusion protein cleavage assay, mixed 3 μ g fusion protein with 2.5 μ g Craspase (if with target RNA pre-incubated complex, RNA concentration is 4 μ M) and incubated at 37 °C for 2 hours. Next, 4 μ L of 5x SDS-loading dye was added and reaction was heated in 95 °C for 10 min. 8 μ L of reaction was loaded and run on a 12% SDS-PAGE gel for analysis.

Cryo-EM sample preparation

Sb-gRAMP was incubated with the specified target RNA in cryo-EM buffer (150 mM NaCl, 25 mM HEPES pH 7.5) for 15 minutes at room temperature. RNA was supplied at a 3-fold molar excess to *Sb*-gRAMP (0.5mg/mL final concentration). 3.5 μ L of the incubation was applied to a Quantifoil holey carbon grid (1.2/1.3, 200 mesh) which had been glow-discharged with 20 mA at 0.39 mBar for 30 seconds (PELCO easiGlow). Grids were blotted with Vitrobot blotting paper (Ted Pella Inc STANDARD VITROBOT FILTER PAPER; Cat# 47000100) for 3 seconds at 4 °C, 100% humidity, and plunge-frozen in liquid ethane using a Mark IV FEI/Thermo Fisher Vitrobot.

EM data acquisition

Data was collected on a 200 kV Talos Arctica (Thermo Scientific) or 300 kV Krios G3i Cryo Transmission Electron Microscope (Thermo Scientific) with Gatan K3 direct electron detector. The total exposure time of each movie stack led to a total accumulated dose of 50 electrons per \AA^2 which fractionated into 50 frames without beam tilt. Dose-fractionated super-resolution movie stacks collected from the Gatan K3 direct electron detector were binned to a pixel size of 1.1 \AA . The defocus value was set between $-1.0 \mu\text{m}$ to $-2.5 \mu\text{m}$.

Image processing and 3D reconstruction

Motion correction, CTF-estimation, blob particle picking, 2D classification, 3D classification and non-uniform 3D refinement were performed in CryoSPARC v.2 (30). Refinements followed a standard procedure, 100 classes of 2D classification was performed in CryoSPARC. High quality 2D classes were hand-picked to do 3D classifications in *C1* symmetry. CryoSPARC was instructed to generate eight initial models in 3D classification for each reconstruction. After heterologous refinement, the promising 3D models was hand-

picked for post 3D refinement, as outlined in the supplemental figures. A solvent mask was generated in RELION (31) with 0.1 contour level and was used for all subsequent local refinement steps. CTF post refinement was conducted to refine the beam-induced motion of the particle set, resulting in the final maps. The detailed data processing and refinement statistics for cryo-EM structures are summarized in supplemental figures and **Table S1**.

Atomic model building

Different modeling procedures were used for the gRAMP complexes with RNA and TPR-CHAT. For the gRAMP/Non-matching PFS target cryo-EM map, the gRAMP sequence was used to generate an AlphaFold2 prediction (22), which was then split into domains and individually docked into the cryo-EM map using UCSF Chimera (32). Model building was completed through iterative cycles of manual building using Coot (33) and real space and positional refinements using Phenix (34). Notably, the cryo-EM density for the big insertion domain did not allow de novo model building despite efforts to improve the local resolution. An AlphaFold2 predicted structure was docked into the EM density to model BID. In other structures was built and refined using a similar strategy. The detailed statistics are documented in **Table S1**.

Model Validation

Map-model Fourier Shell Correlation (FSC) was computed using Mtriage in Phenix (34). Map-model FSC resolution of each dataset was estimated from Mtriage FSC curve, using 0.143 cutoff. The masked cross-correlation (CCmask) from Mtriage was reported as representative model-map cross-correlation. Model geometry was validated using the MolProbity (35). All the deposited models were submitted to MolProbity server to check the clashes between atoms, Ramachandran-plot, bond-angles, bond-lengths, sidechain rotamers, CaBLAM and C-beta outliers. All the model validation stats are summarized in **Table S1**.

In vitro Csx30 cleavage reactions

Csx30 cleavage reactions were performed in 10 μ L reaction volume, containing purified 2225 nM Craspase (WT, MT (TPR-CHAT H585A C627A) or MT (D698A R294A), without SUMO tag (Fig. 5C) or with SUMO tag (Fig. 5E and 5F), 5 μ M (for incubation with Craspase D698A R294A) or 11 μ M (for incubation with target RNA containing matching or non-matching PFS) DualStrep-SUMO-TEV-Csx30 protein (Fig. 5E and 5F) or 4 μ M tag-less Csx30 protein (Fig. 5C, 900 ng in vitro generated target RNA or non-target RNA or 3 μ M target RNA containing matching or non-matching PFS, 100 mM Tris, 150 mM NaCl, 10 mM DTT, 0 mM or 2 mM $MgCl_2$ (Fig. 5C reactions contain 2 mM $MgCl_2$, Fig. 5E was incubated with 90 ng of target RNA and 2 mM $MgCl_2$ for 2 hours at 37 °C prior to addition of 11 μ M DualStrep-SUMO-TEV-Csx30 protein). Reactions were run for 1 hour at 37 °C. Afterwards, the reactions were supplemented with 10 μ L MilliQ water, 5 μ L of 5X Laemmli buffer (375 mM Tris-HCl, 9% SDS, 50% glycerol, 0.03% bromophenol blue) and 2.5 μ L 1 M DTT, and incubated at 95 °C for 10 minutes before loading on a 4-20% surePAGE™ Bis-Tris protein

gel (GenScript). Gels were run in 1X MOPS buffer (GenScript) at 200 V for 30-45 minutes, washed in MilliQ water and stained for at least 2 hours with BioSafe Coomassie G-250 stain (Bio-Rad) under continue shaking. Gels were washed in MilliQ water for 4 hours before imaging.

Mass spectroscopy to confirm the identity of the Csx30 cleavage fragments and to map the Craspase cleavage site

To identify the Csx30 protein fragments, bands of interest (large Csx30 cleavage fragment, ~47 kDa and small Csx30 cleavage fragment, ~19 kDa) were cut from the gel and minced into small pieces using a sterile scalpel. Gel pieces were destained using Coomassie destaining solution (100 mM ammonium bicarbonate in 40% acetonitrile) for 15 minutes at 37 °C and shaking at 300 rpm. A reduction was performed using 200 µL of reducing agent (10 mM dithiothreitol) and incubation for 30 minutes at 56 °C. After removal of the reducing agent and cooling down of the gel pieces to room temperature, 200 µL of alkylating solution (55 mM iodoacetamide) was added and incubated in the dark at room temperature for 30 minutes. After removal of the alkylation solution, 200 µL of Coomassie destaining solution was added and incubated for 5 minutes at room temperature with 300 rpm shaking. The solution was discarded and 200 µL of acetonitrile (100%) was added and incubated for approximately 10 minutes at room temperature until the gel pieces were dehydrated. Proteolytic in-gel digestion was initiated by adding 2 µL of a 100 ng/µL trypsin or chymotrypsin solution (Promega, sequencing grade). Samples were incubated overnight at 37°C with 300 rpm shaking using an Eppendorf ThermoMixer. The next day, samples were spun down and 150 µL of extraction solution (70% acetonitrile, 5% formic acid) was added to the supernatant and incubated for 15 minutes at 37°C with 300 rpm shaking. The supernatant was collected, 100 µL of acetonitrile (100%) was added and incubated for 15 minutes at 37°C with 300 rpm shaking. Next, 100 µL of 10:90 (v/v) acetonitrile:water was added to the samples and incubated for 15 minutes at 37°C with 300 rpm shaking. The supernatant was collected and dried using a SpeedVac concentrator (Thermo Fisher Scientific). Before spectrometry analysis, the dried samples were resuspended in 15 µL resuspension buffer (3% acetonitrile, 0.1% formic acid) under careful vortexing. An aliquot corresponding to approximately 100 ng protein digest was analyzed using a nano-LC (EASY 1200, Thermo Fisher Scientific, Germany) equipped with an Acclaim PepMap RSLC RP C18 separation column (50 µm x 150 mm, 2 µm), coupled online to a QE plus Orbitrap mass spectrometer (Thermo Fisher Scientific, Germany).

The flow rate was maintained at 350 nL/min over a linear gradient from 5% to 30% solvent B over 38 minutes, and finally to 60% B over 15 minutes, followed by back equilibration to starting conditions. Solvent A was H₂O containing 0.1% formic acid, and solvent B consisted of 80% acetonitrile in H₂O and 0.1% formic acid. The Orbitrap was operated in data depended acquisition mode acquiring peptide signals from 385-1250 m/z at 70 K resolution with a max IT of 100 ms and an AGC target of 3e6. The top 10 signals were isolated at a

window of 2.0 m/z and fragmented using a NCE of 28. Fragments were acquired at 17 K resolution with a max IT of 75 ms and an AGC target of 2e5.

Mass spectrometric raw data were analyzed using PEAKS Studio X (Bioinformatics Solutions Inc., Canada) by comparing the obtained peptide fragmentation spectra to a constructed database (retrieved from the UniProtKB, www.uniprot.org) containing the Csx30 protein sequence and relevant background proteins. The database searching was performed analyzing either for trypsin cleaved peptides, or in case of mapping the Craspase cleaved peptides for fully non-specific cleaved variants of the Csx30 protein sequence (**Tables S2-S4**). The search allowed for 20 ppm parent ion and 0.02 m/z fragment ion mass error, carbamidomethylation as fixed and methionine oxidation and N/Q deamidation as variable modifications. Peptide matches and protein identification were filtered for 1% false discovery rate.

Supplemental Figures

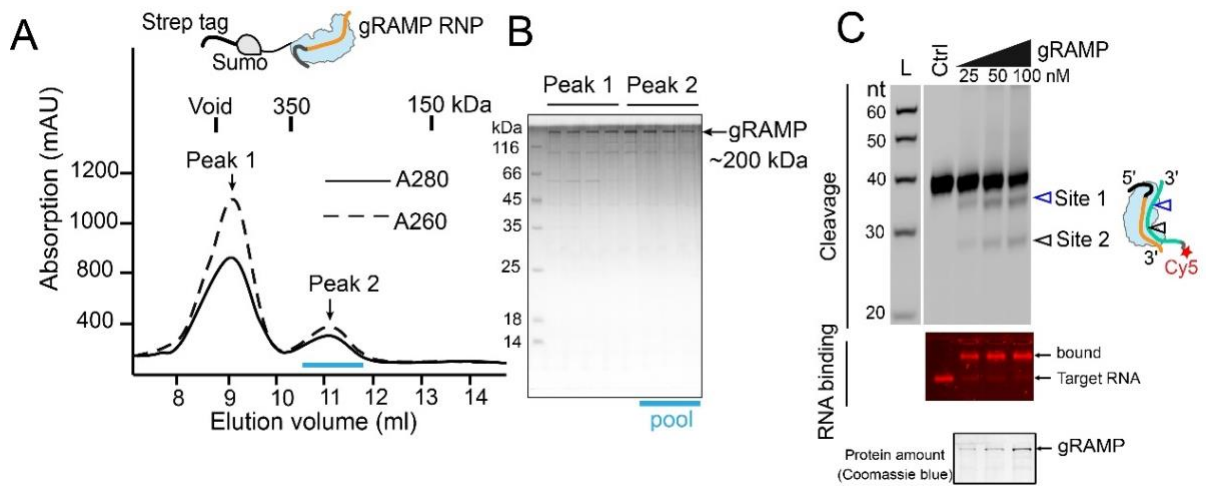


Fig. S1. Reconstitution and biochemical characterization of the *Sb*-gRAMP RNP.
(A) Purification profile on size-exclusion chromatography. **(B)** SDS-PAGE analysis of the peaks on size-exclusion. **(C)** Top: cleavage assay for different concentrations of *Sb*-gRAMP. Middle: EMSA assay using the same titration of *Sb*-gRAMP. Bottom: SDS-PAGE showing protein concentration in cleavage and EMSA assay.

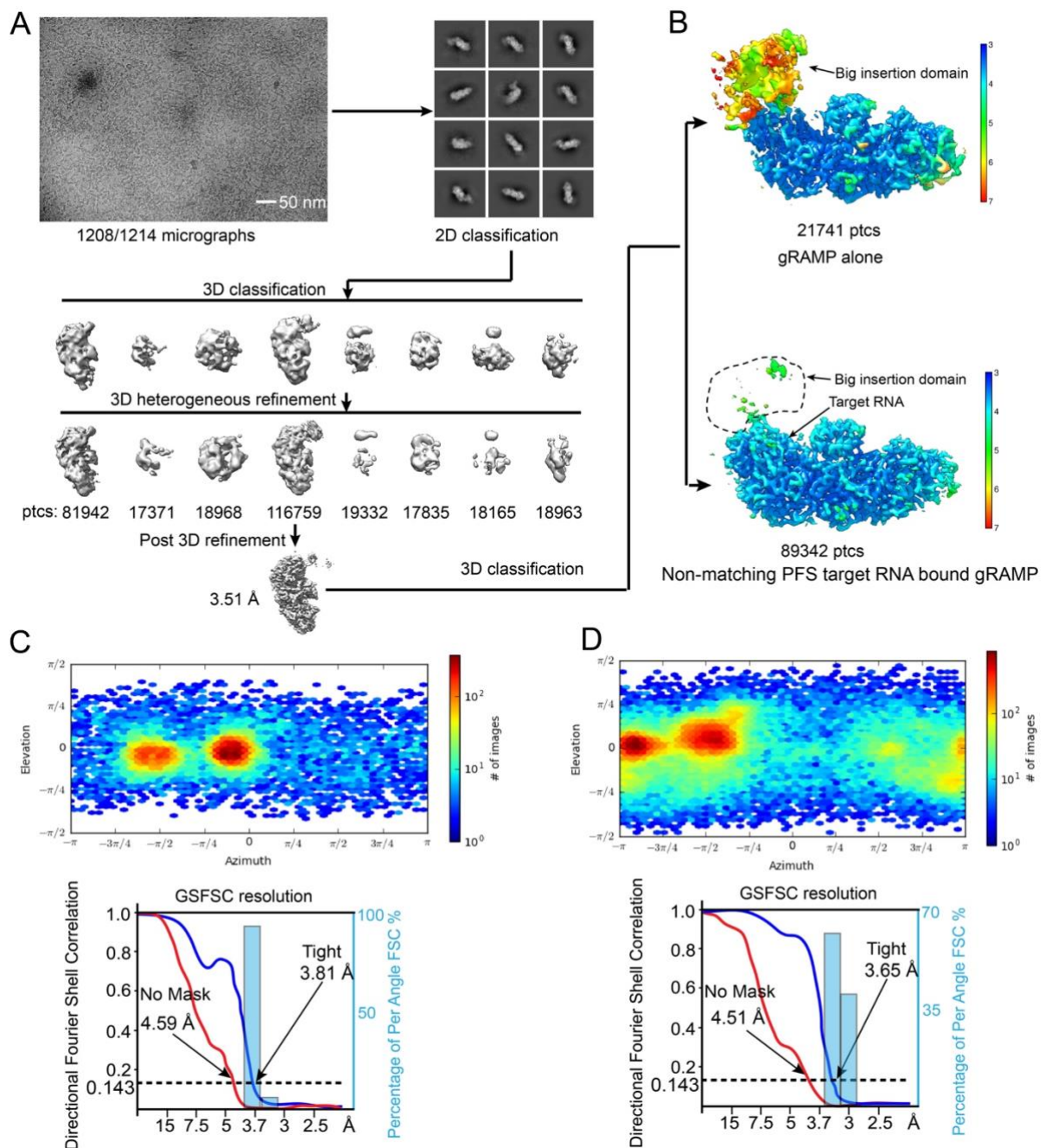


Fig. S2. Single particle cryo-EM reconstruction of *Sb*-gRAMP in resting and non-matching PFS RNA bound states.

(A) Workflow of the cryo-EM image processing and 3D reconstruction for the non-matching PFS RNA bound *Sb*-gRAMP. A portion of the single particles did not bind RNA. They gave rise to the resting state *Sb*-gRAMP reconstruction. (B) Final cryo-EM density map showing the local resolution distribution of the two reconstructions. (C, D) 3D Euler distribution plot (top panel) and Fourier Shell Correlations (FSC; bottom panel) of *Sb*-gRAMP in the resting and NPFS bound states, respectively. The gold-standard cutoff (FSC = 0.143) was marked with a dotted line.

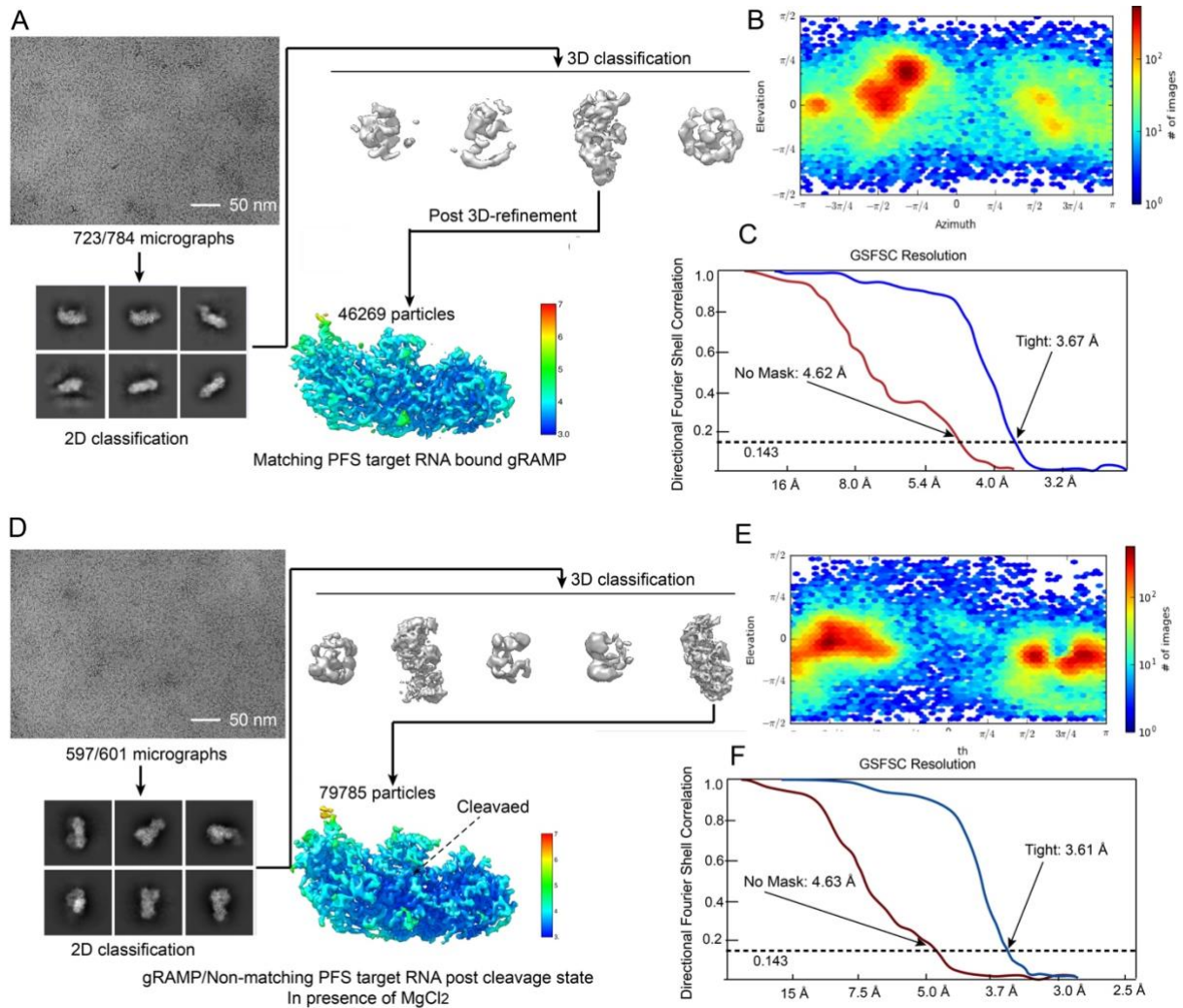


Fig. S3. Single particle cryo-EM reconstruction of *Sb*-gRAMP in Matching PFS state and $MgCl_2$ -incubation induced post-cleavage state.

(A) Workflow of the cryo-EM image processing and 3D reconstruction for the *Sb*-gRAMP in matching PFS RNA bound state. The local resolution distribution is colored on the final EM density map. (B) 3D Euler distribution plot revealing the representation of the single particle orientation in the final reconstruction. (C) Fourier Shell Correlation defined reconstruction resolution (FSC). The dotted line indicates the final resolution defined by the gold-standard FSC cutoff (0.143) (D) Workflow of the cryo-EM image processing and 3D reconstruction for the *Sb*-gRAMP in the post-cleavage state, induced by $MgCl_2$ incubation on a Non-matching PFS RNA substrate. The local resolution distribution is colored on the final EM density map. (E) 3D Euler distribution plot of the post-cleavage state. (F) FSC defined resolution of the post-cleavage state reconstruction.

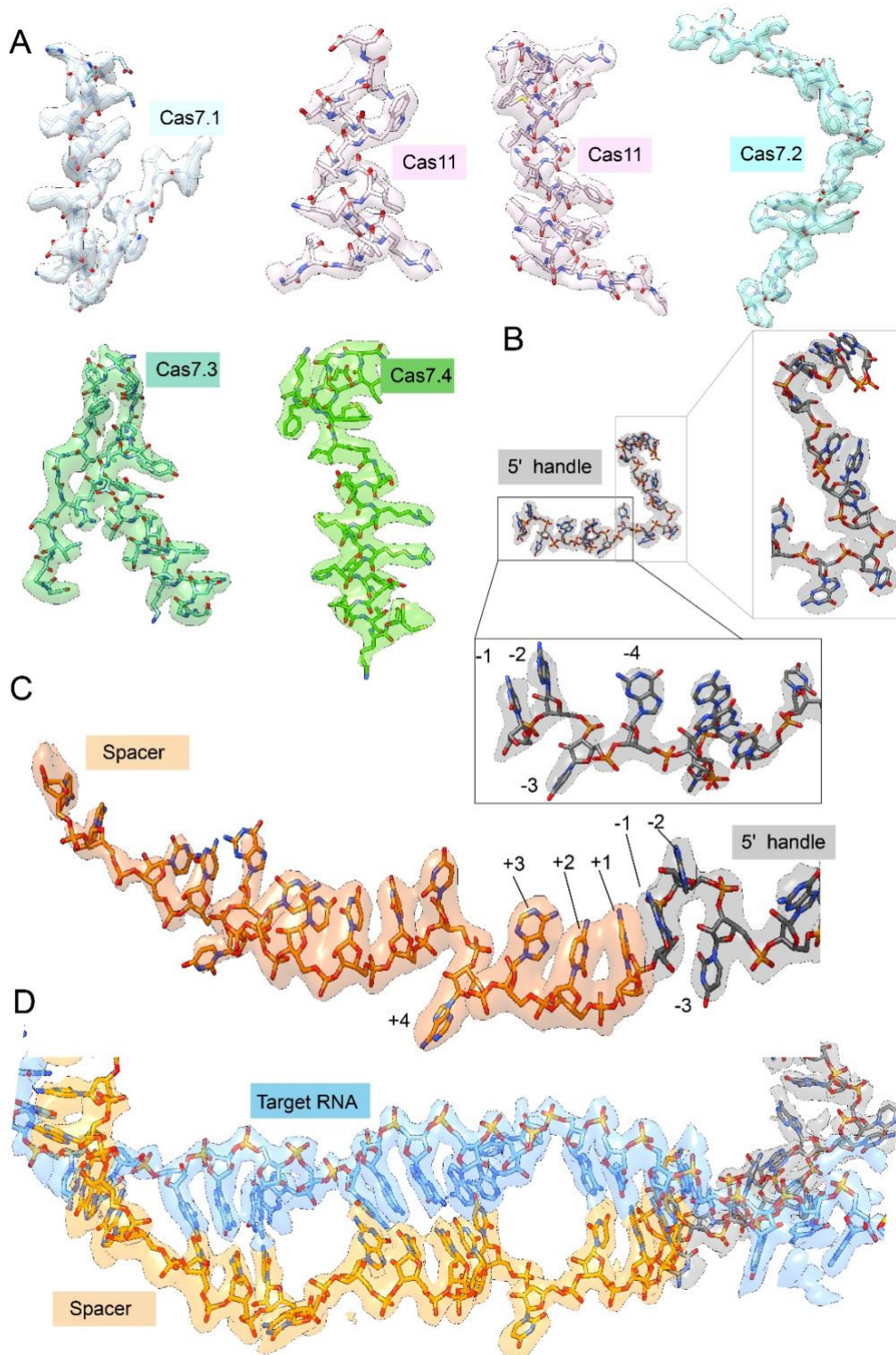


Fig. S4. Representative local map density for the different functional states.

(A) EM densities for representative protein regions inside *Sb*-gRAMP and *Sb*-gRAMP/RNA complex. **(B)** EM densities for the 5' handle region of the crRNA. The number indicates the base order. **(C)** EM densities for guide RNA region inside *Sb*-gRAMP. **(D)** EM densities for the duplex of target RNA-guide RNA.

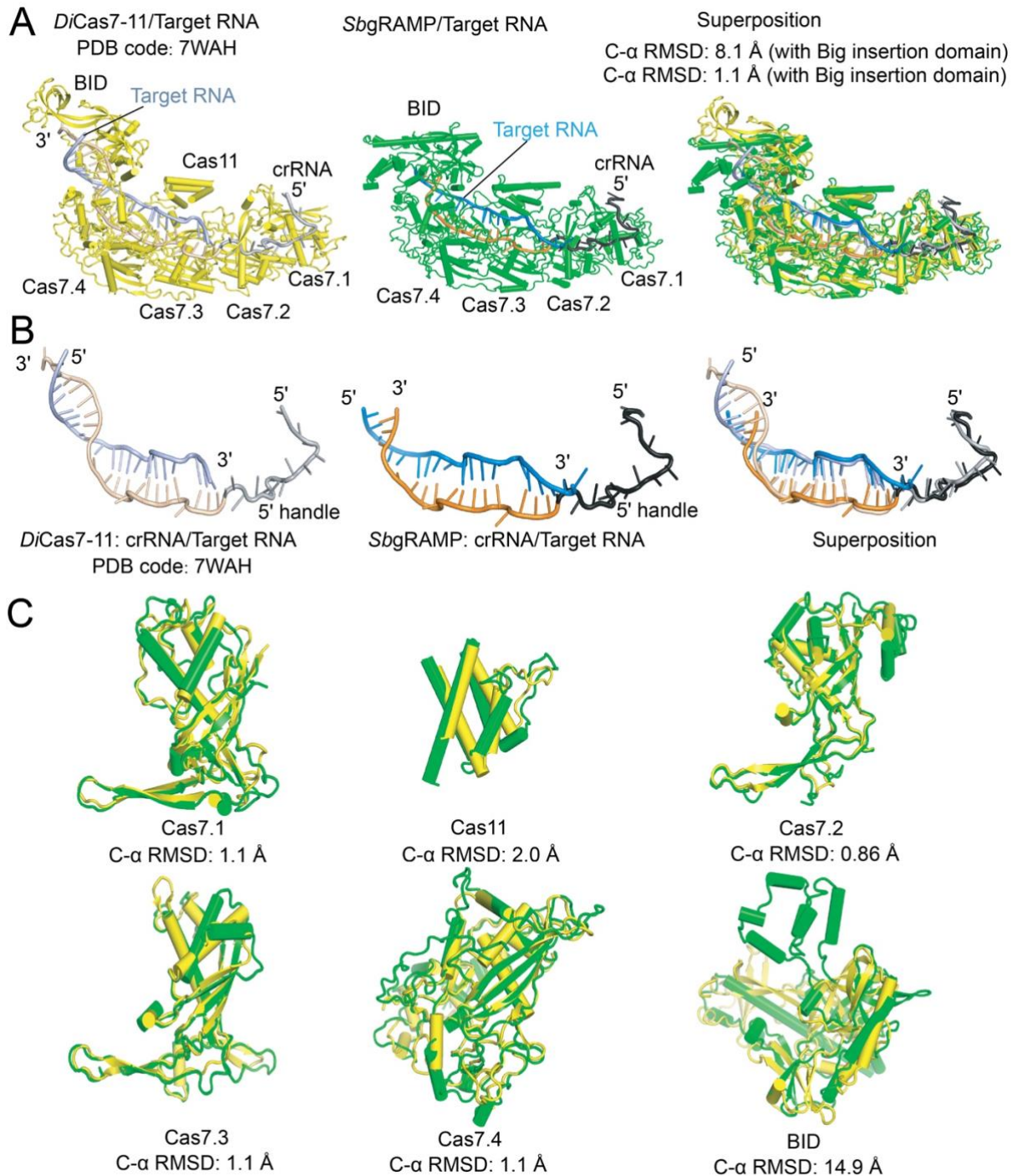


Fig. S5. Structural comparison between *Sb-gRAMP* and *Di-Cas7-11*, both in the target RNA bound state. (A) Side-by-side and superpositioning of *Sb-gRAMP* and *Di-Cas7-11* (PDB: 7WAH). The structure and orientation of the big insertion domain are significantly different in the two structures. The rest of the two structures agree quite well. Alignment of all non-BID C α atoms produced an r.m.s.d. of only 1.1 Å. **(B)** Guide and target RNAs also align well when the two structures are aligned along non-BID C α atoms. **(C)** Individual domains aligned along C α atoms superimpose very well, except BID. The BID cryo-EM density in our reconstruction did not allow reliable de novo model building. An AlphaFold predicted model was docked instead.

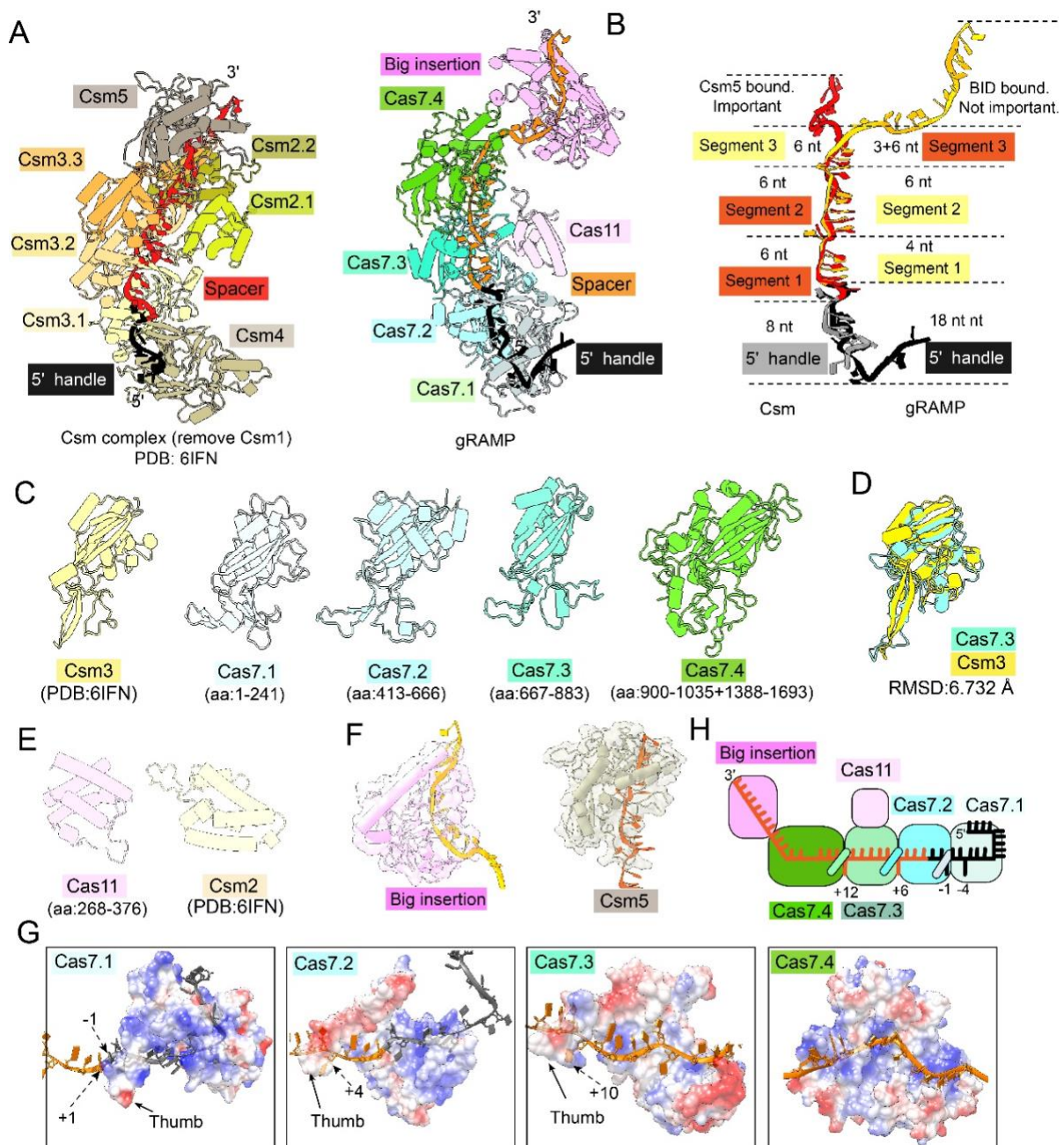


Fig. S6. Structural comparison between type III-E *Sb*-gRAMP and type III-A Csm complex. (A) Side-by-side comparison between type III-E *Sb*-gRAMP and type III-A Csm (10) (PDB: 6IFN) structures. **(B)** Structural alignment and comparison of crRNAs from *Sb*-gRAMP and Csm. **(C)** Side-by-side comparison of Csm-Cas7 and four Cas7 domains in *Sb*-gRAMP. **(D)** Structural alignment showing that Cas7.3 has the highest structure conservation with Csm3. **(E)** Side by side comparison between *Sb*-gRAMP Cas11 and its equivalent Csm2 in the Csm complex. **(F)** Side by side comparison between *Sb*-gRAMP BID and Csm5 in the Csm complex. **(G)** Snapshots of four Cas7 subunits bound to crRNA. Cas7.1, Cas7.2, and Cas7.3 all have an obvious thumb structure to flip out a base of crRNA. **(H)** Cartoon model showing the architecture of the *Sb*-gRAMP RNP complex.

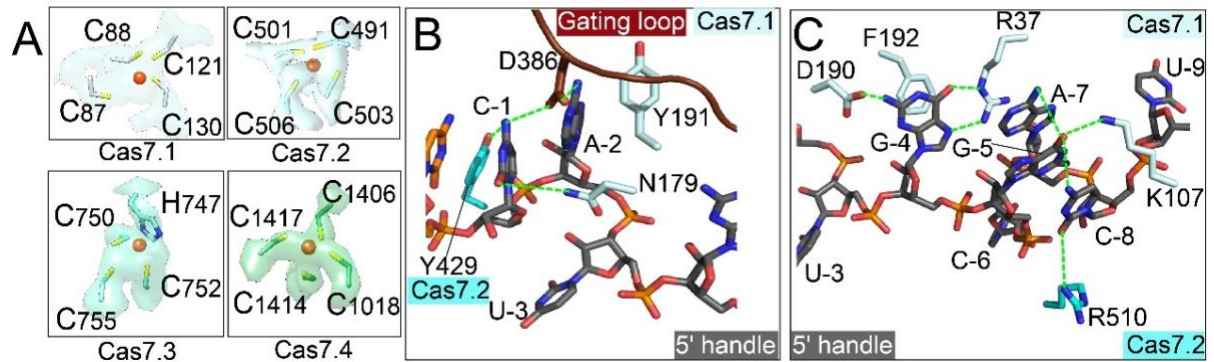


Fig. S7. Structural basis for the zinc-finger of *Sb*-gRAMP and 5' handle recognition. (A) Close-up view of the cryo-EM density of zinc-fingers from Cas7.1 to Cas7.4 subunits. (B) Close-up view of Cas7.1 and Cas7.2 contacting the -1 to -3 bases of 5' handle. (C) Close-up view of Cas7.1 and Cas7.2 contacting the -4 to -9 bases of 5' handle.

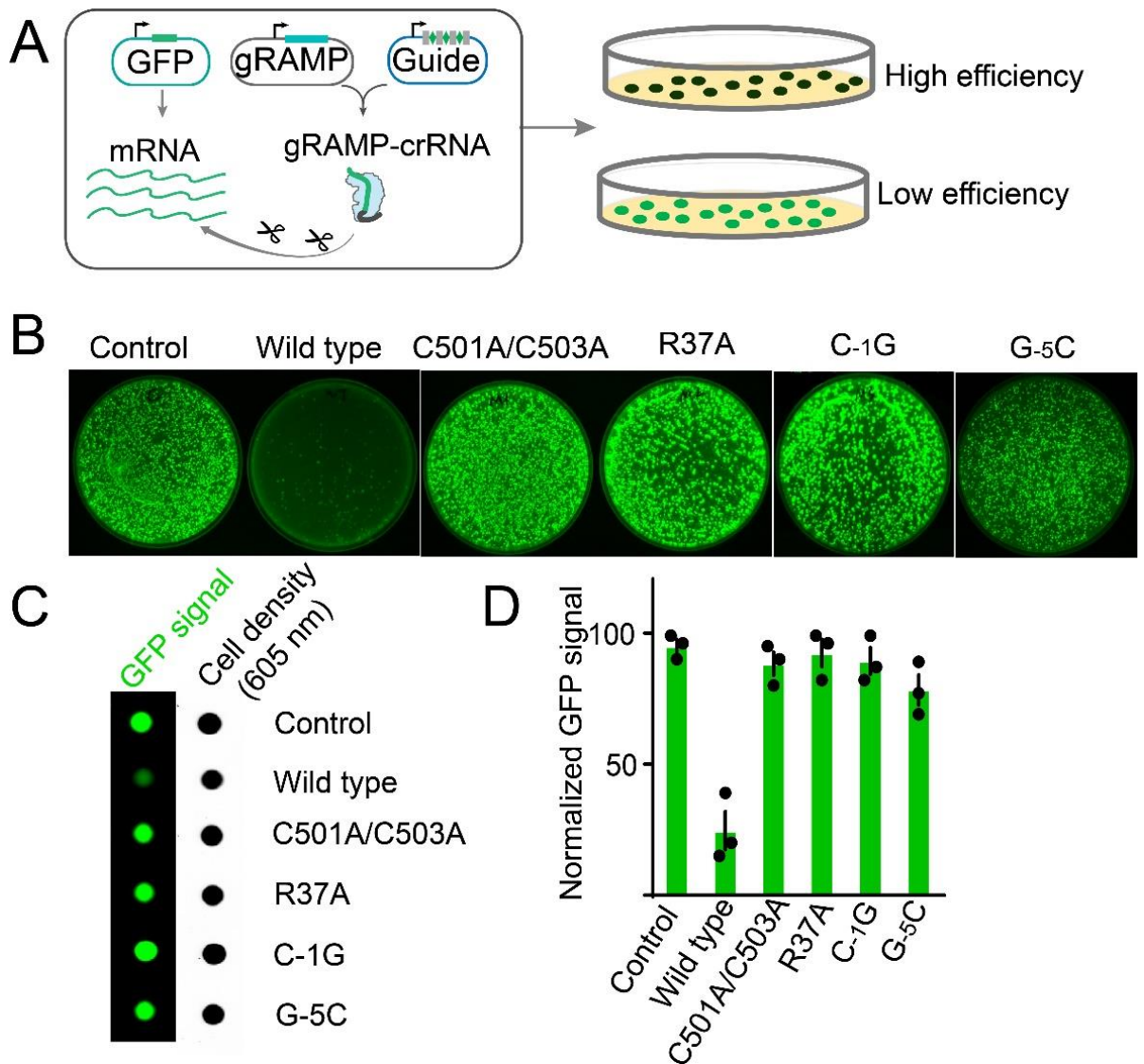


Fig. S8. Mutagenesis analysis of *Sb*-gRAMP RNP protein. (A) Model depicting the workflow of *in vivo* RNA knock down assay in *E.coli*. **(B)** Transformation plates of RNA knockdown assay from different mutations (C501A/C503A is the zinc-finger from Cas7.2; R37 from Cas7.1; C-1 and G-5 from the 5' handle region of crRNA). **(C)** Bacteria solution dot assay to show the GFP signal and cell density. **(D)** Normalized knock down efficiency from different mutagenesis.

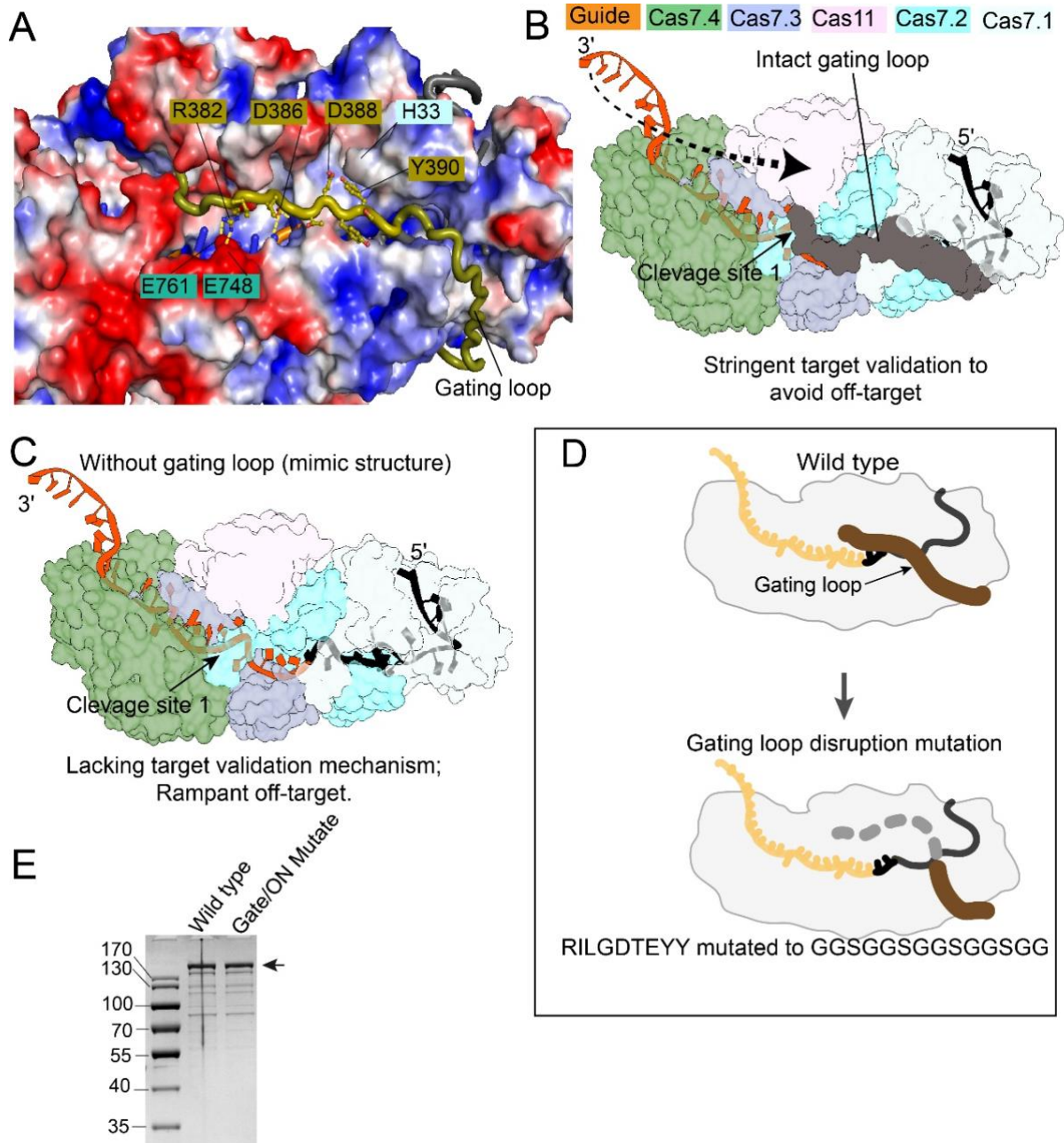


Fig. S9. Functional characterization of the gating loop. (A) close-up view of the gating loop located in a deep cavity and blocking the “seed region” of crRNA. (B) A model showing the direction of base-pairing formation between target RNA and guide RNA. Base-pairings that can only happen after gating loop displacement likely takes place at the end. (C) A model showing that without gating loop protection, base-pairing can take place stochastically. Off-targeting may be rampant. (D) Cartoon model depicting mutagenesis of the gating loop. (E) SDS-PAGE showing the quality of the wild type and gating loop mutant *Sb*-gRAMP samples.

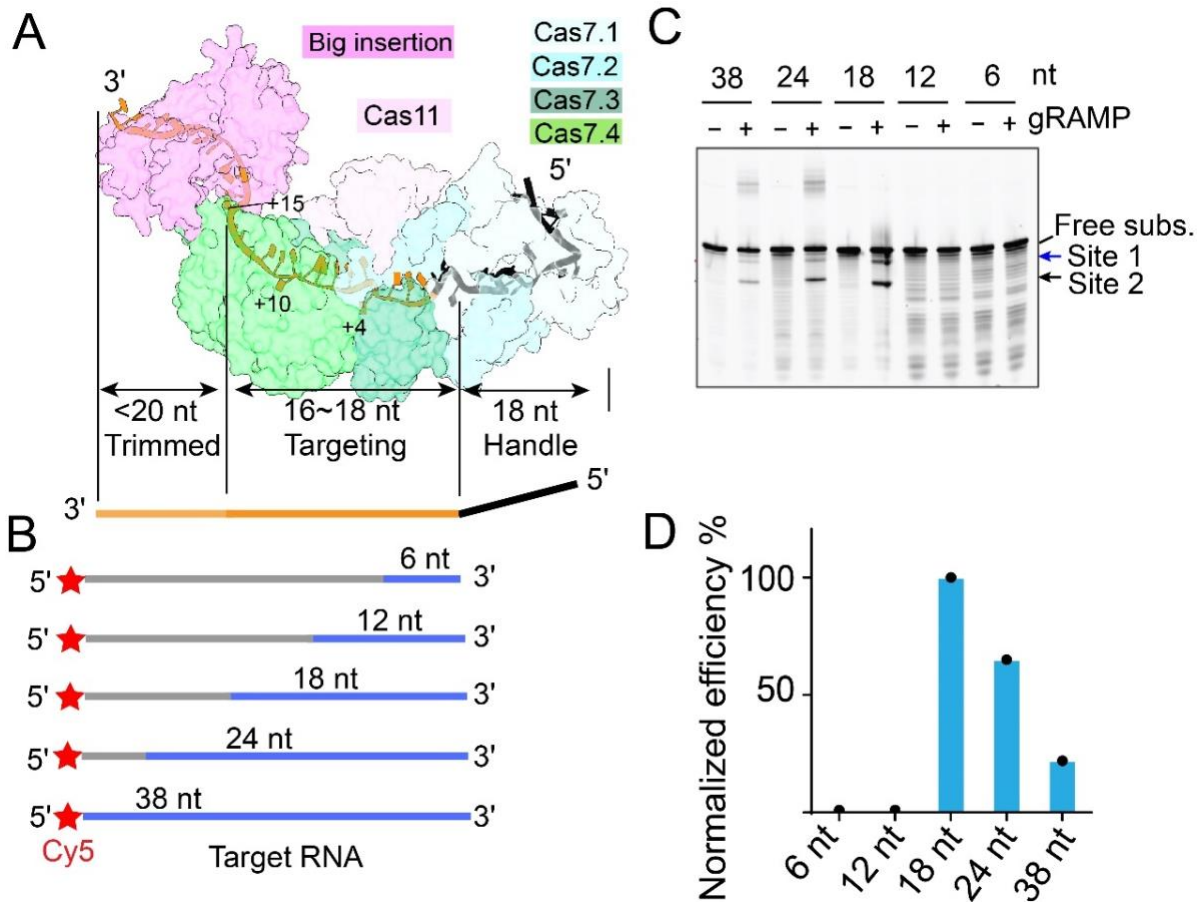


Fig. S10. RNA cleavage experiments using varying lengths of complementarity in the target RNA. (A) Cartoon model to showing the full-length *Sb*-gRAMP architecture and crRNA region. **(B)** Model of RNA substrates used in assay showing varying lengths of complementarity with crRNA. **(C)** Cleavage assay of RNA substrates. **(D)** Normalized cleavage efficiency seen in panel C.

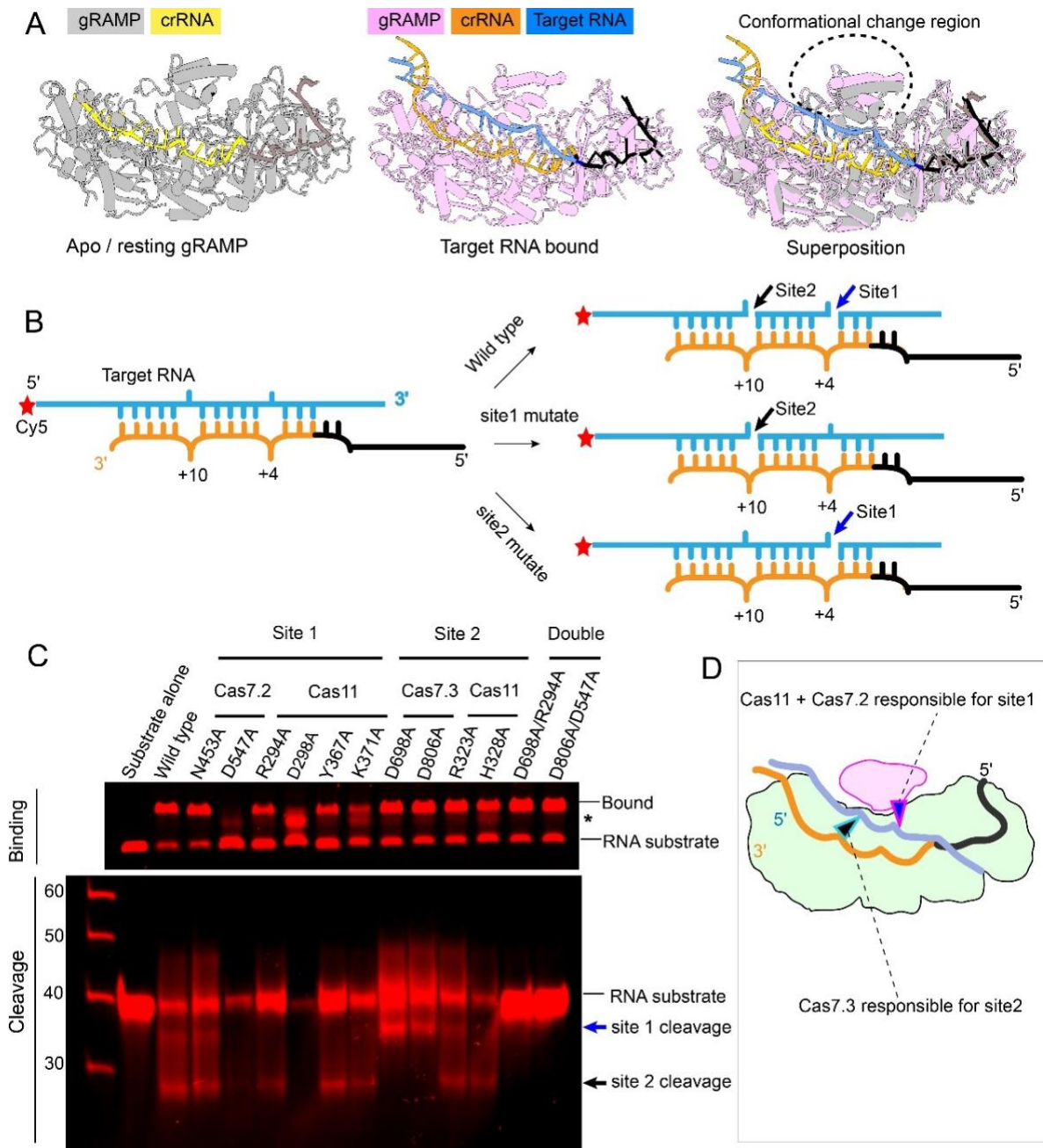


Fig. S11. Characterization of *Sb*-gRAMP RNase activity. (A) Structural alignment showing the main conformational change is in Cas11 region. **(B)** A model showing the RNA cleavage pattern in wild type, site 1, and site 2 mutations of *Sb*-gRAMP. **(C)** RNA substrate binding and cleavage assay for *Sb*-gRAMP mutations. **(D)** Cartoon model depicting the *Sb*-gRAMP domains involved in each cleavage site.

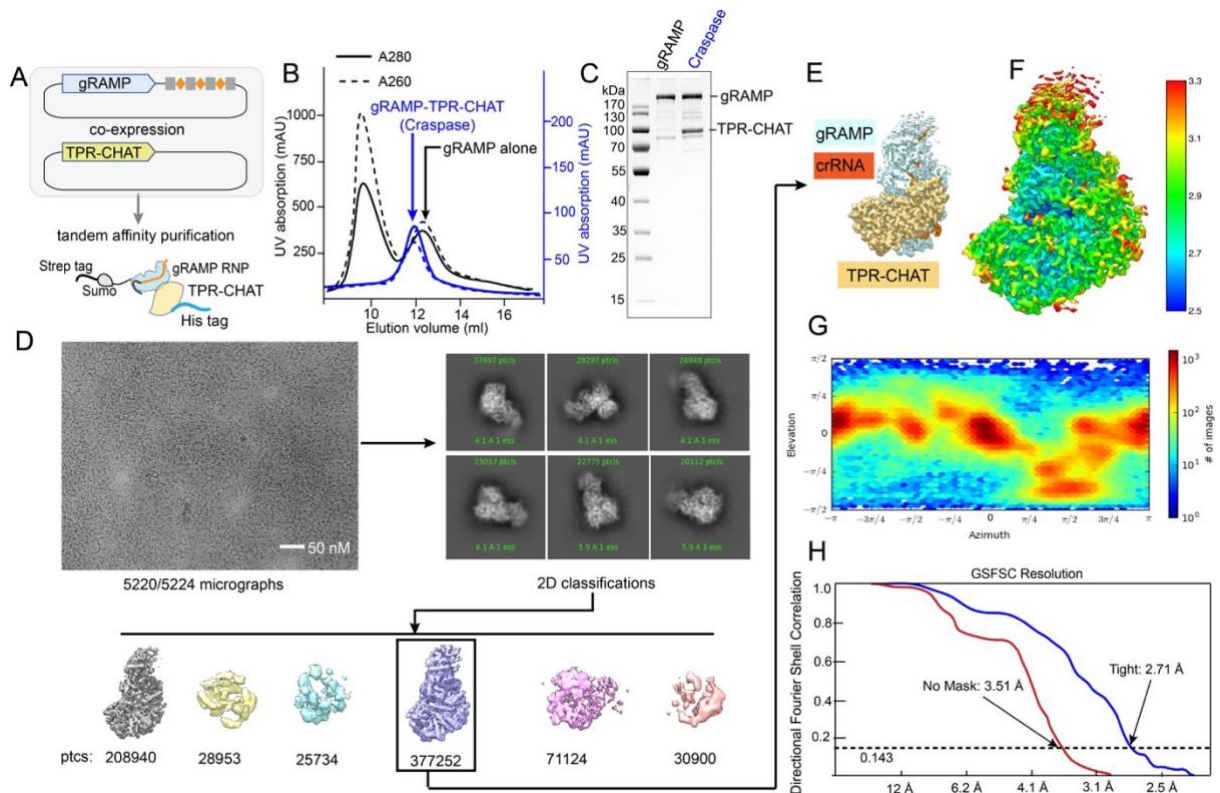


Fig. S12. Purification and Cryo-EM single particle reconstruction of *Sb*-gRAMP-TPR-CHAT complex (Craspase). (A) Model of method used for co-expression and purification for Craspase. (B) Purification profile comparison between *Sb*-gRAMP and Craspase on size-exclusion chromatography. (C) Representative SDS-PAGE comparison between *Sb*-gRAMP and Craspase. (D) Workflow of the cryo-EM image processing and (E) 3D reconstruction for Craspase. (F) Final electron density map showing local resolution for Craspase. (G) 3D Euler distribution plot revealing the representation of the single particle orientation in the final reconstruction. (H) Fourier Shell Correlations (FSC) of the *Sb*-gRAMP-Matching PFS RNA complex reconstruction, with the gold-standard cutoff (FSC = 0.143) marked with a dotted line.

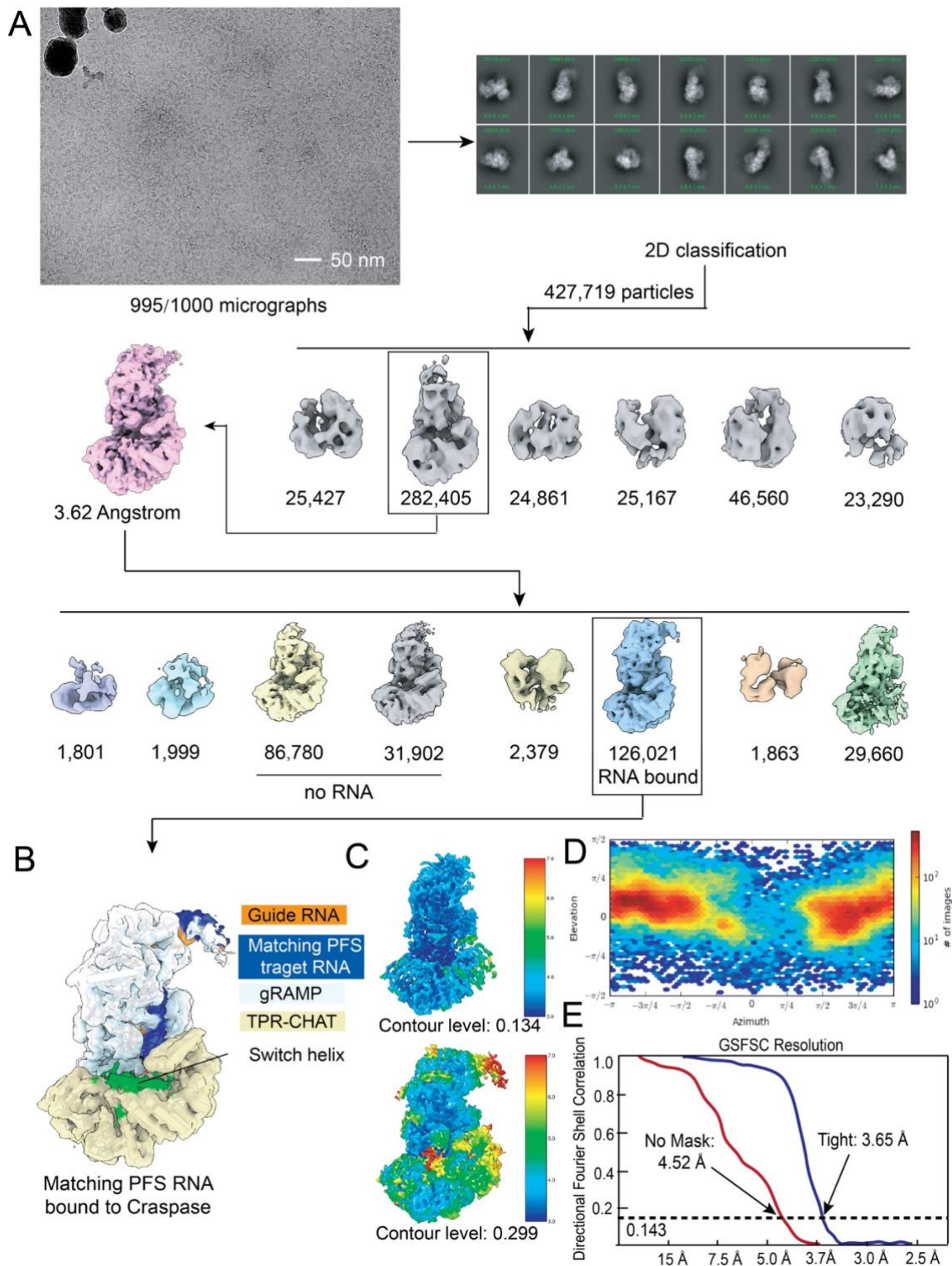


Fig. S13. Cryo-EM single particle reconstruction of Craspase bound with a matching PFS RNA target. (A) Workflow of the cryo-EM image processing and (B) 3D reconstruction for the Craspase bound with a matching PFS RNA. (C) Final electron density map showing local resolution at different contour levels. (D) 3D Euler distribution plot revealing the representation of the single particle orientation. (E) Fourier Shell Correlations defining the reconstruction resolution, with the gold-standard cutoff (0.143) marked with a dotted line.

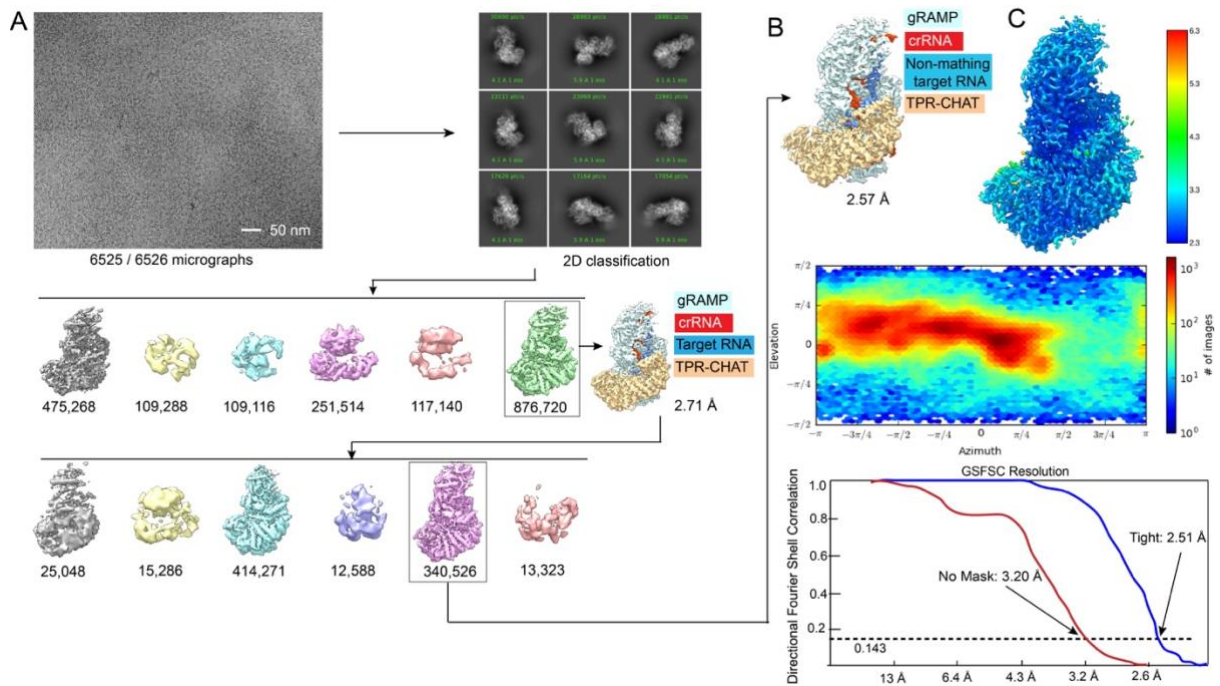


Fig. S14. Cryo-EM single particle reconstruction of Craspase bound with a non-matching PFS RNA target. (A) Workflow of the cryo-EM image processing and **(B)** 3D reconstruction for the Craspase bound with a non-matching PFS RNA. **(C)** Final electron density map showing local resolution at different contour levels. **(D)** 3D Euler distribution plot revealing the representation of the single particle orientation. **(H)** Fourier Shell Correlations defining the reconstruction resolution, with the gold-standard cutoff (0.143) marked with a dotted line.

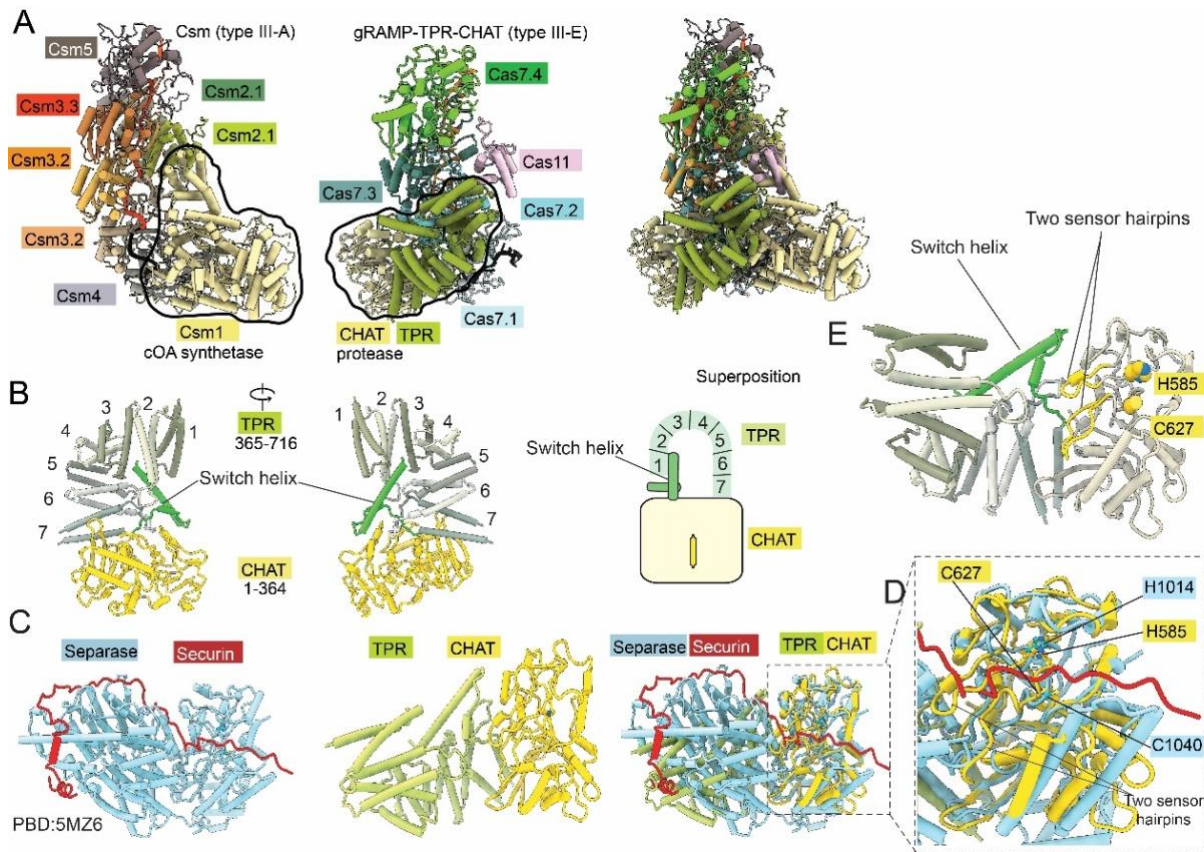


Fig. S15. Structural analysis of the TPR-CHAT component of Craspase. (A) Left: structural model of Csm complex with cOA synthetase. Middle: structural model of *Sb*-gRAMP with TPR-CHAT protease. Right: structural superposition of the Csm complex and Craspase. (B) Right and middle: overall structure of the TPR-CHAT component of Craspase. Right: Cartoon model depicting the architecture of TPR-CHAT. (C) Structural comparison between Separase-Securin complex (PDB: 5MZ6) and TPR-CHAT. Left: Separase-Securin complex structure. Middle: TPR-CHAT structure. Right: structural superposition of TPR-CHAT with Separase-Securin. (D) Close-up view of the structural alignment of protease domain from Separase and CHAT. (E) Close-up view of "switch helix" and "sensor hairpins".

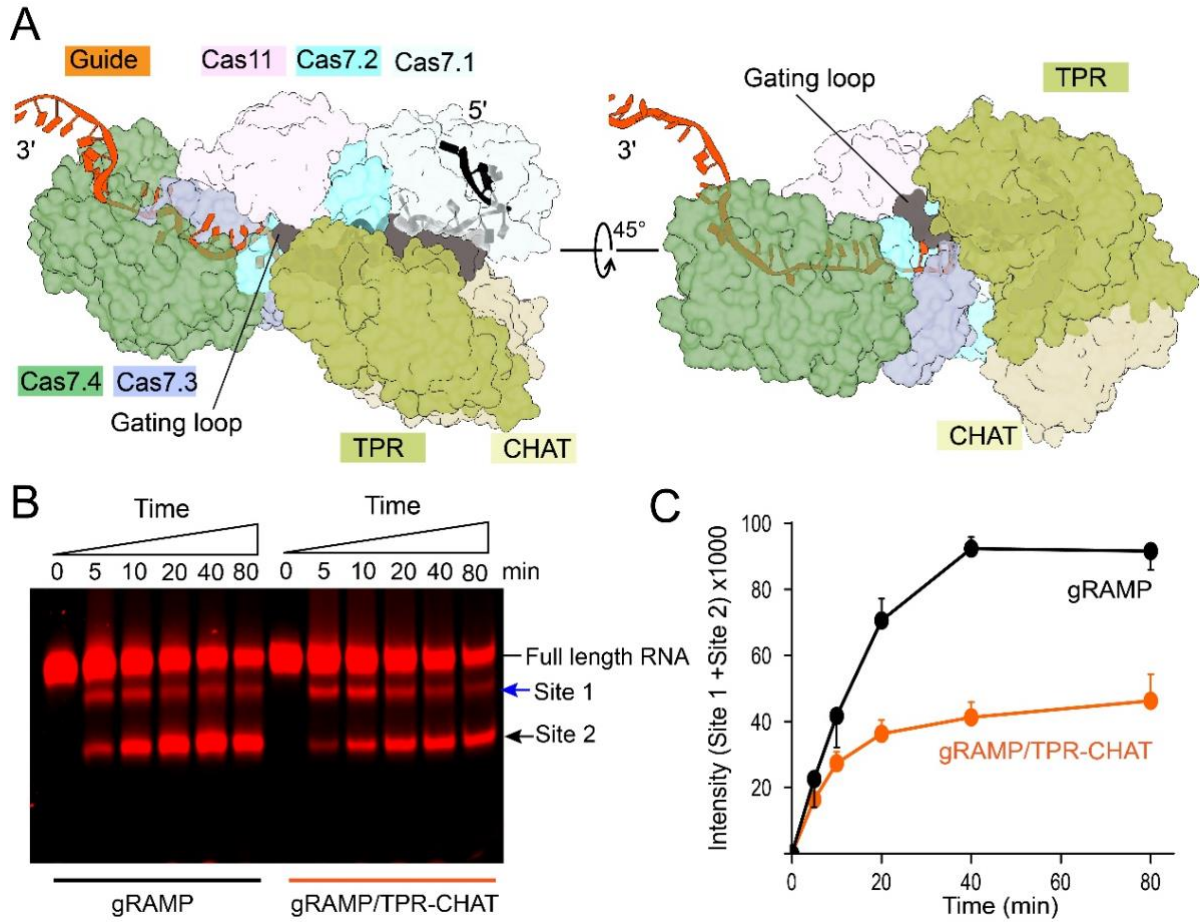


Fig. S16. Biochemistry and structure analysis of the Caspase complex. (A) Structure model revealing that TPR-CHAT binds to the gating loop and limits gating loop dynamic movement. **(B)** RNA cleavage activity comparison between *Sb*-gRAMP and Caspase. **(C)** Quantification of the cleavage products from site 1 and site 2 from panel A.

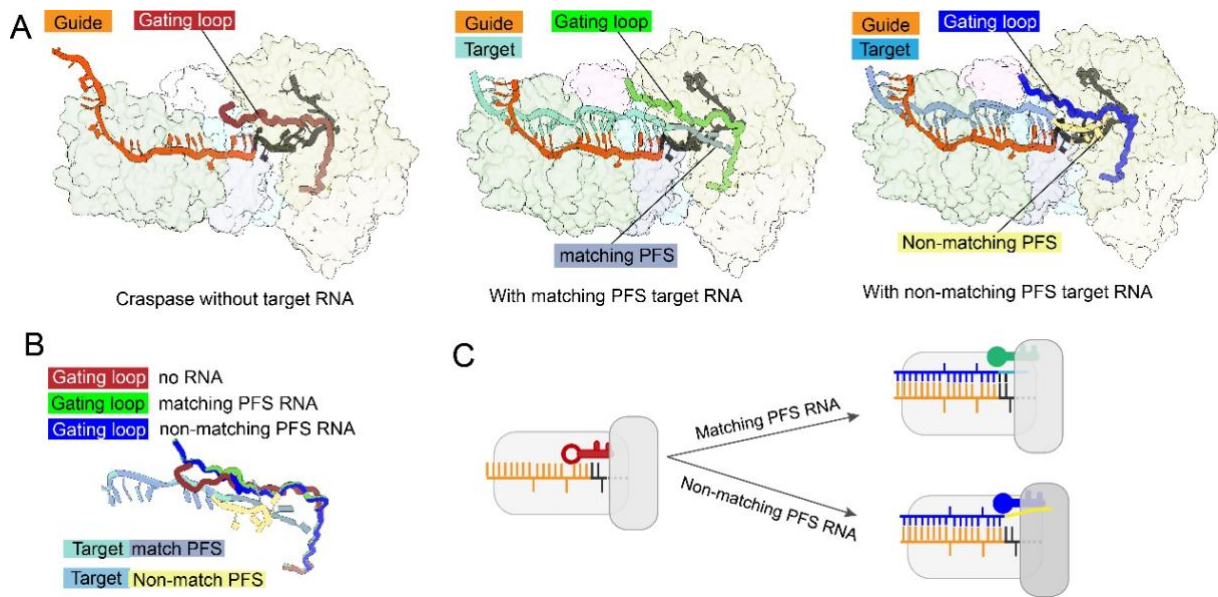


Fig. S17. The structural dynamics of the gating loop in Craspase. **(A)** Cartoon model highlighting the gating loop conformation in apo Craspase (left), matching PFS RNA bound (middle) and non-matching PFS RNA bound Craspase complex (right). **(B)** Structural alignment of the gating loop in apo, matching PFS RNA bound and non-matching PFS RNA bound state. **(C)** Model depicting the gating loop dynamics when bound to different substrates.

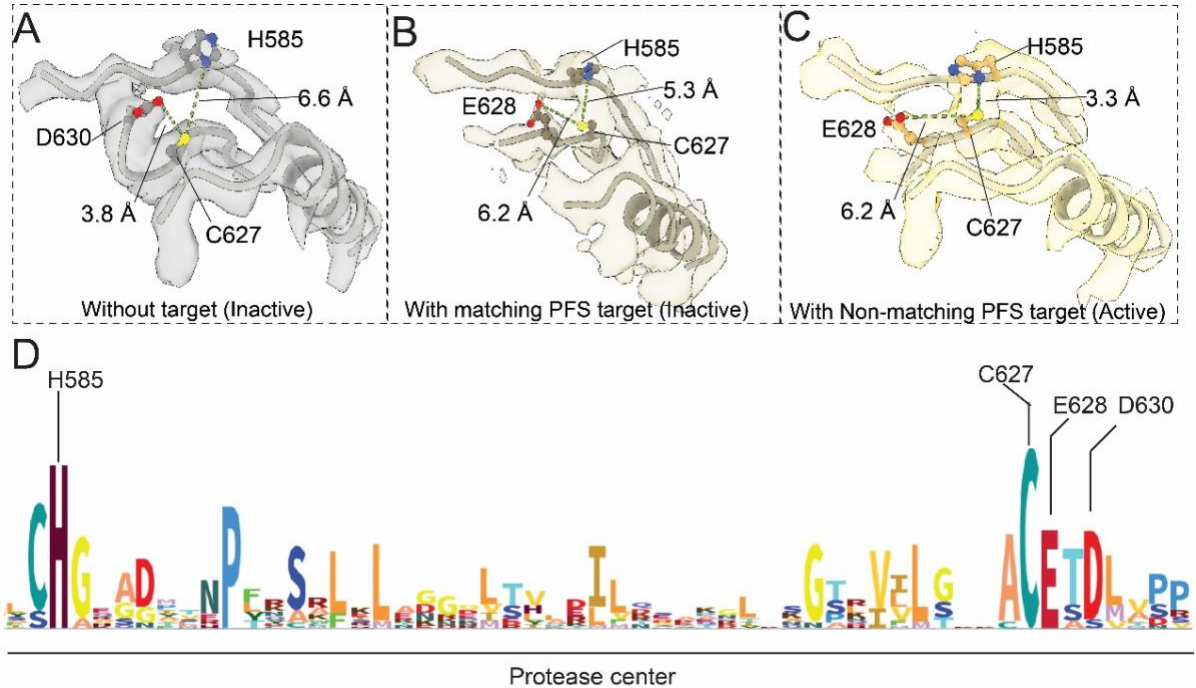


Fig. S18. CryoEM density and conservation analyses of the protease center. The extracted local density of protease center from apo state (**A**), matching PFS target RNA bound state (**B**) and non-matching PFS target bound state (**C**). Highlight the protease center residues H585, C627, E628 and D630. The catalytic dyad in the apo state and the matching PFS state are too far apart to allow general acid-base based protease activity in Craspase. (**D**) Amino sequence alignment of protease center from twenty-five TPR-CHAT homologs.

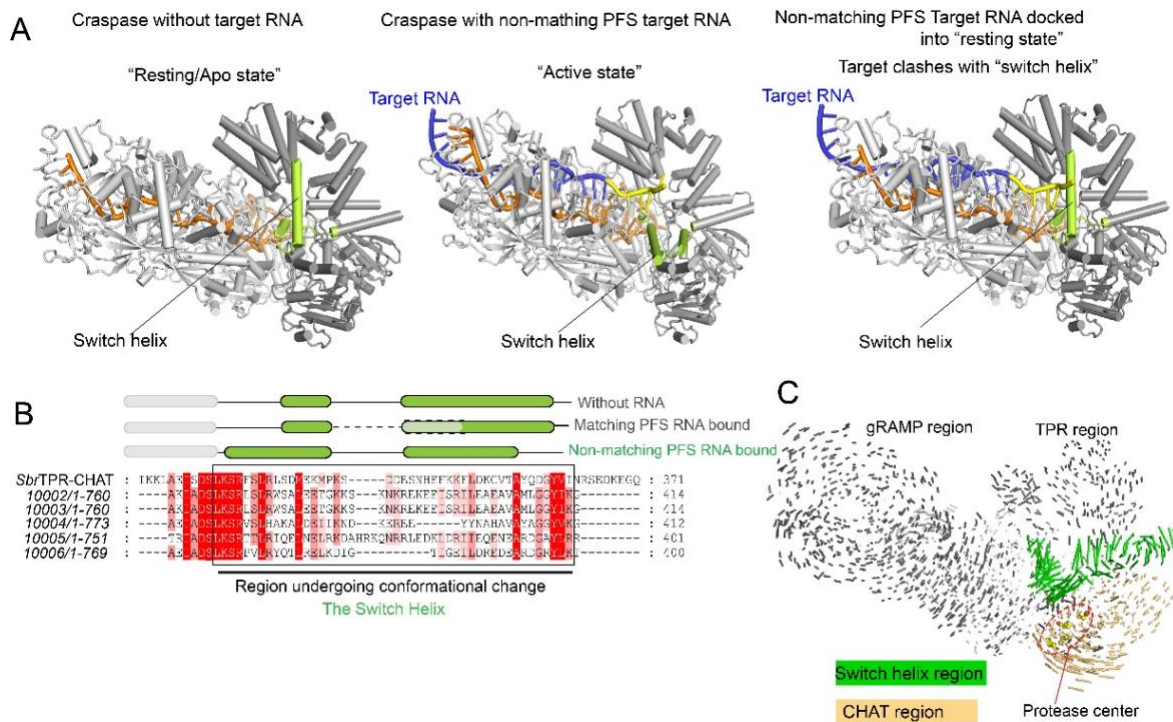


Fig. S19. The structural dynamics of the switch helix in TPR-CHAT. (A) Cartoon model highlighting the switch helix conformation in apo Craspase (left), non-matching PFS RNA bound state (middle), and their superposition (right). (B) Amino acid sequence alignment of the switch helix region in TPR-CHAT among five homologs (C) Structural comparison of Craspase/matching PFS RNA complex and Craspase/non-matching PFS RNA complex showing the large conformational change in the switch helix region and CHAT protease center region. Vector length correlates with the domain motion scale (color-coded as defined in the figure).

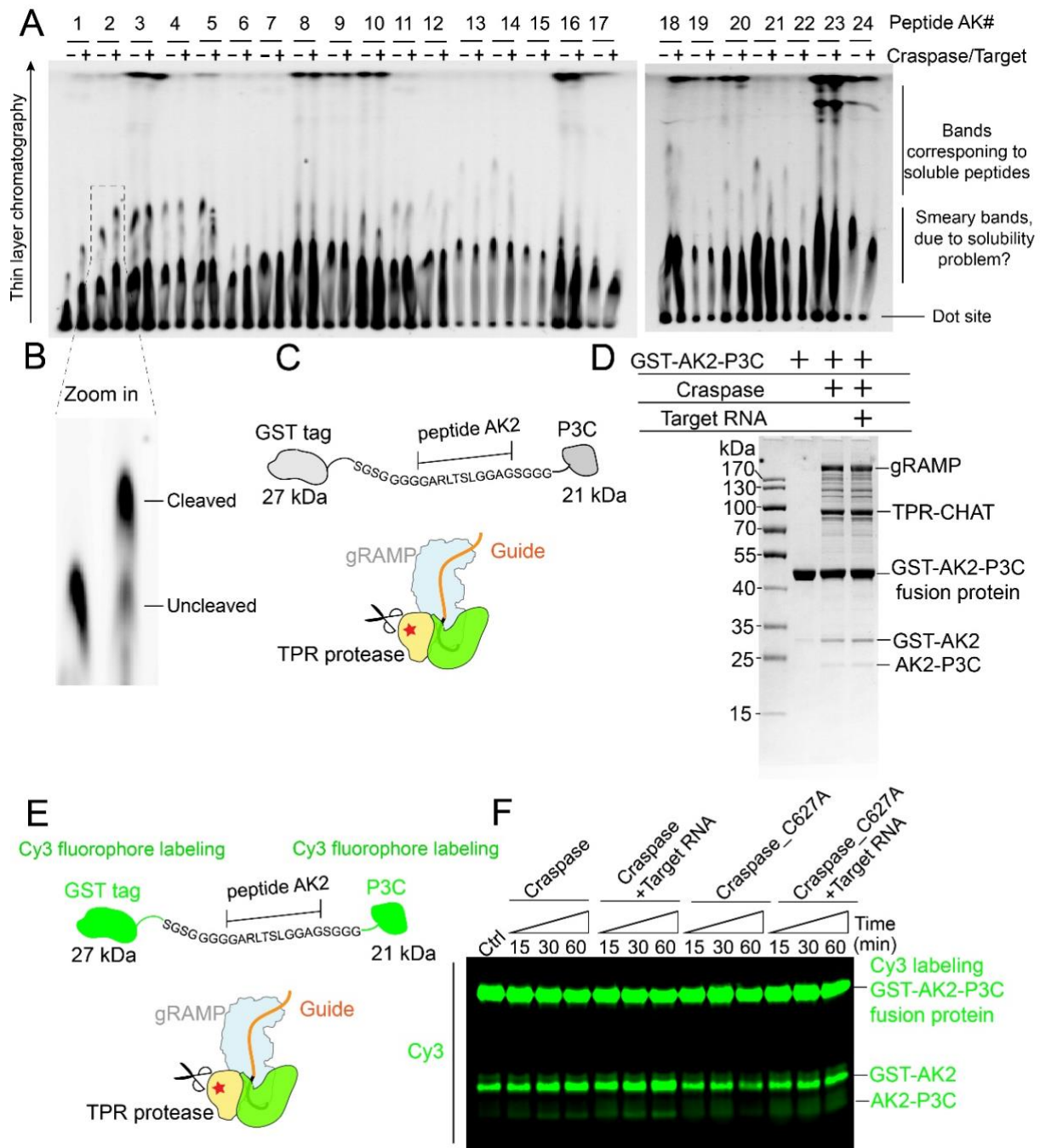


Fig. S20. The biochemical characterization of Craspase protease activity. (A) Peptide substrate screening cleavage assay and separated on thin layer chromatography (TLC). TLC results indicate substrates AK1 and AK2 are candidates for Craspase. **(B)** Zoomed in view of substrate AK2 TLC results. **(C)** Cartoon model showing AK2 linked GST-P3C fusion protein and cleavage assay with Craspase. **(D)** SDS-PAGE of Craspase cleavage assay using AK2 linked GST-P3C fusion protein. **(E)** Cartoon model showing Cy3 labeled AK2 linked GST-P3C fusion protein and Craspase cleavage assay. **(F)** Time course to track the cleavage activity by Cy3 labeled AK2 linked GST-P3C fusion protein with Craspase.

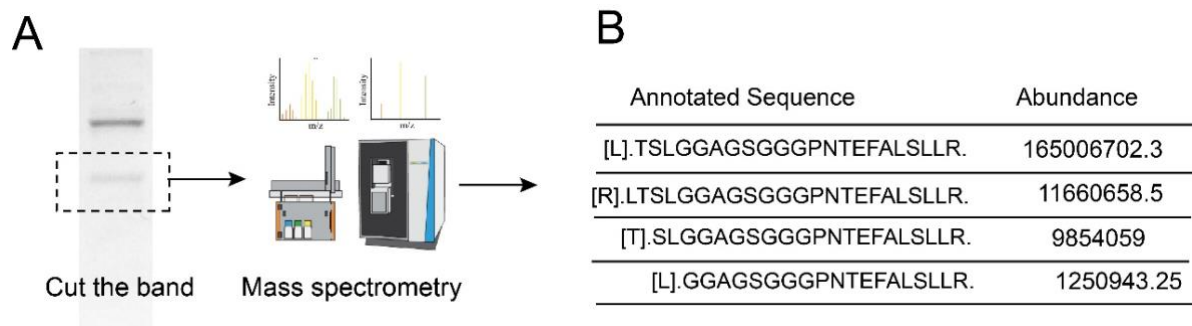


Fig. S21. Biochemical validation of Craspase protease activity. (A) Workflow of the mass spectrometry analysis of the cleavage product. **(B)** Mass spectrometry results for the cleaved peptides.

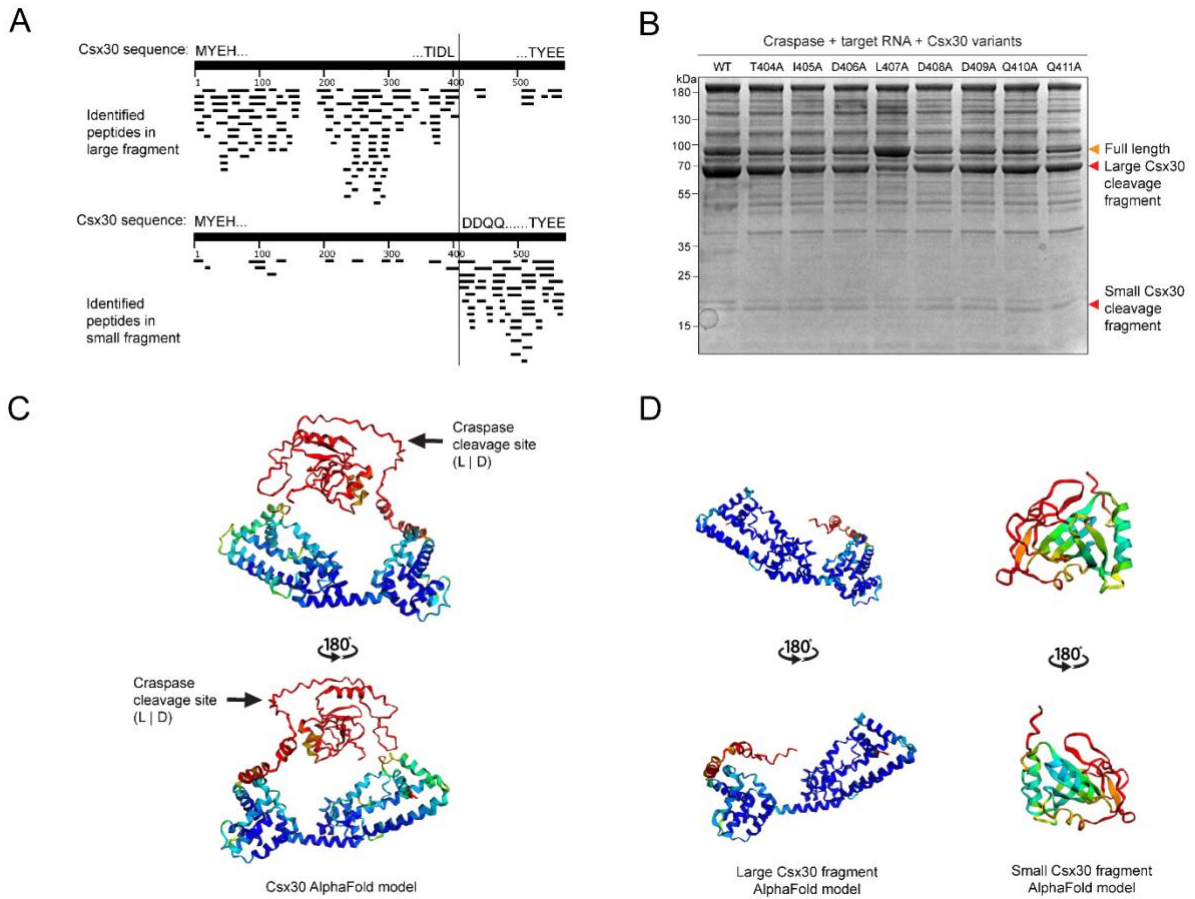


Fig S22. Csx30 processing analysis. (A) Peptides obtained from mass spectrometry of the small and large Csx30 fragment using fully non-specific cleaved variants of the Csx30 protein (listed in Table S3 and Table S4), mapped onto Csx30 using BLAST (36) to reveal a cleavage region (TIDL | DDQQ). (B) Protein gel after Craspase incubation with target RNA and Csx30 containing alanine mutations of the residues in the cleavage region. (C) AlphaFold model of Csx30 with the Craspase cleavage site indicated. The model is colored on pLDDT confidence (dark blue: very high confidence, pLDDT>90; light blue: confident, 90>pLDDT>70; yellow: low confidence, 70>pLDDT>50; orange: very low confidence, pLDDT<50). (D) AlphaFold models of the Csx30 fragments after processing by Craspase (dark blue: very high confidence, pLDDT>90; light blue: confident, 90>pLDDT>70; yellow: low confidence, 70>pLDDT>50; orange: very low confidence, pLDDT<50).

Table S1. Cryo-EM data collection, refinement, and validation statistics

Name	<i>Sb</i> -gRAMP alone	<i>Sb</i> -gRAMP- Non match PFS target RNA	<i>Sb</i> -gRAMP- Match PFS target	<i>Sb</i> -gRAMP- Non match PFS target with MgCl ₂	<i>Sb</i> -gRAMP- TPR-CHAT	<i>Sb</i> -gRAMP- TPR-CHAT- Non match PFS target	<i>Sb</i> -gRAMP-TPR- CHAT-match PFS target
PDB ID	8D97	8D8N	8D9E	8D9I	8D9F	8D9G	8D9H
EMDB ID	27257	27252	27259	27263	27260	27261	27262
Data collection and Processing							
Microscope	Arctica	Arctica	Arctica	Arctica	Krios	Krios	Arctica
Voltage (keV)	200	200	200	200	300	300	200
Camera	K3	K3	K3	K3	K3	K3	K3
Magnification	81,000	81,000	81,000	81,000	81,000	81,000	81,000
Pixel size (Å/pixel)	1.21Å	1.21Å	1.28Å	1.28Å	1.07Å	1.07Å	1.21Å
Total electron exposure (e ⁻ /Å ²)	59	59	50	50	50	50	50
Exposure rate (e ⁻ /pixel/sec)	19.67	19.67	18.7	19.2	20.1	18.87	21.3
Number of frames	50	50	50	50	50	50	50
Defocus range (µm)	1.0 – 2.5	1.0 – 2.5	0.8 – 2.5	1.0 – 2.5	1.0 – 2.5	1.0 – 2.5	1.0-2.5
Automation software	EPU	EPU	EPU	EPU	EPU	EPU	EPU
Tilt angle	N/A	N/A	N/A	N/A	N/A	N/A	N/A
Energy filter slit width	N/A	N/A	N/A	N/A	N/A	N/A	N/A
Micrographs collected	1214	1214	784	601	5224	6526	1000
Micrographs used	1208	1208	723	597	5220	6526	995
Total extracted particles	1,611,555	1,611,555	1,176,000	997,652	6,268,800	8,046,558	1,062,986
<u>For each reconstruction:</u>							
Refined particles (no.)	309,335	309,335	181,985	154,402	742,903	886,430	427,710
Final particles (no.)	21,741	89,342	46,269	79785	377,252	340,526	126,021
symmetry parameters	C1	C1	C1	C1	C1	C1	C1
Estimated error of translations/rotations	N/A	N/A	N/A	N/A	N/A	N/A	N/A
Resolution (global, Å)							
FSC 0.5 (unmasked/masked)	5.1/4.2	4.8/4.0	4.7/3.9	4.6/3.9	3.4/3.0	3.5/3.0	4.5/3.9
FSC 0.143 (unmasked/masked)	4.6/3.7	4.2/3.6	4.2/3.7	4.0/3.6	3.0/2.7	3.0/2.5	4.2/3.6
Resolution range (local, Å)	3.0 – 10	3.0 – 10	3.0 – 10	3.0 – 10	2.0 – 10	2.0 – 10	3.0-10
Resolution range due to anisotropy (Å)	N/A	N/A	N/A	N/A	N/A	N/A	N/A
Map sharpening <i>B</i> factor (Å ²)	-50	-50	-78	-70	-100	-100	-70
Map sharpening methods	Global	Global	Global	Global	Global	Global	Global

Model composition (for each model)

Protein	1600	1256	1256	1256	1912	1965	1936
Ligands	4	4	4	4	4	4	7
RNA/DNA	42	56	57	59	33	59	56

Model Refinement (for each model)

Refinement package	Phenix	Phenix	Phenix	Phenix	Phenix	Phenix	Phenix
- real or reciprocal space	Real	Real	Real	Real	Real	Real	Real
- resolution cutoff	3.6	3.6	3.6	3.6	2.8	2.7	3.6
Model-Map scores							
-CC	0.7	0.6	0.7	0.7	0.8	0.8	0.9
<i>B</i> factors (Å ²)	68.21	84.78	84.71	88.64	149.56	116.07	123.63
Protein residues	58.37	83.20	83.11	83.20	149.90	116.11	126.99
Ligands	133.5	155.3	176.19	171.20	177.56	149.81	55.22
RNA/DNA	212.12	97.75	96.92	133.22	141.65	115.33	80.64
R.m.s. deviations from ideal values							
Bond lengths (Å)	0.008	0.005	0.005	0.005	0.007	0.009	0.014
Bond angles (°)	1.2	0.987	0.987	1.012	0.672	1.038	1.403

Validation (for each model)

MolProbity score	2.08	1.94	1.93	2.07	1.71	1.90	2.26
CaBLAM outliers	0.2	0.0	0.0	0.0	0.0	0.0	0.2
Clashscore	17.8	8.95	9.07	12.46	9.16	11.8	18.04
Poor rotamers (%)	0.4	0.2	0.2	0.2	0.1	0.2	0.89
C-beta deviations	0.2	0.0	0.0	0.0	0.0	0.1	0.0
EMRinger score	2.067	1.34	2.08	2.21	3.25	2.23	1.30
Ramachandran plot							
Favored (%)	95.32	92.68	92.68	92.88	96.56	95.30	94.00
Outliers (%)	0.5	0.2	0.2	0.2	0.1	0.2	0.89

Table S2. Mass spectrometry results of two in-gel digestion samples of the large and small Csx30 cleavage fragments.

Protein	-10 log P	Area Sample	Number of unique peptide per protein	Csx30 cleavage fragment
Csx30	388.80	2.07E10	71	Large
sp P0CE47 EFTU1_ECOLI	251.48	2.23E8	22	Large
sp P0CE48 EFTU2_ECOLI	251.48	2.23E8	22	Large
sp P0ABB4 ATPB_ECOLI	237.83	1.11E8	27	Large
sp P0A6P9 ENO_ECOLI	207.99	1.95E7	16	Large
sp P02943 LAMB_ECOLI	189.66	3.24E7	13	Large
sp P0A6J5 DADA_ECOLI	189.65	2.7E7	14	Large
sp P0ABC7 HFLK_ECOLI	185.24	1.95E7	11	Large
sp P0ABH7 CISY_ECOLI	182.45	1.73E7	12	Large
sp P00393 NDH_ECOLI	180.97	3.01E7	16	Large
sp P0A6H5 HSLU_ECOLI	176.74	5.95E7	18	Large
sp P75990 BLUF_ECOLI	169.51	1.64E7	14	Large
sp P0AG30 RHO_ECOLI	157.13	1,00E+07	13	Large
sp P0A6Y8 DNAK_ECOLI	155.13	7.01E6	11	Large
sp P0A855 TOLB_ECOLI	152.39	1.46E7	8	Large
sp P08622 DNAJ_ECOLI	152.08	8.71E6	10	Large
sp P08200 IDH_ECOLI	149.68	1.05E7	10	Large
sp P0A6B7 ISCS_ECOLI	149.11	2.19E7	12	Large
sp P0AE06 ACRA_ECOLI	146.47	3.01E7	13	Large
sp P24554 RADA_ECOLI	145.65	8.17E6	11	Large
sp P27434 RODZ_ECOLI	143.94	9.29E6	8	Large
sp P31979 NUOF_ECOLI	142.45	1.67E7	11	Large
sp P68187 MALK_ECOLI	138.47	4.39E6	6	Large
sp P0AFG6 ODO2_ECOLI	135.44	1.71E7	10	Large
sp P75876 RLMI_ECOLI	131.00	2.15E6	6	Large
sp P03004 DNAA_ECOLI	130.73	9.2E6	10	Large
sp P10441 LPXB_ECOLI	126.09	3.69E6	4	Large
sp P0C8J8 GATZ_ECOLI	124.37	6.06E6	6	Large
sp P0A836 SUCC_ECOLI	123.96	2.54E6	7	Large
sp P30871 3PASE_ECOLI	117.03	3.05E6	7	Large
sp P0A749 MURA_ECOLI	115.37	2.73E6	6	Large
sp P0A6H1 CLPX_ECOLI	110.20	4.32E6	6	Large
sp P0A847 TGT_ECOLI	108.02	2.18E6	5	Large
sp P00370 DHE4_ECOLI	106.19	2.37E6	7	Large
sp P00350 6PGD_ECOLI	104.18	2.38E6	6	Large
sp P10384 FADL_ECOLI	103.92	1.05E6	3	Large
sp P02930 TOLC_ECOLI	103.41	3.3E6	8	Large
sp P0A7D4 PURA_ECOLI	103.24	2.27E6	4	Large
sp P69786 PTGCB_ECOLI	102.36	2.44E6	5	Large
sp P76373 UDG_ECOLI	100.77	1.32E6	5	Large
sp P37095 PEPB_ECOLI	98.71	3.2E6	5	Large

sp P31120 GLMM_ECOLI	96.42	2.03E6	5	Large
sp P46130 YBHC_ECOLI	93.90	4.03E6	6	Large
sp P0A6F5 CH60_ECOLI	87.89	1.03E6	4	Large
sp P0AE45 PAEA_ECOLI	84.21	1.37E6	5	Large
sp P77552 YDHQ_ECOLI	84.15	3.45E6	4	Large
sp P36929 RSMB_ECOLI	83.81	1.46E6	3	Large
sp P0A879 TRPB_ECOLI	83.29	1.57E6	3	Large
sp P0AAI5 FABF_ECOLI	81.77	1.05E6	4	Large
sp P0A953 FABB_ECOLI	80.52	2.29E6	3	Large
sp P0A9J0 RNG_ECOLI	78.12	5.99E5	4	Large
sp P39396 BTST_ECOLI	77.36	1.54E6	3	Large
sp P27303 EMRA_ECOLI	76.14	1.13E6	4	Large
sp P36979 RLMN_ECOLI	73.77	8.88E5	2	Large
sp P0ABH0 FTSA_ECOLI	71.90	1.62E6	3	Large
sp P0AG67 RS1_ECOLI	71.87	6.57E5	4	Large
sp P42641 OBG_ECOLI	67.78	9.44E5	3	Large
sp P76503 FADI_ECOLI	67.78	1.18E6	3	Large
sp P0A850 TIG_ECOLI	66.93	1.3E6	2	Large
sp P02931 OMPF_ECOLI	66.89	7.75E5	3	Large
sp P16095 SDHL_ECOLI	66.70	1.59E6	3	Large
sp P0ABZ6 SURA_ECOLI	62.39	9.9E5	4	Large
sp P30744 SDHM_ECOLI	62.22	1.34E6	3	Large
sp P09127 HEMX_ECOLI	61.06	1.07E6	2	Large
sp P36672 PTTBC_ECOLI	59.36	1.76E6	3	Large
sp P42596 RLMG_ECOLI	59.18	1.29E6	4	Large
sp P0A7V3 RS3_ECOLI	55.56	4.4E5	2	Large
sp P60422 RL2_ECOLI	54.39	1.09E6	3	Large
sp P06149 DLD_ECOLI	51.21	8.05E5	3	Large
sp P0AGJ9 SY_Y_ECOLI	47.57	6.55E5	2	Large
sp P0AEH1 RSEP_ECOLI	47.15	3.89E5	2	Large
sp P77211 CUSC_ECOLI	45.84	4.17E5	2	Large
sp P23930 LNT_ECOLI	45.29	5.37E5	2	Large
sp P76422 THID_ECOLI	43.93	3.36E5	2	Large
sp P06715 GSHR_ECOLI	38.08	4.32E5	2	Large
Csx30	393.50	6.03E9	49	Small
sp P0A7W1 RS5_ECOLI	190.95	7.23E7	10	Small
sp P02359 RS7_ECOLI	187.74	5.76E7	11	Small
sp P0ADY7 RL16_ECOLI	176.62	2.67E7	4	Small
sp P0AA10 RL13_ECOLI	147.43	8.33E7	10	Small
sp P0A7J3 RL10_ECOLI	133.86	4.7E7	7	Small
sp P0A7R1 RL9_ECOLI	120.73	4.34E6	7	Small
sp P02413 RL15_ECOLI	115.54	1.44E7	6	Small
sp P0ACJ0 LRP_ECOLI	106.74	2.38E6	5	Small
sp P0ABA0 ATPF_ECOLI	102.89	2.57E6	6	Small
sp P0A7L3 RL20_ECOLI	101.89	8.4E6	5	Small
sp P0ABD8 BCCP_ECOLI	98.98	1.41E7	3	Small

sp P0AG44 RL17_ECOLI	90.27	6.13E6	3	Small
sp P02358 RS6_ECOLI	88.27	1.27E6	3	Small
sp P64596 YRAP_ECOLI	87.11	1.11E6	2	Small
sp P0ABV6 TOLR_ECOLI	86.15	2.46E6	4	Small
sp P0AEE1 DCRB_ECOLI	77.89	1.23E6	3	Small
sp P0A912 PAL_ECOLI	72.74	3.47E6	3	Small
sp P0A7X3 RS9_ECOLI	69.43	4.00E+05	3	Small
sp P0AG27 YIBN_ECOLI	61.57	1.22E6	2	Small
sp P0A7J7 RL11_ECOLI	59.57	5.18E5	2	Small
sp P0A7S3 RS12_ECOLI	57.61	4.76E5	2	Small
sp P00894 ILVH_ECOLI	54.81	4.49E5	2	Small

Table S3. Peptides obtained from mass spectrometry of the small Csx30 fragment using fully non-specific cleaved variants of the Csx30 protein.

Peptides	-10 log P	Mass	Length	Processed with
LDREESISIMPDPDNIR	65.63	19.989.680	17	Trypsin
IAEEVRDYTKPLNVVLIK	62.99	24.394.099	21	Trypsin
FIDKVEDWYWGGTCFAEDKKNLVFPLK	62.61	34.186.694	28	Trypsin
FIDKVEDWYWGGTCFAEDKK	59.74	24.931.311	20	Trypsin
FIDKVEDWYWGGTCFAEDK	57.86	23.650.361	19	Trypsin
FAVIGLSNNSDLEIFVNK	55.88	21.080.789	19	Trypsin
DYTKPLNVVLIK	55.63	17.420.342	15	Trypsin
PIKQNPVGITLR	52.86	13.348.033	12	Trypsin
KANEIDTESFNAHLETLR	52.20	22.001.123	19	Trypsin
AGAEFCTFDKINYLMSVHYLICIR	46.37	30.494.500	25	Trypsin
TITYPLLGEIEGSK	44.56	15.198.134	14	Trypsin
EESISIMPDPDNIR	44.35	16.147.559	14	Trypsin
ASTQKEQIPIK	42.58	12.416.979	11	Trypsin
SEDYKELWK	40.13	11.965.713	9	Trypsin
EDYKELWK	39.87	11.095.393	8	Trypsin
TYPVDASGSR	39.47	10.514.934	10	Trypsin
ITLWIEEGDFSPLR	39.20	16.748.617	14	Trypsin
FIDKVEDWYWGGTCF	38.36	19.218.345	15	Trypsin
INYLMSVHYLICIR	37.31	19.229.746	15	Trypsin
PVDASGSR	37.13	7.873.824	8	Trypsin
FLNAFCGPGMDDR	37.08	14.986.333	13	Trypsin
TITYPLLGEIEGSKGYR	36.64	18.959.993	17	Trypsin
KNNLVFPLK	35.07	10.716.440	9	Trypsin
QNPVGITLR	34.64	9.965.716	9	Trypsin
VEEEIKEVDISK	34.63	14.167.347	12	Trypsin
ASEDYKELWK	34.27	12.676.084	10	Trypsin
SISIMPDPDNIR	33.56	13.566.708	12	Trypsin
GTCFAEDKK	33.24	10.544.753	9	Trypsin
YNEILQELDNVFSR	32.34	17.388.525	14	Trypsin
GTCFAEDK	32.29	9.263.804	8	Trypsin
NNLVFPLK	32.16	9.435.491	8	Trypsin
DDQQASTQKEQIPIKQNPVGITLR	32.05	27.064.299	24	Trypsin
NPVGITLR	31.61	8.685.131	8	Trypsin
FVVLNEIR	31.50	9.885.706	8	Trypsin
EQIPIKQNPVGITLR	31.23	17.049.886	15	Trypsin
GGTCFAEDK	31.06	9.834.018	9	Trypsin
VSDGSSEIFFK	30.96	12.145.819	11	Trypsin
EDTLFGR	30.88	8.364.028	7	Trypsin
EHLIEVSFELKR	30.24	14.988.143	12	Trypsin
FAVIGLSNNSDLEIFVNKLNK	29.39	23.492.581	21	Trypsin
LLAMWDDARLDYYLPEK	28.85	21.110.398	17	Trypsin

SNAMYEHDIYIGALEWVK	28.11	20.959.673	18	Trypsin
LDYYLPEK	28.06	10.395.226	8	Trypsin
LKSVSITEK	28.03	10.035.913	9	Trypsin
LMEAFAK	27.96	8.084.153	7	Trypsin
DLDDQQASTQKEQIPIKQNPVGITLR	27.75	29.345.410	26	Trypsin
SVSITEKGQR	27.19	11.035.935	10	Trypsin
DDQQASTQKEQIPIK	26.65	17.278.689	15	Trypsin
LEIFVNK	26.49	8.614.960	7	Trypsin
FLYDGIR	26.07	8.824.599	7	Trypsin
ILSPHIIK	25.40	9.195.854	8	Trypsin
FLEEDVAKEPILEGSLCTIDL	24.03	23.901.926	21	Trypsin
KSVSITEKGQRTYPVDASGSRIAEEVRDY	66.69	32.406.375	29	Chymotrypsin
AEDKKNLVFPLKTITYPLLGEIEGSKGY	66.31	32.367.332	29	Chymotrypsin
KFIDKVEDWYWGTCF	62.08	20.499.294	16	Chymotrypsin
DDQQASTQKEQIPIKQNPVGITL	58.99	25.503.289	23	Chymotrypsin
KTITYPLLGEIEGSKGY	57.86	18.679.930	17	Chymotrypsin
VNKLKSVSITEKGQRTYPVDASGSRIAEEVRDY	57.80	36.949.277	33	Chymotrypsin
RFAVIGLSNNSDLEIF	49.12	19.229.738	17	Chymotrypsin
LVFPLKTITYPLLGEIEGSKGY	45.54	24.373.508	22	Chymotrypsin
TQKPLNVVVLIIKYTY	41.92	21.492.034	18	Chymotrypsin
RLDREESISIMPDNIRASEDYKELW	40.89	32.765.720	27	Chymotrypsin
TYPVDASGSRIAEEVRDY	38.02	20.269.595	18	Chymotrypsin
AVIGLSNNSDLEIF	36.55	16.198.042	15	Chymotrypsin
NVVVLIKY	31.64	10.596.692	9	Chymotrypsin
KSVSITEKGQR	31.10	12.316.885	11	Chymotrypsin
AVIGLSNNSDLEIFVNKL	30.43	20.740.945	19	Chymotrypsin
FAVIGLSNNSDLEIFVNK	30.22	21.080.789	19	Chymotrypsin
TQKPLNVVVLIIKY	27.49	16.270.072	14	Chymotrypsin
RFAVIGLSN	26.92	10.895.930	10	Chymotrypsin
RFAVIGLSNNSDLEIFVNKL	26.40	23.772.642	21	Chymotrypsin
IPIKQNPVGITL	26.40	12.917.864	12	Chymotrypsin
RFAVIGLSN	23.44	9.755.501	9	Chymotrypsin
VFPLKTITYPLLGEIEGSKGY	22.03	23.242.666	21	Chymotrypsin
GRFLNAF	21.93	8.234.340	7	Chymotrypsin
TITYPLLGEIEGSKGY	21.88	17.398.981	16	Chymotrypsin
KSVSITEK	21.75	8.905.073	8	Chymotrypsin
KTITYPL	21.44	8.344.851	7	Chymotrypsin
KGQRTYPVDASGSRIAEEVRDY	21.36	24.962.356	22	Chymotrypsin
SNNSDLEIFVNKL	21.02	16.207.994	14	Chymotrypsin
KPVISSVNMS	22.09	10.605.587	10	Chymotrypsin
EVYAVVQGPL	21.68	10.735.757	10	Chymotrypsin

Table S4. Peptides obtained from mass spectrometry of the large Csx30 fragment using fully non-specific cleaved variants of the Csx30 protein.

Peptides	-10 log P	Mass	Length	Processed with
YREDIEEYCKPLLESNEDELCDLLLR	80.49	33.135.481	26	Trypsin
KANEIDTESFNAHLETLLR	70.32	22.001.123	19	Trypsin
LSKVEEIEKEVDISK	64.90	17.449.458	15	Trypsin
AGAEFCTFDKINYLMEVHYLICIR	64.72	30.494.500	25	Trypsin
VRDEVKLDVTSSREDTLFGR	64.56	23.211.975	20	Trypsin
AIGELKDQVESAISTFGDIK	62.61	21.201.001	20	Trypsin
LLAMWDDARLDYYLPEKVEVGPGK	62.26	28.764.783	25	Trypsin
KYNEILQELDNVFSR	60.35	18.669.475	15	Trypsin
FLNAFCGPGMDDR	57.76	14.986.333	13	Trypsin
VRDEVKLDVTSSR	57.08	15.028.052	13	Trypsin
RKYNEILQELDNVFSR	56.81	20.230.486	16	Trypsin
LDYYLPEKVEVGPGK	55.89	18.049.611	16	Trypsin
INYLMEVHYLICIR	54.84	19.229.746	15	Trypsin
SFNAHLETLLR	54.47	12.996.935	11	Trypsin
SNAMYEHDIYGAILEWGK	54.25	20.959.673	18	Trypsin
ASSPTKEVLSTLK	53.72	13.597.609	13	Trypsin
EHLIEVSFELKR	53.30	14.988.143	12	Trypsin
YNEILQELDNVFSR	52.97	17.388.525	14	Trypsin
EDIEEYCKPLLESNEDELCDLLLR	52.76	29.943.838	24	Trypsin
LVTSTEYEELWHK	51.77	16.337.987	13	Trypsin
VEEIEKEVDISK	51.35	14.167.347	12	Trypsin
SNEDELCDLLLR	48.87	14.756.926	12	Trypsin
AGAEFCTFDKINYLMEVHY	48.38	23.940.659	20	Trypsin
FLNAFCGPGMDDRQR	48.28	17.827.930	15	Trypsin
FLEEDVAKEPILEGSLCTIDL	48.19	23.901.926	21	Trypsin
AGAEFCTFDK	47.98	11.444.858	10	Trypsin
TSSREDTLFGR	47.94	12.676.156	11	Trypsin
DVTSSREDTLFGR	47.54	14.817.109	13	Trypsin
CESLLQIPEDERYR	47.45	18.068.571	14	Trypsin
DEVKLDVTSSR	47.38	12.476.357	11	Trypsin
IEEYCKPLLESNEDELCDLLLR	47.27	27.503.142	22	Trypsin
DQVESAISTFGDIK	47.07	15.087.358	14	Trypsin
EEIEKEVDISK	46.57	13.176.663	11	Trypsin
ITLWIEEGDFSPLR	46.16	16.748.617	14	Trypsin
DRQLFSVIELK	45.56	13.467.557	11	Trypsin
ANEIDTESFNAHLETLLR	45.35	20.720.173	18	Trypsin
FAVIGLSNNSLEDLEIFVNK	45.20	21.080.789	19	Trypsin
LLAMWDDARLDYYLPEK	45.11	21.110.398	17	Trypsin
AIGELKDQVESAISTFGDIKLVTSSTEYEELWHK	43.75	37.358.882	33	Trypsin
NLLETMSKPTSLK	42.88	14.607.909	13	Trypsin
EILQELDNVFSR	42.75	14.617.463	12	Trypsin

AMYEHDYIGAILEWGK	42.65	18.948.923	16	Trypsin
FLNAFCGPGMD	42.45	12.275.052	11	Trypsin
TESFNAHLETLR	42.33	15.297.838	13	Trypsin
QVESAISTFGDIK	42.01	13.937.089	13	Trypsin
LITEIPREHLIEVSFELKR	41.68	23.213.105	19	Trypsin
DTEFNAHLETLR	40.80	16.448.107	14	Trypsin
FLEEDVAKEPILEG	40.64	15.878.031	14	Trypsin
CESLLQIPEDER	39.97	14.876.926	12	Trypsin
VRDEVKLDVTSSRE	39.71	16.318.478	14	Trypsin
DEVKLDVTSSREDTLFGR	39.65	20.660.278	18	Trypsin
EEIKEVDISK	39.44	11.886.238	10	Trypsin
SGNWDKLITEIPR	39.39	15.278.044	13	Trypsin
LETMSKPTSLK	39.24	12.336.638	11	Trypsin
LLAMWDDARLDY	39.24	14.807.020	12	Trypsin
YLPEKVVVEVGPVK	38.74	14.137.867	13	Trypsin
ITLWIEEGDFSPRLR	38.65	18.219.301	15	Trypsin
GGGSGGGSGGGAWSHQPFEK	38.57	18.157.925	20	Trypsin
LLAMWDDAR	38.46	10.895.277	9	Trypsin
CEDGKLTG	38.37	9.494.539	8	Trypsin
EIDTEFNAHLETLR	38.35	18.869.374	16	Trypsin
NEILQELDNVFSR	37.95	15.757.893	13	Trypsin
ISFETWLGK	37.13	10.795.651	9	Trypsin
EDELCDLLLR	37.12	12.746.177	10	Trypsin
KLLAMWDDAR	36.47	12.176.227	10	Trypsin
VRDEVKLDVTSSRED	36.18	17.468.748	15	Trypsin
AIGELKDQVESAISTF	35.85	17.068.727	16	Trypsin
FVVLNEIR	35.42	9.885.706	8	Trypsin
NLLETMSKPT	35.05	11.325.798	10	Trypsin
VVEVGPVK	34.37	7.834.490	8	Trypsin
FLNAFCGPGMDD	34.31	13.425.322	12	Trypsin
QLFSVIELK	33.64	10.756.277	9	Trypsin
SSSAWSHQPFEK	33.22	13.896.313	12	Trypsin
AFCGPGMDDR	33.22	11.244.379	10	Trypsin
LDYYLPEK	33.07	10.395.226	8	Trypsin
GDFSPLR	33.05	7.903.973	7	Trypsin
EDTLFGR	32.80	8.364.028	7	Trypsin
AIGELKDQVESAISTFG	32.42	17.638.940	17	Trypsin
DELCDLLLR	32.30	11.455.751	9	Trypsin
KVVEVGPVK	32.23	9.115.439	9	Trypsin
EPILEGSLCTIDL	32.03	14.587.275	13	Trypsin
LMEAFK	31.10	8.084.153	7	Trypsin
NLLETMSK	30.88	9.344.794	8	Trypsin
FLEEDVAK	30.68	9.494.756	8	Trypsin
EGDFSPLR	30.65	9.194.399	8	Trypsin

LSKVEEEIK	29.95	10.735.968	9	Trypsin
ELCDLLLR	29.55	10.305.481	8	Trypsin
AHLETLR	29.53	9.515.502	8	Trypsin
LLAMWDDARL	29.35	12.026.118	10	Trypsin
FLNAFCG	29.20	8.273.636	7	Trypsin
EHLIEVSF	29.05	9.724.916	8	Trypsin
EHLIEVSFELK	29.03	13.427.133	11	Trypsin
NEDELCDLLR	28.84	13.886.605	11	Trypsin
WFEKCEDGK	28.69	12.545.339	10	Trypsin
LDREESISIMPPDNIR	28.30	19.989.680	17	Trypsin
TKILSPHIIK	28.11	11.487.281	10	Trypsin
IAEEVRDYTKPLNVVLIK	28.06	24.394.099	21	Trypsin
NEIDTESFNAHLETLR	28.02	20.009.803	17	Trypsin
PREHLIEVSFELKR	27.75	17.519.681	14	Trypsin
ILSPHIIK	27.65	9.195.854	8	Trypsin
ESNEDELCDLLR	27.61	16.047.351	13	Trypsin
VSDGSSEIFFK	27.29	12.145.819	11	Trypsin
FLYDGIR	27.03	8.824.599	7	Trypsin
DYTKPLNVVLIK	26.88	17.420.342	15	Trypsin
YIGAILEWGK	26.36	11.486.229	10	Trypsin
KPLLESNEDELCDLLR	26.10	20.560.510	17	Trypsin
ARLDYYLPEK	26.01	12.666.608	10	Trypsin
LMESVHY	25.64	8.774.004	7	Trypsin
HDYIGAILEWGK	25.52	14.007.089	12	Trypsin
LFSVIELK	25.44	9.475.692	8	Trypsin
EVLSTLK	25.14	7.884.644	7	Trypsin
ITLWIEEGDF	25.09	12.215.917	10	Trypsin
RQLFSVIELK	24.85	12.317.288	10	Trypsin
ESLLQIPEDER	24.81	13.276.619	11	Trypsin
VRDEVKDVTS	24.74	11.726.400	10	Trypsin
LSPHIIK	24.55	8.065.014	7	Trypsin
ISFETWLGKMER	24.19	14.957.493	12	Trypsin
YYLPEKVVVEVGPGK	24.06	15.768.500	14	Trypsin
LITEIPR	23.44	8.405.069	7	Trypsin
VRDEVKDVTS	23.44	12.596.721	11	Trypsin
VRDEVK	23.23	8.574.970	7	Trypsin
FVVLNEIRCE	23.12	12.776.438	10	Trypsin
SKVEEEIK	22.52	9.605.128	8	Trypsin
REDTLFGR	22.43	9.925.039	8	Trypsin
NLLETMSKPTSL	22.40	13.326.959	12	Trypsin
AIGELKDQVESAISTFGD	22.39	18.789.210	18	Trypsin
FLNAFCGPG	22.35	9.814.378	9	Trypsin
INYLMEVHY	21.93	12.675.907	10	Trypsin
AGAEFCTFDKINYLMEVHYLICIRDK	21.32	32.925.718	27	Trypsin

EESISIMPDNDIR	21.19	16.147.559	14	Trypsin
RLMEAFK	21.02	9.645.164	8	Trypsin
LWFEGKCEDGK	20.93	13.676.179	11	Trypsin
DVTSSREDTLF	20.75	12.685.884	11	Trypsin
TYPVDASGSR	20.52	10.514.934	10	Trypsin
HYAHVDCPGHADYVK	52.52	17.677.787	15	Trypsin
GYRPQFYFR	41.84	12.326.090	9	Trypsin
PSDLIPELQGR	27.15	12.236.510	11	Trypsin
NIIMIGPTGVGK	26.30	11.986.743	12	Trypsin
DIDEHSADAGV	30.32	11.274.730	11	Trypsin
RYEYGYK	29.72	9.774.606	7	Trypsin
VVVPIDR	25.35	7.964.807	7	Trypsin
VVVPIDR	25.35	7.964.807	7	Trypsin
PAVTIGLTK	25.34	8.985.488	9	Trypsin
VEDALHATR	25.01	10.105.145	9	Trypsin
VEDALHATR	25.01	10.105.145	9	Trypsin
VEDALHATR	25.01	10.105.145	9	Trypsin
AAQSLTLK	21.98	8.304.861	8	Trypsin
CTNRNELR	21.84	10.615.037	8	Trypsin
KGDNSVDYPDY	21.69	12.715.305	11	Trypsin
PTALRMLMKAGNE	21.15	14.307.374	13	Trypsin
LIPAIRPP	20.79	8.755.592	8	Trypsin
VATVEPGVV	20.56	8.694.858	9	Trypsin
SVIELKAALHKNLLETMSKPTSL	51.71	25.224.141	23	Chymotrypsin
GRFLNAFCGPGMDDRQLN	50.97	22.230.425	19	Chymotrypsin
FAVIGLSNNSLEDLIFVNK	42.11	21.080.789	19	Chymotrypsin
SNAMYEHDIYGAILEWGK	41.32	20.959.673	18	Chymotrypsin
RGVPGLTKFLEEDVAKE	39.47	18.870.101	17	Chymotrypsin
DKINYLMESVHY	38.43	15.107.126	12	Chymotrypsin
RGVPGLTKFLEEDVAKEPILEGSLCTIDL	36.43	31.986.846	29	Chymotrypsin
RFVVLNEIRCESLLQIPEDERY	36.27	27.774.170	22	Chymotrypsin
NRLSKVEEIEKVDISKASSPTKEVLSTL	33.90	32.287.451	29	Chymotrypsin
GRFLNAFCGPG	32.92	11.945.604	11	Chymotrypsin
LSGNWDKLITEIPREHLIEVSF	32.69	25.953.696	22	Chymotrypsin
AMWDDARLDY	30.18	12.545.339	10	Chymotrypsin
IEEGDFSPLRF	30.04	13.086.350	11	Chymotrypsin
AMWDDARLDYYLPEKVVVEVGPGKVRDEVLK DVTSSREDTLF	28.85	47.403.745	41	Chymotrypsin
NEILQELDNVF	28.84	13.326.561	11	Chymotrypsin
SVIELKAALH	28.25	10.796.339	10	Chymotrypsin
GDIKLVSTEYEELW	28.12	17.818.723	15	Chymotrypsin
NEIRCESLLQIPEDERY	27.92	21.630.266	17	Chymotrypsin
GRFLNAFCG	27.80	10.404.862	9	Chymotrypsin
KLLAMWDDARLD	27.64	14.457.336	12	Chymotrypsin
KNLLETMSKPT	27.20	12.606.748	11	Chymotrypsin

CTFDKINYLMESVHY	26.77	19.188.594	15	Chymotrypsin
GDIKLVSTEYEELWHKAGAEF	26.35	25.222.329	22	Chymotrypsin
LAMWDDARLDY	26.08	13.676.179	11	Chymotrypsin
ELKRDRQLF	25.99	12.036.724	9	Chymotrypsin
LMESVHY	25.30	8.774.004	7	Chymotrypsin
KLLAMWDDARL	25.13	13.307.067	11	Chymotrypsin
GDIKLVSTEYEELWHKAGAEFCTF	25.04	29.303.796	25	Chymotrypsin
FAVIGLSNNSDLEIFVNKLLK	24.56	23.492.581	21	Chymotrypsin
SPHIIKY	23.66	8.564.807	7	Chymotrypsin
KDVTSSREDTLFGRFL	23.21	18.699.584	16	Chymotrypsin
VVLNEIRCE	22.57	11.305.753	9	Chymotrypsin
GGTKILSPHIIKY	22.47	14.969.078	13	Chymotrypsin
VTSSREDTLF	22.29	11.535.615	10	Chymotrypsin
RLSKVEEIIKEVDISKASSPTKEVLSTL	22.27	31.147.024	28	Chymotrypsin
NAHLETLL	22.16	9.094.919	8	Chymotrypsin
REDIEEY	22.11	9.524.138	7	Chymotrypsin
ITLWIEEGDFSPLR	22.02	16.748.617	14	Chymotrypsin
GRFLNAFC	21.94	9.834.647	8	Chymotrypsin
GGTKILSPHIIKYREDIEEY	21.81	24.313.110	20	Chymotrypsin
KNLLETM	21.55	8.474.473	7	Chymotrypsin
KPVISSVNMS	28.17	10.605.587	10	Chymotrypsin
AHVDCPGHADY	25.83	12.404.930	11	Chymotrypsin

Table S5. Oligos and peptides used in this study

Oligos		
Name	Sequence (5'-3')	Description
CY681	CUCUAGU AACAGCCGUGGAGUCCGGGGCAGAAAAUUGG SUACCGUG	Matching PFS region; For cryoEM and biochemical assays
CY682	CUCUAGU AACAGCCGUGGAGUCCGGGGCAGAAAAUUGG ACGAUUAA	Non-matching PFS region; For cryoEM and biochemical assays
Sub_38nt	Cy5-CUCUAGU AACAGCCGUGGAGUCCGGGGCAGAAAAUUGG ACGAUUAA	For cleavage
Sub_24nt	Cy5- GAGAUCAUUGUCGG GUGGAGUCCGGGGCAGAAAAUUGG ACGAUUAA	For cleavage; mismatch.
Sub_18nt	Cy5- GAGAUCAUUGUCGGCACCCUC UCCGGGGCAGAAAAUUGG ACGAUUAA	For cleavage; mismatch.
Sub_12nt	Cy5- GAGAUCAUUGUCGGCACCCUCAGGCC GCAGAAAAUUGG ACGAUUAA	For cleavage; mismatch.
Sub_6nt	Cy5- GAGAUCAUUGUCGGCACCCUCAGGCCCCGUCUU AAUUGG ACGAUUAA	For cleavage; mismatch.
Sub_6nt	Cy5- GAGAUCAUUGUCGGCACCCUCAGGCCCCGUCUU AAUUGG ACGAUUAA	For cleavage; mismatch.
Sub_9nt	Cy5- CCCGG GAGAUCAUUGUCGGCACCCUCAGGCCCCGU GAAAAUUGG ACGAUUAA	For cleavage; mismatch.
Target RNA v1 (DNA sequence version)	TCGATCAGAGCGCTCTTACGTAATACGACTCACTATAGGTGTACGCTATTCAGGGATT GACTGATACCGGAAGACATCTCTCTAGTAACAGCCGTGGAGTCCGGGGCAGAAAATTG GTGTAGCCTTTTGGCTCTTAATACCAATGAAAAACCTATGCCTAGCATAACCCCTTGGG GCCTCTAAACGGGTCTTGAGGGGTTTTTGGGGAGTGTTTGAAGTGGACC	
Target RNA v2 (DNA sequence version)	TCGATCAGAGCGCTCTTACGTAATACGACTCACTATAGGGAATAGCAAGGCCTTCC GGTCTCAATGAAGGGCCGGGAACCTCTAGTAACAGCCGTGGAGTCCGGGGCAGAAAAT TGGAGGTACGCGCGTGGTATGGGAGGATCAAGGGGCCAATAGACTAGCATAACCCCTT GGGGCCTCTAAACGGGTCTTGAGGGGTTTTTGGGGAGTGTTTGAAGTGGACC	
Target RNA v3 (DNA sequence version)	TCGATCAGAGCGCTCTTACGTAATACGACTCACTATAGGAGGAAGCTACCAAT ATTTAGTTTCTGAGTCTCACGACAGACTCTAGTAACAGCCGTGGAGTCCGGGG CAGAAAATTGGCCCAACGCCTCGGATATGACTATATACTTAGGTTTCGATCTCTA GCATAACCCCTTGGGGCCTCTAAACGGGTCTTGAGGGGTTTTTGGGGAGTGTT TGAAGTGGACC	
Target RNA v4 (DNA sequence version)	TCGATCAGAGCGCTCTTACGTAATACGACTCACTATAGGCCAGACTGTAG CTCTTTGTTCTGTCAAGGCCGACCTTCTCTAGTAACAGCCGTGGAGTCC GGGGCAGAAAATTGGAACGTTACCGATTCTTCTGCGGACCATACCGTC CTGATACTAGCATAACCCCTTGGGGCCTCTAAACGGGTCTTGAGGGGTT TTTTGGGGAGTGTTTGAAGTGGACC	
Primers for PCR		
1	TTCCAATCCAATGCAATGAAAAATTCACCATCGG	On Csx31 gBlock
2	AGGGCTTCAGGATTAATGATGGTGTTTCATGCATTTTTC	On Csx31 gBlock
3	TTCCAATCCAATGCAATGTATGAGCACGATTATATTGG	On Csx30 gBlock
4	AGGGCTTCAGGATTATTCTTCATAGGTATATTTGATG	On Csx30 gBlock
5	TTCCAATCCAATGCAATGAAAGAACCGGAAGAAATC	On RpoE gBlock
6	AGGGCTTCAGGATTAGTCGCTCATCAGAATTTTGC	On RpoE gBlock
7	CTCATTAGGCACCCCGGAAATTAATACGACTCACTATAGG	On pRAMP for generating the LacI repressed T7 promoter

		followed by a N-terminal Twin-Strep-Tag II and a SUMO-tag
8	ATCGTGCTCATACATTGCATTGGATTGGAAGTACAGG	Combine with primer #7 for integration in Csx30
9	GGTGAATTTTTCCATTGCATTGGATTGGAAGTACAGG	Combine with primer #7 for integration in Csx31
10	TTCCGGTTCTTTCATTGCATTGGATTGGAAGTACAGG	Combine with primer #7 for integration in RpoE
11	GTCGTATTAATTTCCGGGGTGCCTAATGAGTGAGC	On pGFPuv for generating the backbone
12	TATACCTATGAAGAATAATCCTGAAGCCCTA GCATAACCCCTTGGGGCCTCTAAACGGGTCTTGA GGGGTTTTTGTAAATGAATTCCAACCTGAGCG	Combine with primer #11 for integration in Csx30
13	ATGAACACCATCATTTAATCCTGAAGCCCTAGC ATAACCCCTTGGGGCCTCTAAACGGGTCTTGAGGG GTTTTTGTAAATGAATTCCAACCTGAGCG	Combine with primer #11 for integration in Csx31
14	ATTCTGATGAGCGACTAATCCTGAAGCCC TAGCATAACCCCTTGGGGCCTCTAAACGG GTCTTGAGGGTTTTTGTAAATGAATTCCAACCTGAGCG	Combine with primer #11 for integration in RpoE
15	GTCGTATTAATTTCCCTAAATCAGTAAGTTGGCAGC	On pTPR-CHAT to construct pTPR-CHAT-target1
16	TTTTGCTGAAACCTCGTGATGATGGTGTTTTTGAGG	On pTPR-CHAT to construct pTPR-CHAT-target1
17	TACTGATTTAGGAAATTAATACGACTCACTATAGG	On pRAMP-CRISPR1-target1 to generate target 1 to construct pTPR-CHAT-target1
18	AACACCATCATACACGAGGTTTCAGCAAAAAACCCC	On pRAMP-CRISPR1-target1 to generate target 1 to construct pTPR-CHAT-target1
Peptides or proteins		
AK1	ARLTSMGGA	
AK2	ARLTSLGGA	
AK3	ARLTSFGGA	
AK4	ARLTSWGGA	
AK5	ARLTSYGGA	
AK6	ARLTSNGGA	
AK7	ARLTSMGPA	

AK8 AK9 AK10 AK11 AK12 AK13 AK14 AK15 AK16 AK17 AK18 AK19 AK20 AK21 AK22 AK23 AK24	ARLTVMGGA ARLT A MGGA ARLESMGGA ARLDSMGGA ARPTSMGGA ARVTSMGGA ARITSMGGA ARLEVMGGA DDRLTSMGGA DD D ARLTSMGGA ARLTSMG M ARLTSMG G N DARLTSMG G N ARTTSMGGA AKLTSMGGA AQLTSMGGA ANLTSMGGA	For peptide cleavage assay
GST-AK2- P3C	MGSPILGYWKIKGLVQPTRLLEYLEEKYEEHLYERDEGD KWRNKKFELGLEFPNLPYYIDGDVKTQSMARIYIADKH NMLGGCPKERAIEISMLEGAVLDIRYGVSRIAYSKDFETLK VDFLSKLPEMLKMFEDRLCHKTYLNGDHVTHPDFMLYDAL DVVLYMDPMCLDAFPKLVCFKKRIEAIQIDKYLKSSKYIAW PLQGWQATFGGGDHPKSDLVPRGSSGSGGGGG ARLTS LCG AGSGGGPNTEFALSLLRKNIMTITTSKGEFTGLGIHDR VCVIPTHAQPGDDVLVNGQKIRVKDKYKLVDPENINLEL TVLTLDRNEKFRDIRGFISEDLEGVDATLVVHSNNFTNTILEV GPVTMAGLINLSSPTNRMIRYDYATKTGQCGGVLCA TGKIFGIHVGGNGRQGFSAQLKKQYFVEKQ.	Cleavage site
Csx31	MEKFTIGYIFPSAKVKYVDSSEDFSSILEFVSNSEDERKFELFLW KQYTPHTLNVKTGASLKNLVFVEYGKKERLLVATEEF GPPALMKKYYVNNDAQFVWLKRNWKKWYRRWTKECGVDF EDNFKIEKVNLPIDEPSPRLSLYALRGKDYMLPVLGCKNLD YLRGYPLFYPGVADNDYNRSSCVYKTRDDTTDFPKCYEAKI INYNDINEAKNIRIYLHGFLYPAKWHHCIWKHIFALTN PNHIPEGEKQLWENYWKTKNIAESVFNNCKENSKYSSCDTTHC INQSLFDDVHDRIKAKCKNFLEEIVTAFETKTTNRIV TSNGNCKSDKEITILLAREIEIIVEQDTVLLGRKITPAFIQKVYLHV KFTGICHNWSDDLPLVHIRPVTMHLNRNIKKTK WFKRAEEGKAVVFTGTLCGVEKCMNTII	
Csx30	MYEHDIYGAILEWGKTKILSPHIIKYREDIEEYCKPLLESNEDEL DLLLRAIGELKDQVESAISTFGDIKLVSTEYEE LWHKAGAECTFDKINYLMEVHYLICIRDKRKYNEILQELDNV SRITLWIEEGDFSPLRFVVLNEIRCESLLQIPEDE RYRFPWYEAYSADDTVGIIIFNLFLSGNWDKLITEIPREHLIE VSFELKRDRQLFSVIELKAALHKNLLETMSKPT SLKLLAMWDDARLDYLLPEKVVEVGPVKVRDEVLDVTSSRED TLFGRFLNAFCGPGMDDRQRLNRLSKVEEIEKEVDIS KASSPTKEVLSTLKLWFEGKCEDGKLTKISFETWLGKMERKANEI DTESFNAHLETLLRGVPGLTKFLEEDVAKEPILEG SLCTIDLDDQQASTQKEQIPIKQNPVGITLRLDREESISIMPDPDNI RASEDYKELWKFIDKVEDWYWGTCFAEDKKN LVFPLKTITYPLLGEIEGSKGYRFAVIGLSNNSDLEIFVNKLS VSITEKGQRTYPVDASGSRIAEEVRDYTQKPLNVV VLIKYTYEE	
RpoE	MKEPEEIIINECFERNGEDVACKTCSLHGNKCKIMLPILYNKTRGI NSKGVKVRSTLEGFPIEDIKDIVKESIFAINGIK KGKFRGTRDAQFIKWVERIIHNKRVDFLRKKGKAERIKPLEGIEA SAQDCEPENIDDLIGFLKEKVGEGILNAEDIALIK ALYEGNENGCTQSEMSEEMGLKPDFAFKQRKCRLIKLESS GFGKDTLSKILMSD	

Movie S1. Binding of target RNA displays the gating loop, exposes Site 1 active site, and triggers Cas11 hinge motion in *Sb*-gRAMP.

Movie S2. Architecture and domain composition of the Craspase complex.

Movie S3. Cryo-EM reconstruction of apo-Craspase, with zoom-ins of the switch helix captured by the TPR repeats, keeping TPR-CHAT in the locked state.

Movie S4. Cryo-EM reconstruction of Craspase bound to a matching PFS-containing target RNA (self RNA), with zoom-ins of matching PFS (in light blue) accommodation.

Movie S5. Cryo-EM reconstruction of Craspase bound to a non-matching PFS-containing target RNA (non-self RNA), with zoom-ins of non-matching PFS (in yellow) accommodation.

Movie S6. Morphing of apo- and nm-PFS states showing the non-matching PFS triggered conformational relay.

Movie S7. Zoom-in view of the non-matching PFS triggered conformational relay. Switch helix is dislodged from TPR repeats by nm-PFS RNA. It participates in coiled coil formation and packs against CHAT. Sensor hairpins are perturbed, and the catalytic residues residing in the same strands align to become catalytically competent. CHAT domain also undergoes a rigid-body movement.